# Thermoelectric converter

A. V. Karimov and Sh. N. Bakhronov

*Physicotechnical Institute, 'Sun–Physics' Scientific Industrial Association, Uzbek Academy of Sciences, Tashkent*

Results are presented of investigations of a field- and temperature-controlled thermofield-effect transistor. It is shown experimentally that compared with thermistors, a thermofield-effect transistor has greater scope for controlling its operating point and output characteristics. © *1999 American Institute of Physics.* [S1063-7850(99)00802-2]

The use of thermoelectric effects to convert weak signals has been the subject of numerous original studies.[1,2] The functional capabilities of thermistors, posistors, and phase-transition elements have been extensively studied.[3,4] However, due consideration has not been given to aspects involved in developing new thermoelectric devices for the growing field of thermoelectronics.

Here we report results of an investigation of a thermosensitive element based on a thermofield-effect transistor which we have fabricated for the first time.

In contrast to resistor structures, the operating point as well as the temperature of this thermofield-effect transistor can be controlled by a cutoff voltage. This is achieved by assigning a particular sign to the temperature dependence of the channel resistance.

This thermoconversion structure is based on a gallium arsenide $p^+-n$ junction with two Ohmic contacts provided to the $n$-type region between which a channel is formed. One of the contacts acts as a drain and the other as the source. A continuous contact is applied to the $p^+$ region which serves as a gate. It is connected to the power supply so that the $p-n$ junction is always closed. In our case, a positive working voltage is applied to the drain and a control voltage to the gate–source junction, negative with respect to the gate. An increase in the cutoff voltage reduces the current flowing through the channel (Fig. 1a).

A thermotransistor effect is achieved in this field-effect transistor under conditions close to channel cutoff, in particular at gate voltages higher than $0.5V_1$ where $V$ is the cutoff voltage. For example, increasing the drain voltage to 1 V and the fixed temperatures to 100° C produces a family of characteristics similar to a triode (Fig. 1b).

It can be seen that at constant temperature the current between the drain and the source increases exponentially as a function of the drain voltage. Here the temperature fulfills the function of the input signal.

The ratio of the change in drain current to the temperature increment ($\Delta I/\Delta T$) is the thermal sensitivity, which is given by

$$S_\theta = \frac{\partial I}{\partial T},$$

or the specific thermal sensitivity is given by

$$S'_\theta = \frac{1}{I}\frac{\partial I}{\partial T}.$$

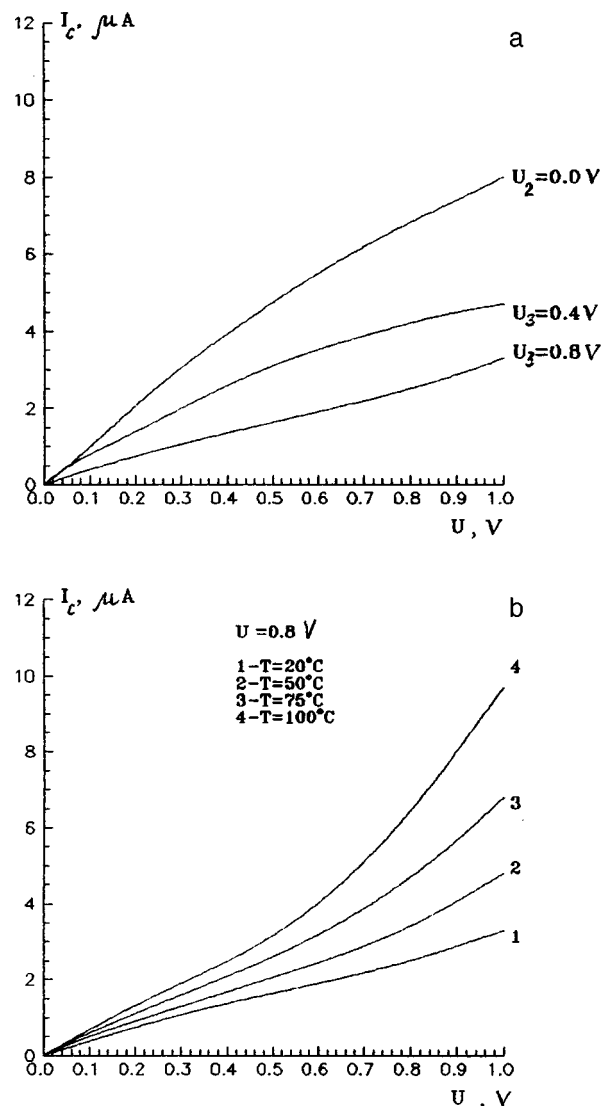The thermal sensitivity depends on the operating point and



FIG. 1. Drain current as a function of cutoff voltage (a) and also as a function of temperature (b) at a cutoff voltage of 0.8 V.
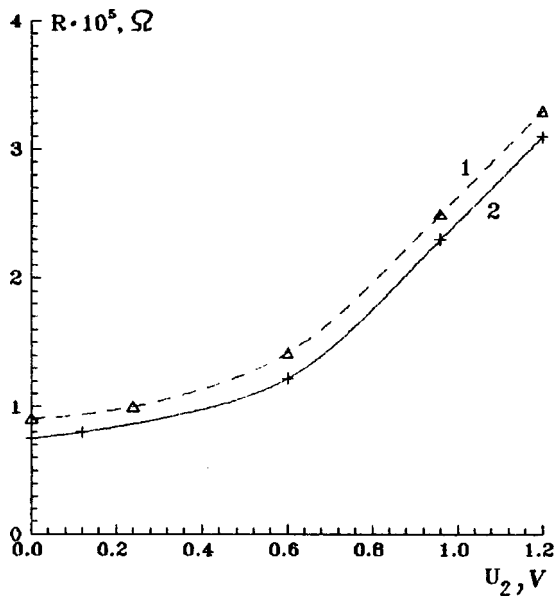
FIG. 2. Resistance of conducting section as a function of cutoff voltage (*1* — calculated curve, *2* — experimental curve).
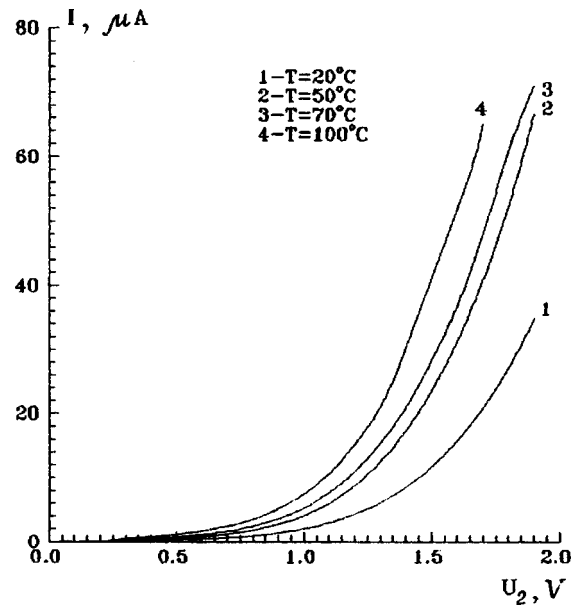


FIG. 3. Dependence of the return current of the gate $p-n$ junction at various temperatures.

increases as the drain voltage increases. For an operating voltage of 1.8 V this sensitivity is $(7-8)\times10^{-5}$ A/deg.

The resistance of the conducting section is a linear function of temperature $R\sim f(T)$ for $V_c=2kT/q$ at voltages below $V_1$. At room temperature (20 °C) at a cutoff voltage of 0.8 V the channel resistance is $2.32\times10^5\ \Omega$ and decreases to $1.35\times10^5\ \Omega$ at 100 °C. The dependence of the resistance on the cutoff voltage $V_2$ (Fig 2) is approximated by the function[5]

$$R=R_0/(1-(V_2/V_1)^{2/3}),$$

where $R_0$ is the channel resistance at zero bias, and $V_1$ is the cutoff voltage. The calculated (*1*) and experimental curves (*2*) of $R\sim V$ show satisfactory agreement.

If the output characteristics (Fig. 1b) are compared with the dependence of the gate current on the cutoff voltage (Fig. 3), we observe that the gate current initially varies negligibly and then increases abruptly. Investigations showed that the breakdown voltage of the gate $p-n$ junction varies linearly as a function of temperature:[6]

$$V_3(T)=V_3(T_0)+\beta V_3(T_0)\Delta T.$$

Here $T_0$ is room temperature, $\Delta T=T-T_0$, and $\beta$ is the temperature coefficient of the breakdown voltage:

$$\beta=\frac{V_3(T)-V_3(T_0)}{V_3(T_0)\Delta T}.$$

The temperature coefficient of the breakdown voltage determined using the data plotted in Fig. 3 was $3.53\times10^{-3}$ deg$^{-1}$, which agrees with the values $\beta=-(2-8)\times10^{-3}$ deg$^{-1}$ obtained for thermal breakdown.[7] The observed steep rise in the gate current is caused by electrical breakdown which leads to overheating of the $p-n$ junction.

Note that at all temperatures (20–100 °C) the behavior of the drain current as a function of voltage is the same and there is no breakdown of the drain–gate junction. The mechanism responsible for the increase in the drain current with temperature may be attributed to an increase in the thickness of the conducting part of the channel as a result of a reduction in the contact potential difference of the $p-n$ junction as a function of temperature.

To conclude, these investigations have shown that a thermofield-effect transistor has considerable scope for controlling its operating point and may be of interest for processing electrical and thermal signals.

[1] Yu. I. Ageev, M. M. Akperov, K. Z. Kobakhidze, M. V. Nebuchinov, L. S. Stil'bans, T. T. Tokarbaev, and É. M. Sher, Pis'ma Zh. Tekh. Fiz. **9**(11), 1396 (1983) [Sov. Tech. Phys. Lett. **9**, 601 (1983)].

[2] Yu. I. Ageev, A. É. Bilyalov, L. S. Stil'bans, and É. M. Sher, Pis'ma Zh. Tekh. Fiz. **7**(9), 1058 (1981) [Sov. Tech. Phys. Lett. **7**, 453 (1981)].

[3] A. A. Bugaev, B. P. Zakharchenya, Ya. G. Pyzhov, L. S. Stil'bans, F. A. Chudnovskiĭ, and É. M. Sher, Fiz. Tekh. Poluprovodn. **13**, 1446 (1979) [Sov. Phys. Semicond. **13**, 847 (1979)].

[4] M. I. Fedorov, V. I. Zaĭtsev, F. Yu. Solomkin, and M. V. Vedernikov, Pis'ma Zh. Tekh. Fiz. **23**(15), 64 (1997) [Tech. Phys. Lett. **23**, 602 (1997)].

[5] D. V. Igumnov and I. S. Gromov, *Operating Parameters and Usage Characteristics of Field-Effect Transistors* [in Russian], Radio i Svyaz', Moscow (1981) 64 pp.

[6] W. Shockley, Bell Syst. Tech. J. **28**, 435 (1949).

[7] V. F. Voronov, A. G. Akhmelkin, I. M. Dokuchaev *et al.*, *Gate Currents in p–n-Junction Field-Effect Transistors. Electronic Engineering Reviews. Series "Semiconductor Devices"* [in Russian], Vol. 4(22), TsNII Élektronika, (1972), 31 pp.

Translated by R. M. Durham

# Sensitivity of the surface microwave impedance of superconducting thin films to modulated optical radiation

V. M. Arutyunyan and V. C. Buniatyan

*Erevan State University*
(Submitted April 8, 1998; resubmitted September 14, 1998)
Pis'ma Zh. Tekh. Fiz. **25**, 50–56 (February 12, 1999)

A theoretical analysis is made of the photosensitivity of the component of the microwave surface impedance of high-temperature superconducting films exposed to intensity-modulated optical excitation. The results agree with the experimental data. © *1999 American Institute of Physics.* [S1063-7850(99)00902-7]

The discovery of high-temperature superconductors and the development of the technology for fabricating these as thin films has resulted in the development of sensitive microwave devices in the millimeter and submillimeter ranges, operating at liquid-nitrogen temperatures.[1,2] Recently, considerable interest has been shown in studying the properties of a superconductor exposed to radiant energy (such as laser radiation, infrared excitation, sound, and so on). Laser-induced decay of Cooper pairs, additional to the thermal damage in ordinary superconducting thin films, was investigated at the beginning of the seventies.[3–7] It was concluded that the formation of additional unpaired electrons in principle reduces the width of the energy gap in the superconductor, but the superconducting state itself is not destroyed up to quite specific densities of additional electrons and hence optical excitation energies. This phenomenon of photon interaction with the energy gap in high-temperature superconducting (HTSC) films and the nonbolometric decay of a pair of superconducting electrons may be used to detect weak short-wave signals, i.e., to fabricate highly sensitive detectors. The high sensitivity of HTSC YBCO films to optical excitation which has been achieved in practice (see Refs. 8–13) has opened up the possibility of developing optical switches,[14] mixers,[15] delay lines,[16] quasioptic filters,[17] and other optically controlled microwave devices.

The aim of the present paper is to analyze the dependence of the photosensitivity of the surface component of the microwave impedance of HTSC films when these are exposed to intensity-modulated optical excitation.

## THEORETICAL ANALYSIS

Clearly, if a modulated optical signal $\Phi = \Phi_0 \times (1 + \sin \omega_S t)/2$ is incident on a HTSC film, where $\Phi_0$ is the

radiation intensity (W/cm$^2$), $\omega_S$ is the signal modulation frequency, and $t$ is the time, the active and reactive components of the surface impedance of the film are modulated according to the pump law. We assume that as a result of optical radiation of intensity $\Phi_0$ being absorbed by the HTSC film, some nonbolometric dumping of electrons takes place via the superconducting gap (see, for example, Refs. 4, 7, and 9). The temperature of the film does not change significantly and in the limits of the two-fluid model the total electron density $n = n_S + n_N = n_{S\Phi} + n_{N\Phi}$ and the superconducting state are conserved. Then the density of electrons $n_S$ bound in pairs in the superconducting state decreases and the density of normal unbound electrons $n_N$ increases by the same amount $\Delta n_\Phi$. On this basis, we write the corresponding expressions for the density in the presence of irradiation denoted by the subscript "$\Phi$" in the form

$$n_{S\Phi} = n_S - \Delta n_\Phi, \quad n_{N\Phi} = n_N + \Delta n_\Phi. \tag{1}$$

For the density of nonequilibrium (additional) quasiparticles normalized to $4N(0)\Delta_0$, where $N(0)$ is the density of spin-1 states near the Fermi level and $\Delta_0$ is the energy gap at $T = 0$, Owen *et al.*[4] and Rothwarf *et al.*[7] obtained the expression

$$\Delta n_\Phi = \eta p \tau_{\text{eff}} [d\Delta(T, \Delta n_\Phi)]^{-1}, \tag{2}$$

where $p$ is the optical power incident per unit area (W/cm$^2$), $\eta$ is the dimensionless "effective quantum yield" which indicates the fraction of the power absorbed by the film which is directly dissipated in producing additional quasiparticles, and $d$ is the film thickness.

Using the results of Ref. 10, the expression for $\Delta n_\Phi$ can also be expressed directly in terms of the photon density $N_\Phi$ (cm$^{-3}$· photons/s) absorbed by the HTSC film:

TABLE I.

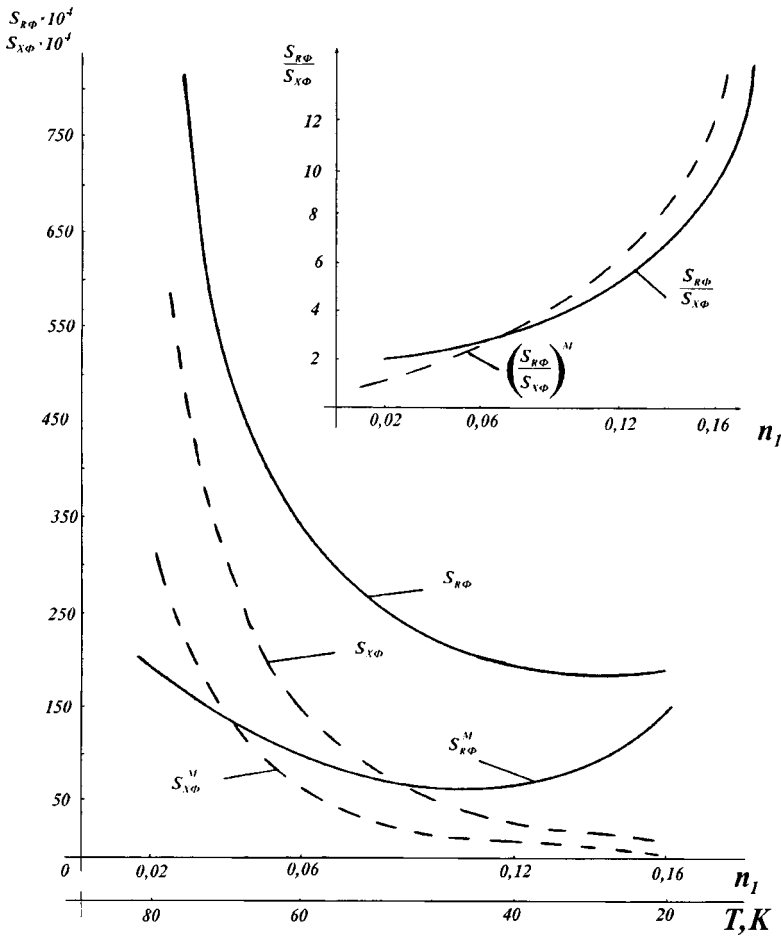| $n_1$ | $T$, K | $t_C$ | $\gamma(t_C)$ | $\Delta$, eV | $S_{R\Phi} \times 10^4$ | $S_{X\Phi} \times 10^4$ | $S_{R\Phi}^M \times 10^4$ | $S_{X\Phi}^M \times 10^4$ | $S_{R\Phi}/S_{X\Phi}$ | $S_{R\Phi}^M/S_{X\Phi}^M$ |
|---|---|---|---|---|---|---|---|---|---|---|
| 0.02 | 80 | 0.869 | 4.28 | 0.0139 | 1422 | 637 | 150 | 318.5 | 2.23 | 0.5 |
| 0.06 | 60 | 0.652 | 0.98 | 0.02 | 308 | 102 | 104 | 51 | 3.02 | 2.04 |
| 0.12 | 40 | 0.432 | 0.4 | 0.018 | 208 | 46 | 115 | 23 | 4.5 | 5 |
| 0.16 | 20 | 0.21 | 0.106 | 0.016 | 158 | 14 | 130 | 7 | 11.4 | 18.8 |

FIG. 1. Behavior of $S_{R\Phi}$ and $S_{X\Phi}$ ($S_{R\Phi}^M$ and $S_{X\Phi}^M$) as functions of the density $n_1$ of additional quasiparticles at various temperatures.

$$\Delta n_\Phi \cong \eta \tau_{\text{eff}} N_\Phi, \tag{3}$$

where $\tau_{\text{eff}}$ is the effective quasiparticle lifetime. It follows from expressions (2) and (3) that $\Delta n_\Phi \sim \Phi$ or $\Delta n_\Phi \sim N_\Phi$, and thus to a first approximation we have $\Delta n_\Phi \cong C\Phi \cong C_1 N_\Phi$. Then we have $C \cong \eta \tau_{\text{eff}} [d\Delta(T, \Delta n_\Phi)]^{-1}$, $C_1 \cong \eta \tau_{\text{eff}}$. After expressing $\Delta n_\Phi$ in terms of $n_N$ and $n_S$, we have $\Delta n_\Phi = n_N f_1 = n_S f_2$, where

$$f_1 \cong C\Phi n_N^{-1} \cong C_1 N_\Phi n_N^{-1},$$

$$f_2 \cong C\Phi n_S^{-1} \cong C_1 N_\Phi n_S^{-1}. \tag{3a}$$

We know that if the inequality $d \ll \lambda_L$ is satisfied in HTSC films, where $\lambda_L$ is the London penetration depth, analytic expressions for the active and reactive components of the surface microwave impedance calculated using the two-fluid model for $t_c = T/T_c < 1$ are written in the form[2,8]

$$R_S(t_C) = (\omega \mu_0)^2 \lambda_L^4(t_C) \sigma_N(t_C)/d,$$

$$X_S(t_C) = \omega \mu_0 \lambda_L^2(t_C)/d, \tag{4}$$

where

$$\lambda_L^2(t_C) = m_S(n_S q^2 \mu_0)^{-1}, \quad \sigma_N(t_C) = n_N q^2 \tau_N m_N^{-1}, \tag{5}$$

$T$ is the sample temperature, $T_C$ is the critical temperature, $\omega$ is the microwave field frequency, $\mu_0$ is the magnetic constant of vacuum, $\sigma_N$ is the conductivity, $m_S$, $m_N$, $n_S$, and $n_N$ are the effective masses and electron densities in the su-

perconducting and normal (nonsuperconducting) states, respectively, $\tau_N$ is the lifetime of the normal electrons, and $q$ is the electron charge.

Using expressions (1)–(4), we obtain the following expressions for the impedance components $R_{S\Phi}(t_C)$ and $X_{S\Phi}(t_C)$:

$$R_{S\Phi} \approx R_S(t_C)\{1 + 2f_2 + f_1 + 2f_1 f_2\},$$

$$X_{S\Phi} \approx X_S(t_C)\{1 + f_2\}. \tag{6}$$

We introduce the concept of the optical sensitivity of the components of the surface impedance $S_{R\Phi}$ and $S_{X\Phi}$. Expressions (4) and (6) readily yield expressions for these components

$$S_{R\Phi} \cong \frac{1}{R_S(t_C)} \frac{\partial R_{S\Phi}(t_C)}{\partial \Phi} \cong \frac{c}{n_S}\left\{2 + \frac{n_S}{n_N} + \frac{4C\Phi}{n_N}\right\},$$

$$S_{X\Phi} \cong \frac{1}{X_S(t_C)} \frac{\partial X_{S\Phi}(t_C)}{\partial \Phi} \cong \frac{c}{n_S}. \tag{7}$$

It follows from expression (7) that the rate of increase in $S_{R\Phi}$ with radiation intensity (the optical sensitivity with respect to $R$) is higher than that for $S_{X\Phi}$ (the sensitivity with respect to $X$). Similarly, in the opposite case $d > \lambda_L$, which is typical of a solid HTSC material such that[2,18]

$$R_{SM}(t_C) = (\omega\mu_0)^2 \lambda_L^3(t_C) \sigma_N(t_C)/2,$$

$$X_{SM}(t_C) = \omega\mu_0 \lambda_L(t_C), \tag{8}$$

we obtain

$$R_{S\Phi} \approx R_S(t_C)(1 + f_1 + 3f_1 f_2/2),$$

$$X_{S\Phi} \approx X_S(t_C)(1 + f_2/2), \tag{9}$$

and $S_{R\Phi}^M$ and $S_{X\Phi}^M$ are given by

$$S_{R\Phi}^M \cong \frac{c}{n_S}\left\{ \frac{n_S + 3C\Phi}{n_N} \right\}, \quad S_{X\Phi}^M \cong \frac{c}{2n_S}. \tag{10}$$

Since

$$\frac{n_S}{n_N} = \frac{1 - t_C^{3/2}}{t_C^{3/2}} = \frac{f_1}{f_2} = \frac{1}{\gamma(t_C)},$$

$$f_2 \cong \gamma(t_C) f_1, \quad \gamma(t_C) = \frac{t_C^{3/2}}{1 - t_C^{3/2}},$$

we obtain from expressions (7) and (10)

$$S_{R\Phi} \cong \frac{c}{n_N}\left\{ 1 + 2\gamma(t_C) + \frac{4C\Phi\gamma(t_C)}{n_N} \right\}, \quad S_{X\Phi} \cong \frac{c\gamma(t_C)}{n_N},$$

$$\frac{S_{R\Phi}}{S_{X\Phi}} \cong \frac{1 + 2\gamma(t_C)}{\gamma(t_C)} \tag{11}$$

for a thin film ($d \ll \lambda_L$), and

$$S_{R\Phi}^M \cong \frac{c\gamma(t_C)}{n_N}\left\{ \frac{1}{\gamma(t_C)} + \frac{3C\Phi}{n_N} \right\}, \quad S_{X\Phi}^M \cong \frac{S_{X\Phi}}{2}, \quad \frac{S_{R\Phi}^M}{S_{X\Phi}^M} \cong \frac{2}{\gamma} \tag{12}$$

for a solid material.

Expression (12) also indicates that for fixed $\gamma(t_C)$, we find $S_{R\Phi}^M > S_{X\Phi}^M$ at lower temperatures. For small $\Delta n_\Phi$ (Ref. 4) the change in the gap is described by $\Delta/\Delta_0 \cong 1 - 2\Delta n_\Phi$. For various temperatures (below $T_C$), using the results of Ref. 7, in particular the dependence of $\Delta/\Delta_0$ on $t_C$ for various values of $n_1 = \Delta n_\Phi[4N(0)\Delta_0]^{-1}$ and $\Phi_0 \cong 0.08$ mW/cm$^2$, $\tau_{\text{eff}} \cong 10^{-13}$ s, $\sin\omega_S t = 1$, $\eta \cong 0.1$, $d \cong 0.3$ $\mu$m, we can calculate the values for $S_{X\Phi}$ and $S_{R\Phi}$, as given by ex-

pressions (7) and (12). These values are given in Table I and the dependences of $S_{X\Phi}$ and $S_{R\Phi}$ (in arbitrary units) on $n_1$ are plotted in Fig. 1. As was to be expected, Fig. 1 shows that as $n_1$ and therefore the radiation intensity increase, a reduction in the optical sensitivity is observed. A relatively high sensitivity is observed for small $n_1$ (or $\Delta n_\Phi$), i.e., for small deviations of $T$ from $T_C$ and $n_S \ll n_N$.

Note that the predicted faster increase in $R_S$ with illumination relative to $X_S$ was observed in Ref. 8 for YBCO films. This relationship is also found for the temperature dependence and is clearly general because of the obvious inequalities $S_{R\Phi} > S_{X\Phi}$ for thin films and solid samples.

[1] O. G. Vendik *et al.*, Sverkhprovodimost' (KIAE) **3**(10), 2133 (1990).
[2] O. G. Vendik, S. Galchenko, E. Kollberg *et al.*, *Models of HTSC Transmission Lines as Applied to Computer Aided Design of Microwave Integrated Circuits* Report N 9, ISSN 1103–4599, ISRN CTH–MVT–R–9–SE (1994), 98 pp.
[3] L. R. Testardi, Phys. Rev. B **4**, 2189 (1971).
[4] C. S. Owen and D. F. Scalapino, Phys. Rev. Lett. **28**, 1559 (1972).
[5] W. H. Parker and W. D. Williams, Phys. Rev. Lett. **29**, 924 (1972).
[6] W. H. Parker, Phys. Rev. B **12**, 3667 (1975).
[7] A. Rothwarf, G. A. Sai-Halasz, and D. N. Langenberg, Phys. Rev. Lett. **33**, 212 (1974).
[8] E. Carlsson, S. Gevorgian, E. Kolberg *et al.*, in *Proceedings of the IEEE–MTT–S Topical Meeting on Optical Microwave Interactions*, 1994, pp. 195–197.
[9] M. Johnson, Appl. Phys. Lett. **59**, 1371 (1991).
[10] D. Gupta *et al.*, IEEE Trans. Appl. Supercond. **33**, 2895 (1993).
[11] E. K. Track, R. E. Drake, and G. K. G. Hobenwarterg, IEEE Trans. Appl. Supercond. **3**, 2899 (1993).
[12] Xin-Hua Hu, T. Juhasz, and W. E. Bron, Appl. Phys. Lett. **59**, 3333 (1991).
[13] D. Zhang, D. V. Plant, and H. Fetterman, Appl. Phys. Lett. **58**, 1560 (1991).
[14] D. B. Moix, D. P. Scherrer, and F. K. Kneubuhl, Infrared Phys. Technol. **37**, 403 (1996).
[15] Zh. Mai, X. Zao, F. Zhou *et al.*, Infrared Phys. Technol. **38**, 13 (1997).
[16] N. Bluser, J. Appl. Phys. **71**, 1336 (1992).
[17] A. Frenkel, M. A. Saifi, T. Venkatasen *et al.*, J. Appl. Phys. **67**, 3054 (1990).
[18] C. J. Wu and T. Y. Tseng, IEEE Trans. Appl. Supercond. **6**, 94 (1996).

Translated by R. M. Durham

# Waveguides coupled via apertures: asymptotic form of the eigenvalue

I. Yu. Popov

*St. Petersburg Institute of Precision Mechanics and Optics (Technical University)*

An analysis is made of the problem of waveguides coupled via small apertures. A method of matching the asymptotic expansions of solutions is used to find the asymptotic form of the eigenvalue which tends to the lower limit of the continuous spectrum for a small parameter, i.e., the aperture diameter. A similar asymptotic form is obtained for several coupling apertures. © *1999 American Institute of Physics.* [S1063-7850(99)01002-2]

The problem of studying the properties of the spectrum of coupled waveguides has attracted the attention of physicists and mathematicians for some time. Recently there has been a resurgence of interest following the development of nanoelectronics. In fact, the description of many mesoscopic quantum systems has been reduced to analyzing the transport properties of an electron wave in a quantum waveguide.[1–4] A system of two waveguides coupled via one or several apertures is considered here. Exner *et al.*[5] showed that there is an eigenvalue which tends to the lower limit of the continuous spectrum as the aperture narrows and obtained variational estimates for this. The problem of its asymptotic form, which was left open, is considered here.

Let us assume that $\Omega_\pm$ are two-dimensional waveguides with the boundaries $\{(x_1,x_2):x_2=0, x_2=\pm d_\pm\}$, connected by the window $\{(x_1,x_2):x_2=0, -a<x_1<a\}$. We shall consider the case $d_+\geq d_-$ and we shall assume that $\lambda_a=k_a^2$ is the unknown eigenvalue. To search for its asymptotic form, we use the system of matching asymptotic expansions proposed in Refs. 6 and 7, but we seek the asymptotic series in a slightly different form:

$$\sqrt{\pi^2/d_+^2-k_a^2}=\sum_{j=2}^\infty \sum_{i=0}^\infty k_{ji}a^j\ln^i a.$$

The asymptotic series for the corresponding eigenfunction are then

$$\psi_a(x)$$

$$=\begin{cases} \mp\sqrt{\dfrac{\pi^2}{d_+^2}-k_a^2}\sum_{j=0}^\infty a^j P_{j+1}(D_y,\ln a)G^\pm(x,y,k)\big|_{y=0}, \\[2mm] x\in\Omega^\pm/S_{\sqrt{a}}, \\[2mm] \sum_{j=1}^\infty \sum_{i=0}^{[(j-1)/2]} v_{ji}\left(\dfrac{x}{a}\right)a^j\ln^i a, \\[2mm] x\in S_{2\sqrt{a}}, \end{cases}$$

where $S_t$ is a sphere of radius $t$ with its center at the center of the aperture, $v_{ji}\in W_{2,\mathrm{loc}}^1(\Omega^+\cup\Omega^-)$, and $P_m$ are various polynomials of $D_y$ ($D_y$ is a derivative with respect to the variable $y$). The functions $G^\pm$ are the Green's functions of the waveguides $\Omega^\pm$, whose derivatives have the asymptotic forms (for $d_+>d_-$)

$$D_y^j G^+(x,0,k)=\sin\frac{\pi x_2}{d_+}D_x^i\left(\sin\frac{\pi x_2}{d_+}\right)\bigg|_{x_2=0}\left(\frac{\pi^2}{d_+^2}-k_a^2\right)^{-1/2}$$

$$+\Phi_j(x,k)\ln r+g_j^+(x,k)$$

$$+\sum_{i=0}^{\left[\frac{j}{2}\right]}\sum_{t=0}^{j-2i-1}b_{it}^{(j)}(k)r^{-j+2(i+t)}$$

$$\times\sin(j-2i)\Theta,$$

$$D_y^j G^-(x,0,k)=\Phi_j(x,k)\ln r+g_j^-(x,k)+\sum_{i=0}^{[j/2]}\sum_{t=0}^{j-2i-1}b_{it}^{(j)}$$

$$\times(k)r^{-j+2(i+t)}\sin(j-2i)\Theta,$$

where $(r,\Theta)$ are the polar coordinates; the terms $b_{it}^{(j)}(k)$, $\Phi_j(x,k)$, and $g_j^\pm(x,k)$ are analytic with respect to $k$ in some region near the point $\pi/d_+$; $\Phi_j\in C^\infty(\mathbf{R}^2)$ is odd with respect to the variable $x_2$; and $g_j^\pm\in C^\infty(\Omega^\pm)$.

Performing a procedure for matching the asymptotic expansions, we obtain the principal term of the asymptotic form $\lambda_a$ with respect to $a$ in the form

$$\lambda_a=\begin{cases}\dfrac{\pi^2}{d_+^2}-\left(\dfrac{\pi^3}{2d_+^2}\right)^2 a^4+o(a^4), & d_+>d_-, \\[3mm] \dfrac{\pi^2}{d^2}-\left(\dfrac{\pi^3}{d^2}\right)^2 a^4+o(a^4), & d_+=d_-=d.\end{cases}$$

Similarly, we can consider the case of $n$ coupling apertures of width $2a\omega_i$, $i=1,2,\ldots,n$. Here the asymptotic form of the ground state close to the boundary of the continuous spectrum has the form

$$\lambda_a=\begin{cases}\dfrac{\pi^2}{d_+^2}-\left(\dfrac{\pi^3}{nd_+^2}\sum_{i=1}^n c_{\omega_i}\right)^2 a^4+o(a^4), & d_+>d_-, \\[3mm] \dfrac{\pi^2}{d^2}-\left(\dfrac{2\pi^3}{nd^2}\sum_{i=1}^n c_{\omega_i}\right)^2 a^4+o(a^4), & d_+=d_-=d.\end{cases}$$

Here $c_{\omega_i}$ is the harmonic capacitance of the segment $\omega_i$ ($i$th coupling window) in $\mathbf{R}^2$. Note that this result explains why the sum of the squares of the aperture lengths appears as a measure of smallness of the coupling apertures in the variational estimates.[8]

[1] Y. Takagaki and K. Ploog, Phys. Rev. B **49**(3), 1782 (1994).

[2] P. Duclos and P. Exner, Rev. Math. Phys. **7**, 73 (1995).

[3] W. Bulla, F. Gesztesy, W. Renger, and B. Simon, Proc. Am. Math. Soc. **125**, 1487 (1997).

[4] I. Yu. Popov, Rep. Math. Phys. **40**, 521 (1997).

[5] P. Exner and S. Vugalter, Ann. Inst. Henri Poincaré Phys. Theor. **65**, 109 (1996).

[6] A. M. Il'in, *Matching of Asymptotic Expansions of Solutions of Boundary Value Problems*, American Mathematical Society, Providence, RI (1992) [Russian orig. Nauka, Moscow (1989), 214 pp.].

[7] R. R. Gadyl'shin, Algebra Analiz. **4**(2), 88 (1992).

[8] P. Exner and S. Vugalter, J. Phys. A: Math. Gen. **30**, 7863 (1997).

Translated by R. M. Durham

# Testing of intracavity multipass probing systems for diagnostics of a tokamak plasma by laser photoionization

Yu. V. Petrov, G. T. Razdobarin, and S. Yu. Tolstyakov

*A. F. Ioffe Physicotechnical Institute, Russian Academy of Sciences, St. Petersburg*
(Submitted September 18, 1998)
Pis'ma Zh. Tekh. Fiz. **25**, 60–65 (February 12, 1999)

Efficient laser systems for plasma probing have been developed using stable cavity configurations with low diffraction losses to improve the sensitivity of photoionization diagnostics. These probing systems were tested in demonstration experiments using the FT-1 tokamak. The results indicate that reliable measurements of the neutral hydrogen density may be made in the range $10^8 - 10^9$ cm$^3$ in a tokamak plasma.  © *1999 American Institute of Physics.*
[S1063-7850(99)01102-7]

Previous publications[1,2] have reported a new diagnostic method based on laser photoionization of excited hydrogen atoms in a tokamak plasma. Further development of this diagnostic technique involves increasing the accuracy with which the weak optical signal produced by photoionization can be measured in the presence of the noise of the plasma self-emission, which can be achieved by increasing the probing energy. It is also advisable to increase the energy under saturation conditions[2] when the recorded photoionization signal ceases to depend on the probe beam power. In this case, increasing the sensitivity of the diagnostics involves increasing the lasing duration and the number of generated pulses. To meet these requirements, laser systems have been developed using cavities with low diffraction losses which are suitable for intracavity multipass plasma probing in tokamaks.

These developments are based on two principles. This first is multipass plasma probing using a pair of mirrors positioned on either side of the tokamak discharge chamber. In this case, the probing energy is increased by increasing the number of passes of the laser beam through the plasma. The second principle is based on positioning the plasma inside a closed laser cavity. This allows a low lasing threshold because of the low end losses, thus increasing the lasing energy. Both principles can be implemented individually but the maximum effect is achieved by using them in combination. It has been suggested that at least two coupled cavity sections should be used, one designed to accommodate the active medium and the other to accommodate the plasma undergoing diagnostics. This configuration with a matching lens can provide lasing with the lowest losses.

The main requirements for intracavity multipass plasma probing systems are that the cavity length can be increased to match the large dimensions of the tokamak discharge chamber, and a low lasing threshold. These two contradictory requirements may be satisfied by using the most stable cavity configurations close to confocal.[3] A semiconfocal cavity of total length $\sim 10$ m which satisfies the requirements for multipass plasma probing is displayed schematically in Fig. 1a, which shows six complete passes of the beam through the

volume occupied by the plasma (three in each direction). In this configuration the role of the spherical mirror is played by a mirror-lens system consisting of a plane mirror *1* and a variable-focus matching objective *4*, between which are inserted a $\varnothing 45 \times 300$ Nd phosphate glass active element *3* and a phototropic switch *2* with an initial transmission of around 90%. The objective *4* is aligned to achieve confocal requirements such that the focus of the mirror-lens system (*1*, *4*) is matched with the plane mirror *6*. With this cavity configuration, the cross sections of the active element and the tokamak ports can easily be matched and the cavity length can be varied using the same optical elements.

Under confocal conditions multipulse lasing is achieved with more then ten pulses per train during pumping and a single-pulse energy of up to 6.5 J. The total number of beam passes inside the cavity was 30, for a total pulse duration of $\sim 2$ $\mu$s, which shows the low level of divergence losses. The low level of losses is also indicated by the low lasing threshold. Compared with the planar-configuration cavity used in the first experiments,[1,2] the threshold pump energy was reduced from 15 to 2.7 kJ. Some deterioration in the energy confinement was also noted when the cavity length was increased above 10 m, which corresponds to more than six passes of the probe beam through the plasma. This effect is more characteristic of regimes with high pump powers because of the thermal distortions and thus the impaired confocal conditions. An increase in the selective losses caused by thermal aberrations means that any increase in the number of probe beam passes above six cannot be used effectively. Nevertheless, despite the limited number of passes, this semiconfocal cavity system has obvious advantages over a planar cavity configuration[1,2] in terms of threshold pump energy and plasma probe energy.

An alternative system shown in Fig. 1b uses the principle of a composite cavity formed by confocal sections *A*, *B*, and *C*. The confocal condition is satisfied by matching the foci of lens *4* with the focus of the spherical mirror *6* and mirror *1*. In addition, the plane mirror *5* designed for multipass plasma probing is situated in the focal plane of the spherical mirror. Unlike the cavity configuration shown in
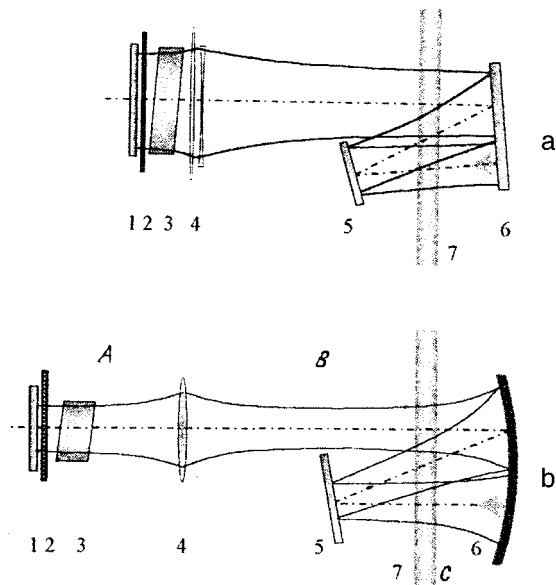
FIG. 1. Optical diagrams of stable cavity configurations: a — semiconfocal cavity, b — sectional confocal cavity. *1* — plane mirror, *2* — phototropic switch, *3* — active element, *4* — objective, *5, 6* — mirrors in multipass system, and *7* — plasma under diagnosis.

Fig. 1a, multipass probing in a sectional system does not imply increasing the cavity length and the associated diffraction losses. The losses only increase as a result of reflections at the surfaces of the optical elements and may be minimized by selecting highly reflecting coatings and antireflection-coated lens optics. The presence of a multipass system gives an increase in the plasma probing energy proportional to the number of passes.

This system demonstrated the lowest selective losses recorded so far, giving a low threshold pump energy of $\sim 1.9$ kJ and allowing multipulse operation with a large number of lasing pulses. For a given cavity length the beam cross
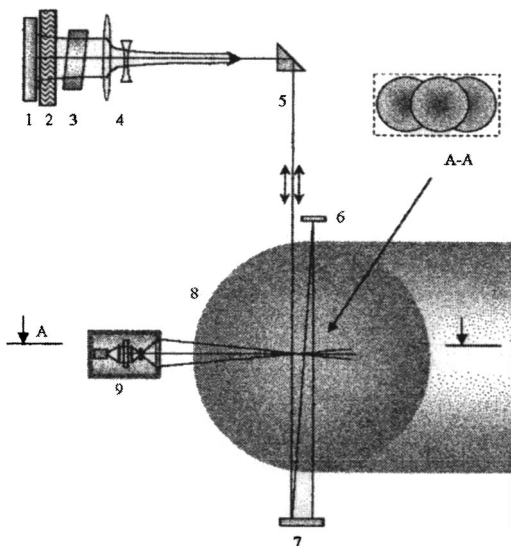


FIG. 2. Schematic of FT-1 tokamak experiment using semiconfocal cavity: *1* — plane mirror, *2* — phototropic switch, *3* — active element, *4* — objective, *5* — rotating prism, *6, 7* — plane mirrors, *8* — plasma, and *9* — light-gathering system. $A-A$ — beam cross section for six passes.
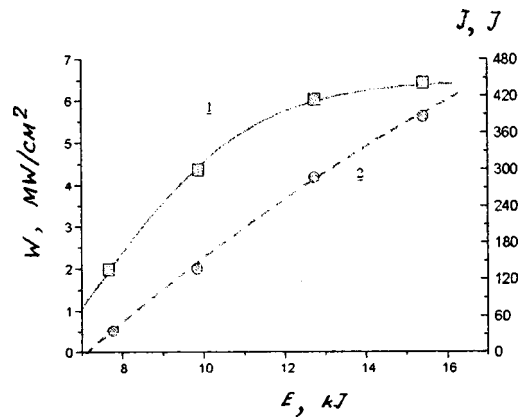


FIG. 3. Power density of probe radiation $W$ (*1*) and probe energy $J$ (*2*) as a function of pump energy $E$.

section at the optical elements can be varied widely without reducing the lasing energy. Thus, the radiation filling of the active medium and the tokamak ports can optimized.

Demonstration experiments were carried out on the FT-1 tokamak plasma ($R = 62.5$ cm, $a = 15$ cm) under standard discharge conditions using the system for recording the $H_\beta$ luminescence line discussed earlier.[1,2] Figure 2 shows an intracavity multipass probing system using a semiconfocal cavity with a total length $\sim 10$ m. Despite the additional nonselective losses caused by the tokamak chamber being in the cavity, high probe radiation parameters were achieved. At a moderate pump energy of 15 kJ, the number of pulses in the train was $N \geqslant 10$ and the pulse energy per pass was 5–6 J. The peak power density of the probe beam and the total plasma probing energy for the series of pulses in the train are plotted as a function of the pump energy in Fig. 3. The peak power density is 6.5 MW/cm$^2$, which is appreciably higher than the saturation value of $\sim 2$ MW/cm$^2$ under the discharge conditions in the FT-1 tokamak.

For comparison we note that in previous measurements[1,2] the pulse energy per pass was 3–5 J with a maximum pump energy of $\sim 40$ kJ. In addition, the duration of the probe pulses was more than doubled, reaching values $\sim 1$ $\mu$s at half-maximum. The longer probing duration is a significant factor in increasing the sensitivity of the diagnostics. Thus, it was possible to record signals for each of the-
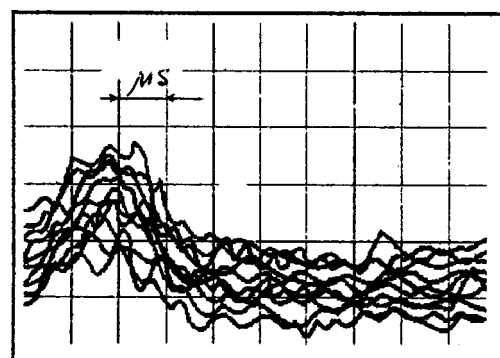


FIG. 4. Oscilloscope traces of photoionization signals.

series of laser pulses in the train in the presence of the plasma noise. This can be seen from the oscilloscope trace in Fig. 4, which gives the individual photoionization signals recorded for a series of lasing pulses during pumping. The results of the measurements shown in the trace correspond to a plasma region with a concentration of unexcited hydrogen atoms of less than $10^{10}\,\text{cm}^{-3}$. Averaging the signals over the series of pulses in the train can provide reliable measure-

ments in the range of concentrations between $10^8$ and $10^9\,\text{cm}^{-3}$ typical of the central part of the plasma.

[1] V. K. Gusev, A. V. Dech, D. V. Kuprienko *et al.*, Pis'ma Zh. Tekh. Fiz. **21**, 32 (1995) [*sic*].
[2] V. I. Gladuschak, V. K. Gusev, M. Yu. Kantor *et al.*, Nucl. Fusion **35**, 1385 (1995).
[3] Yu. A. Anan'ev, *Laser Cavities and the Beam Divergence Problem* (Adam Hilger, Philadelphia, 1992).

Translated by R. M. Durham

# Influence of electron bombardment on recombination and attachment in II–VI—IV–VI film photoconductors

V. É. Bukharov, A. G. Rokakh, and S. V. Stetsyura

*N. G. Chernyshevskiĭ State University, Saratov*
(Submitted April 28, 1998)
Pis'ma Zh. Tekh. Fiz. **25**, 66–72 (February 12, 1999)

An investigation is made of the action of electron bombardment on wide-gap photosensitive films of II–VI compounds with submicron IV–VI inclusions which form bounded solid solutions with these compounds. It is shown that the radiation resistance of II–VI compounds is enhanced by adding IV–VI compounds. It is observed that the radiation acts differently on shallow and deep levels in the wide-gap semiconductor. An explanation is proposed for the experimental data using a heterophase semiconductor model. © *1999 American Institute of Physics.* [S1063-7850(99)01202-1]

Our recent investigations have shown that the addition of submicron inclusions of a IV–VI narrow-gap phase to a II–VI wide-gap photosensitive matrix substantially enhances the degradation resistance of the photoconductor, with little influence on the position of the natural spectral sensitivity maximum of the initial material. Studies of this effect are vital, since the rapid photofatigue and degradation of II–VI compounds exposed to external influences severely restricts their range of application.

The aim of the present paper is to make a comparative analysis of the action of electron bombardment on the lifetime and photoresponse time of CdS(Se) photoconducting films and bounded CdS(Se)–PbS solid solutions containing less than fractions of a percent of a narrow-gap component.

To solve this problem we measured the characteristics of film samples before and after electron bombardment at below-threshold energies (the samples were irradiated in a vacuum of $10^{-5}$–$10^{-4}$ Torr using an electron gun, the radiation dose was $4.4 \times 10^9$ rad, and the anode voltage was 10 kV.)

We know that the electron-induced conductivity (cathodoconductivity) $Y$ of a monopolar, fairly thin (the electrode gap $a$ and the electrode length $l$ are much greater than the film length $d$) $n$-type sample under a fairly high level of excitation is given by[1]

$$Y(E_0) = \int_0^d \frac{l\sigma}{a} dx = \frac{le}{a} \int_0^d \mu n(x, E_0)\, dx$$

$$= \frac{le}{a} \int_0^d \mu \tau(x)\, G(x, E_0)\, dx, \quad (1)$$

where $E_0$ is the initial electron energy, $\sigma$ is the conductivity, $e$ is the elementary charge, $\mu$ and $\tau$ are the electron mobility and lifetime, respectively, $n$ is the free electron density, $G$ is the electron-beam-induced carrier generation function[1]

$$G(x, E_0) = \frac{J}{eE_g'}\left|\frac{dE}{dx}\right|, \quad (2)$$

where $J$ is the beam current density, $E_g'$ is the formation energy of an electron–hole pair, which is[1] approximately three times the band gap $E_g$ of the material being bombarded, and the energy loss function $|dE/dx|$ may be written as[1]

$$\left|\frac{dE}{dx}\right| = \frac{2E_0(1 - 0.5\eta - 0.4\eta^2)}{\sqrt{\pi}\Delta R_m(1 + \mathrm{erf}\,\chi)} \exp\left[-\left(\frac{x}{\Delta R_m} - \chi\right)^2\right], \quad (3)$$

where $\eta$ is the backscattering coefficient, $\chi = R_m/\Delta R_m$, $R_m$ is the position of the energy loss maximum, and $\Delta R_m$ is its half-width.[2]

Experimental studies of the cathodoconductivity of CdS(Se) samples as a function of the electron energy (cathodoconductivity spectra) for a direct beam current showed that the rate of change in the current through the sample decreased with increasing radiation dose (Fig. 1), whereas for samples with added PbS the spectrum remained almost unchanged up to the maximum dose.

The degradation of the CdS(Se) samples can naturally be attributed to changes in $\tau$ during irradiation, since in Eq. (1) $G$ does not depend on the absorbed dose and a substantial radiation-induced change in $\mu$ is doubtful. Since the cathodoconductivity spectra are measured in vacuum directly during irradiation, the lifetime $\tau$ calculated for these only changes as a result of electron bombardment and does not depend on the influence of atmospheric gases, moisture, and other factors.

Equations (1)–(3) can be used to determine $\tau$ in the surface and bulk layers from the cathodoconductivity spectra or the average lifetime $\tau$ over the entire volume of the sample. Our calculations using the experimental data (Fig. 1) and formulas (1)–(3) gave a reduction in the average lifetime $\tau$ under irradiation from $1.63 \times 10^{-4}$ s ($D = 0$) to $3.45 \times 10^{-5}$ s ($D = 4.47 \times 10^9$ rad) for CdS(Se) samples. For CdS(Se)–PbS samples the change in $\tau$ at the maximum dose was less than 7% from $1.96 \times 10^{-4}$ s ($D = 0$) to $1.84 \times 10^{-4}$ s ($D = 4.47 \times 10^9$ rad).

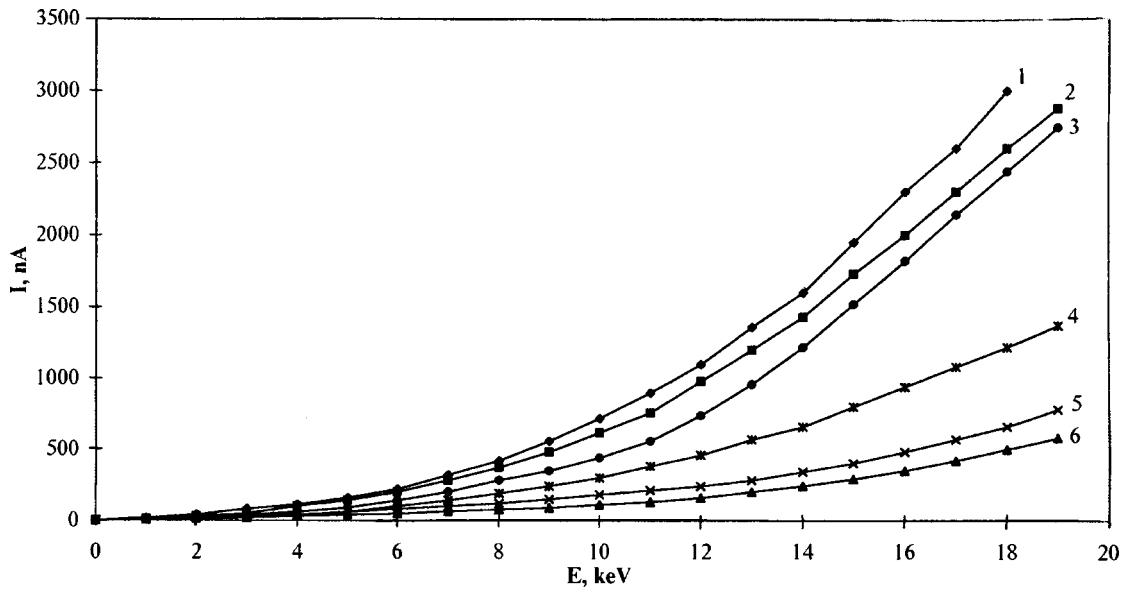In addition to the static characteristics, we also investigated the influence of electron bombardment on the photo-

FIG. 1. Dependence of the electron-beam-induced current on the energy of the bombarding electrons: *1*, *2* — CdS(Se)–PbS sample (*1* — before irradiation, *2* — after irradiation with the dose $D = 4.4 \times 10^9$ rad), *3–6* — CdS(Se) sample (*3* — before irradiation, *4* — $D = 8.7 \times 108$ rad, *5* — $D = 2.6 \times 10^9$ rad, *6* — $D = 4.4 \times 10^9$ rad). The spectra were recorded at low beam currents ($10^{-9}$ A) in intervals between series of bombardments using the same apparatus where the dose was received at high current ($10^{-6}$ A.)

current kinetics from the change in the photocurrent response time $\tau_{ph}$. The measurements were made under illumination by white light whose intensity was modulated sinusoidally by a mechanical modulator at frequencies between 0 and 2 kHz (Fig. 2). The frequency characteristics were used to determine the photoresponse times.[3]

When comparing the photoresponse time $\tau_{ph}$, we should note the following facts: 1) $\tau_{ph}$ for samples with PbS was always less than or equal to that for samples without PbS (between $3.3 \times 10^{-4}$ and $1.17 \times 10^{-3}$ s); 2) after electron bombardment at below-threshold energies $\tau_{ph}$ was reduced by a factor of three for samples with PbS (from $1.1 \times 10^{-3}$ to $3.35 \times 10^{-4}$ s). For samples without PbS more stable values

of $\tau_{ph}$ were obtained: $1.25 \times 10^{-3}$ s before irradiation and $8.65 \times 10^{-4}$ s after irradiation, i.e., the change was less than 25%.

The reduction in the lifetime $\tau$ observed in CdS(Se) is naturally attributed to a radiation-induced increase in the number of defects (deep levels) forming recombination centers. The fact that $\tau$ remains constant in samples with PbS implies that defect formation in these samples does not influence the photoconductivity, i.e., defects either do not form at all or they form in narrow-band inclusions, which do not participate in the photoconduction, or they accumulate in these inclusions (or at the phase interfaces), forming in the
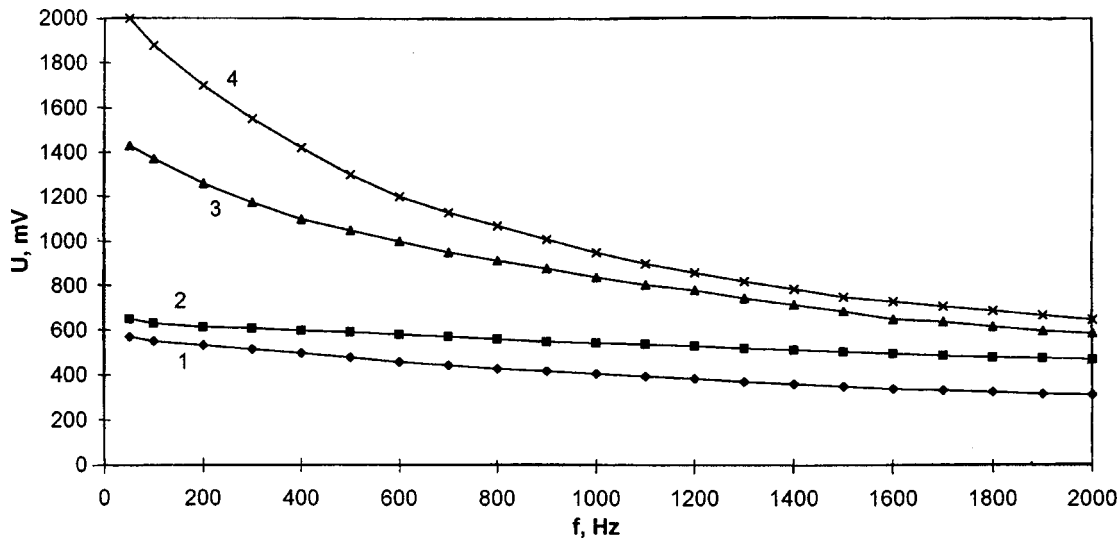


FIG. 2. Dependence of the photoresponse on the optical modulation frequency for films having two compositions: *1*, *2* — ''pure'' CdS(Se), *3*, *4* — CdS with added PbS. Curves *1* and *3* were obtained after electron beam bombardment and curves *2* and *4* were obtained before bombardment.

entire volume of the semiconductor. In our view the second scenario is more likely and the enhanced sensitivity observed after bombardment (low-dose effect) in some batches of samples with added PbS may be explained as the narrow-gap phase forming a sink for defects formed during preparation of the sample. This sink may be caused by radiation-stimulated diffusion. For instance, exposure of CdS to $\gamma$ radiation at a dose rate of $250 \, \mathrm{rad/s}$ (which is considerably lower than that used here) produces a defect diffusion coefficient $D = 10^{-12} – 10^{-11} \, \mathrm{cm^2/s}$ (Ref. 4). Then, the average crystallite (distance $0.2–0.4 \, \mu\mathrm{m}$) passes through a defect within times on the order of $10^2 \, \mathrm{s}$, which is considerably shorter than the irradiation time.

In our view, one of the most probable mechanisms for radiation-stimulated diffusion in wide-gap semiconductors is the $\Theta$ burst mechanism,[5] since recombination takes place via local levels and the energy released per recombination event is fairly high. In narrow-gap inclusions, however, $\Theta$-bursts are ineffective (interband recombination with low released energy) and thus it should be predicted that the rate of radiation-stimulated diffusion in the narrow-gap component is considerably lower than that for the wide-gap component. As a result, diffusing defects ''stick'' in narrow-gap inclusions and the wide-gap matrix is cleared of these. The migration of defects toward inclusions may also be promoted by the directional motion of carriers toward then (''electron wind''[6]) observed when a heterophase photoconductor is illuminated.[7]

The concentration of shallow traps in CdS(Se) is almost unchanged after bombardment, since a slight reduction in the photoresponse time

$$\tau_{\mathrm{ph}} = \tau(1 + n_t/n) = \tau + C n_t, \qquad (4)$$

where $n_t$ is the electron density at traps, $C = \tau/n = \tau/(\tau G)$

$=$ const at constant beam current [see Eq. (1)], can only be caused by a reduction in the lifetime $\tau$, and $\tau_{\mathrm{ph}}$ will vary less than $\tau$ (since $n_t$ usually exceeds $n$). This is observed experimentally for CdS(Se) samples. A reduction in the photoresponse time $\tau_{\mathrm{ph}}$ in CdS(Se)–PbS for constant $\tau$ implies a reduction in $n_t$, which may also be caused by the narrow-gap phase forming a sink for attachment centers.

To sum up, these investigations indicate that the addition of PbS to the initial mixture substantially improves the degradation resistance of the static characteristics, while having no stabilizing influence on the photoresponse kinetics. An analysis of the changes in the lifetime and the photoresponse times shows that these experimental data can be explained in terms of the model of a heterophase semiconductor[7] whose narrow-gap phase forms a sink for radiation-induced defects, although, as follows from Ref. 7, the role of the submicron PbS inclusions does not merely involve a getter function.

[1] *Photoconducting Films (CdS Type)*, edited by Z. I. Kir'yashkina and A.G. Rokakh [in Russian], Saratov University Press, Saratov, (1979), 192 pp.

[2] I. A. Abroyan, A. N. Andronov, and A. I. Titov, *Physical Principles of Electron and Ion Technology* [in Russian], Vysshaya Shkola, Moscow (1984), 320 pp.

[3] S. M. Ryvkin, *Photoelectric Effects in Semiconductors* (Consultants Bureau, New York, 1964; Fizmatgiz, Moscow, 1963, 494 pp.).

[4] V. S. Vavilov, A. E. Kiv, and O. R. Niyazova, *Mechanisms for Defect Formation and Migration in Semiconductors* [in Russian], Nauka, Moscow (1981), 368 pp.

[5] B. I. Boltaks, *Diffusion and Point Defects in Semiconductors* [in Russian], Nauka, Leningrad (1972), 384 pp.

[6] V. B. Fiks, *Ionic Conductivity in Metals and Semiconductors* [in Russian], Nauka, Moscow (1969), 295 pp.

[7] A. G. Rokakh, Pis'ma Zh. Tekh. Fiz. **10**, 820 (1984) [Sov. Tech. Phys. Lett. **10**, 344 (1984)].

# Determination of the parameters of gas formations in the atmosphere by reconstructing a radar image of the underlying surface

V. A. Ivanchenko and V. V. Nikolaev

*N. G. Chernyshevskiĭ State University, Saratov*
(Submitted July 17, 1998)
Pis'ma Zh. Tekh. Fiz. **25**, 73–76 (February 12, 1999)

It is shown that the distribution function of the pollutant concentration in the atmosphere can be reconstructed by analyzing the radar pattern of the underlying surface. © *1999 American Institute of Physics.* [S1063-7850(99)01302-6]

One of the major problems in ecological monitoring involves determining the parameters of gaseous pollution in the atmosphere. In many cases, an active radar method is the best way of solving this problem. For example, if the pollutant gas is capable of resonantly absorbing microwave energy, the signal power received from a reference reflector $P_A$ is related to the radiation power of the station $P_0$ as follows:

$$P_A(\omega) = P_0(\omega)\frac{GA\sigma}{(4\pi D^2)^2}$$
$$\times \exp\left(-2\chi_a(D-d) - 2\alpha(\omega)\int_0^d n(x)dx\right),$$
(1)

where $\omega$ is the frequency, $G$, $A$ are the coefficient of directionality and the effective area of the antenna, $\sigma$ is the effective scattering area of the reference reflector, $D$ is the distance between the radar station and the reflector, $d$ is the distance covered by the radiation in the pollutant gas, $\chi_a$ is the absorption coefficient of the atmosphere, $\alpha$ is the absorption coefficient of the pollutant gas per unit concentration, and $n$ is the gas concentration. By measuring $P_A$ at various distances, we can determine the average gas concentration

$$\bar{n} = \frac{1}{d}\int_0^d n(x)dx,$$

and also the size and position of gas formations which are symmetric with respect to an axis perpendicular to the Earth's surface.[1] However, the axial symmetry is only preserved in the first few moments if the gas is ejected at high pressure. Then, depending on a number of factors (such as wind, rate of gas escape, and so on), the polluted zone may have a complicated profile with a complicated distribution function of pollutant concentration.

The parameters of a complex gas formation capable of resonantly absorbing microwave energy can be determined by using the reflecting property of the surface in the area being monitored. If dispersion has no significant influence on the change in the time profile of the probe signal, it follows from Eq. (1) that in the absence of pollution

$$x_A(t) = x_0\left(t - \frac{2D}{v}\right)\frac{\sqrt{GA\sigma}}{4\pi D^2}\exp(-\chi_a D),$$

where $x_A$ is the signal at the radar station receiver, $x_0$ is the emitted signal, $t$ is the time, and $v$ is the radiation propagation velocity in the atmosphere. We shall assume that the area being monitored is a plane surface and the radar station antenna is mounted at a height $h$ above this surface. In this case, the signal received from the surface element $dS$ will be

$$dx_A(r,r',\varphi,\varphi',t) = x_0\left(t - \frac{2R}{v}\right)\frac{\sqrt{G_0 A_0}}{4\pi R^2}g(\psi_1,\psi_2)$$
$$\times \exp(-\chi_a R)f(r',\varphi')dS,$$

where $r,\varphi$ are the polar coordinates, $R = (r'^2 + h^2)^{1/2}$, the function $g(\psi_1,\psi_2)$ characterizes the angular distribution, $\psi_1 = \varphi - \varphi'$ (see Fig. 1),

$$\psi_2 = \psi_{20} - \arccos\left(\frac{h^2 + rr'}{\sqrt{(h^2+r^2)(h^2+r'^2)}}\right),$$

$$f(r,\varphi) = \frac{d}{dS}\sqrt{\sigma(r,\varphi)}.$$

Thus, the entire irradiated surface generates the following signal in the radar station receiver:

$$x_A(r,\varphi,t) = \frac{\sqrt{G_0 A_0}}{4\pi}\int_r^{\tilde{r}} x_0\left(t - \frac{2R}{v}\right)\frac{\exp(-\chi_a R)}{R^2}$$
$$\times \int_{\varphi-\psi_{10}}^{\varphi+\psi_{10}} g(\psi_1,\psi_2)f(r',\varphi')d\varphi'dr'. \quad (2)$$

We shall assume that the function $g$ has the form

$$g(\psi_1,\psi_2)$$
$$= \begin{cases} \theta(\psi_2), & \psi_1 \in [-\psi_{10},\psi_{10}] \text{ and } \psi_2 \in [-\psi_{20},\psi_{20}], \\ 0, & \psi_1 \notin [-\psi_{10},\psi_{10}] \text{ or } \psi_2 \notin [-\psi_{20},\psi_{20}], \end{cases}$$

the angle $\psi_{10}$ is fairly small and is determined by the required resolution $h \ll r$, and thus, $\psi_2(r,r') \approx \psi_{20}$, $R \approx r'$, and Eq. (2) is simplified
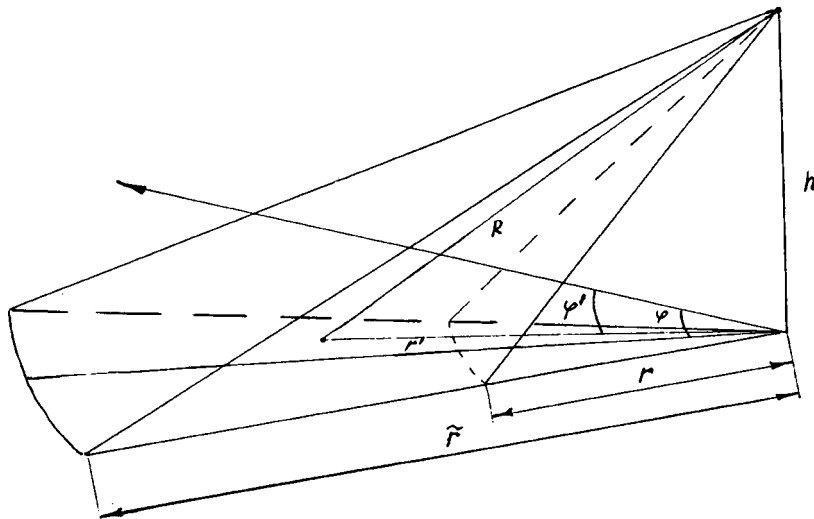
FIG. 1. Projection of angular distribution on underlying surface.

$$x_A(r,\varphi,t) = C \int_r^\infty x_0\left(t - \frac{2r'}{v}\right)\frac{\exp(-\chi_a r')}{r'^2} f(r',\varphi)dr',$$

(3)

where $C = \psi_{10}\sqrt{G_0 A_0}\,\theta(\psi_{20})/(2\pi)$. Thus the function $f(r,\varphi)$ can be determined from Eq. (3):

$$f(r,\varphi) = -\frac{r^2}{C}\exp(\chi_a r)\frac{\partial x_A(r,\varphi,t)}{\partial r}\Big/ x_0\left(t - \frac{2r}{v}\right).$$

When pollution appears whose concentration has the distribution function $n(r,\varphi)$ near the Earth's surface, the signal at the radar receiver is

$$x_A(r,\varphi,t) = C \int_r^\infty x_0\left(t - \frac{2r'}{v}\right)\frac{f(r',\varphi)}{r'^2}$$

$$\times \exp\left(-\int_0^{r'}\chi(\xi,\varphi)d\xi\right)dr',$$

(4)

where

$$\chi(r,\varphi) = \begin{cases} \alpha n(r,\varphi), & n(r,\varphi) \neq 0, \\ \chi_a, & n(r,\varphi) = 0 \end{cases}$$

(it is also assumed that radiation propagates at the same velocity in the pollutant gas and in the atmosphere).

Using Eq. (4), we can easily determine $\chi(r,\varphi)$:

$$\chi(r,\varphi) = \frac{\partial}{\partial r}\ln\left(-C\frac{f(r,\varphi)}{r^2}x_0(r,\varphi,t)\Big/\frac{\partial x_A(r,\varphi,t)}{\partial r}\right),$$

and thus $n(r,\varphi)$.

To conclude, the radar pattern from the underlying surface can be used to reconstruct the distribution function of the concentration of any type of pollutant gas and also the position of gas formations in the atmosphere which are capable of resonantly absorbing microwave energy.

[1] V. A. Ivanchenko and V. V. Nikolaev, Pis'ma Zh. Tekh. Fiz. **23**(24), 1 (1997) [Tech. Phys. Lett. **23**, 943 (1997)].

Translated by R. M. Durham

# Analysis of quasielastic neutron scattering in condensed media by periodic spatial filters

V. T. Lebedev and D. Torok

*B. P. Konstantinov Institute of Nuclear Physics, St. Petersburg; Institute of Solid-State Physics, Budapest, Hungary*

A method is proposed for Fourier analysis of quasielastic neutron scattering in condensed media using moving spatial filters with a periodic neutron transmission function, allowing the time correlation function of the object to be measured. © *1999 American Institute of Physics.*
[S1063-7850(99)01402-0]

Neutron studies of condensed media come up against the problem of maximizing the neutron flux density on the sample while maintaining (increasing) the resolution in terms of the imparted energies $\hbar\omega$ and momenta $\hbar\mathbf{q}$. Resolution is usually achieved by monochromatizing and collimating the beams, i.e., by using a small part of the angular and wavelength spectrum. However, Fourier methods,[1-7] determining not the initial and final neutron states (momenta, energies) but their changes, which carry information on the object, can be used to measure energies $\hbar\omega \sim (10^{-8}-10^{-9})$ eV several orders of magnitude smaller than the initial line width (neutron spin echo[1-5]) and to achieve an angular resolution higher than that permitted by the initial divergence by spatial modulation of the neutron intensity.[6] Here the principle of analyzing inelastic scattering using periodic filters is developed for the first time.[6,7]

A neutron beam (Fig. 1) having the characteristic wavelength $\lambda_0$, spectral width $\delta\lambda/\lambda_0 \ll 1$, and the spectral flux density distribution $i_{0\lambda}(X,Y)$, passes through modulator filters each having the transmission $T(Y) = [1+\cos(2\pi Y/\Lambda)/2]$, where $\Lambda$ is the period along the $Y$ coordinate. When the filters are fixed, the $\lambda$ spectrum remains unchanged but the intensity is modulated in terms of the flux density $i_\lambda(X,Y) = i_{0\lambda}(X,Y)T^2(Y)$. We shall show that the beam divergence in the directions of the axes is $\Delta\varphi_{X,Y} \ll \Lambda/L$. When the beam passes through a modulator moving at the velocity $\mathbf{U}$ along the $Y$ axis, the neutron spectrum changes since the phase of the transmission function depends on time $\Psi = 2\pi(Y_0+Ut)/\Lambda$, and the resultant spectral density $I_\lambda$ is determined by the time $\tau = mL\lambda/(2\pi\hbar)$ taken for a neutron of mass $m$ at wavelength $\lambda$ to cover the base $L$:

$$I_\lambda = \left[1 + \frac{1}{2}\cos\left(\frac{m}{\hbar}\frac{LU}{\Lambda}\lambda\right)\right]\frac{\Phi(\lambda)}{4}, \tag{1}$$

where the integrated intensity over the beam cross section is $\Phi(\lambda) = \int i_{\lambda 0}(X_0,Y_0)dX_0 dY_0$.

The time-averaged intensity is the spectral density $\Phi(\lambda)$, modulated at the "frequency" $\Omega_m = mLU/(\hbar\Lambda)$.

Scattering changes the wavelength and the direction of the neutron momentum. The scattering cross section $d^2\sigma/d\Omega d\omega \propto S(\omega,\mathbf{q})$ in the solid angle interval $d\Omega$ and the

frequency interval $d\omega$ is proportional to the scattering function of the sample $S(\omega,\mathbf{q})$ and depends on the imparted energy $\hbar\omega = -(2\pi\hbar)^2\Delta\lambda/m\lambda^3$ and the scattering vector $\mathbf{q}$. The scattered beam passes through an analyzer. The intensity is measured in two cases: $I^+$ (filters in phase) and $I^-$ (filters shifted by $\Lambda/2$). This implies that the spectral density of the scattered neutrons is multiplied by the factor $\{1 \pm (1/2)\cos[mLU(\lambda+\Delta\lambda)/\hbar\Lambda]\}/4$. Integration over $\lambda$ and $\omega$ for constant $\mathbf{q}$ gives the sum of the contributions of the energy-integrated cross section and the Fourier transform of the scattering function:

$$I^\pm(\mathbf{q},t_m) \propto \frac{I_\Phi}{16}\left[1 \pm \frac{1}{8}\int S(\omega,\mathbf{q})\cos(t_m\omega)d\omega\right],$$

$$I_\Phi(\mathbf{q}) = \int \Phi(\mathbf{q},\lambda)d\lambda, \tag{2}$$

where $t_m = m^2\lambda_0^3 UL/(2\pi\hbar)^2\Lambda$ has the dimensions of time. From this we determine the $q$-dependence of the cross section $d\sigma/d\Omega \propto (I^++I^-) = (1/8)I_\Phi(\mathbf{q})$ and the time-dependent scattering function

$$S(t_m,\mathbf{q}) \propto \frac{(I^+-I^-)}{(I^++I^-)} = \frac{1}{4}\int S(\omega,\mathbf{q})\cos(\omega t_m)d\omega. \tag{3}$$

The function (3) is the Fourier transform of the correlation function of the system $G(t_m,\mathbf{R})$ with respect to the coordinates, $S(t_m,\mathbf{q}) \propto \int G(t_m,\mathbf{R})\exp(-i\mathbf{q}\cdot\mathbf{R})d\mathbf{R}$. The time and frequency scattering functions are equivalent in terms of the information contained in them. We need to determine the resolution and the experimental range for the $S(t_m,\mathbf{q})$ measurements. The results (1)–(3) are valid for a narrow line $\delta\lambda/\lambda_0 \ll 1$ with an angular spread $\Delta\varphi_{X,Y} \ll \Lambda/L$ and the same detector aperture for analyses of scattering with small imparted energies $\hbar\omega/E_0 \ll \delta\lambda/\lambda_0$, where $E_0$ is the energy of a neutron of wavelength $\lambda_0$. The scattering analysis involves measuring the function $S(t_m,\mathbf{q})$ as a function of the time $t_m$ by varying the velocity $\mathbf{U}$, the transit base $L$, and the period $\Lambda$. The variable $t_m$ conjugate with the frequency has a upper limit $t_m = t_{max}$, which determines the resolution
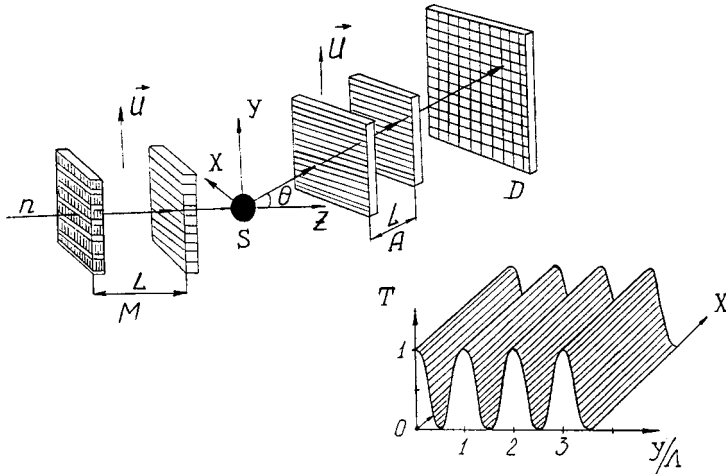
FIG. 1. Schematic of experiment: $n$ — neutron beam, $M$ and $A$ — modulator and analyzer formed by filters at the distance $L$, moving at the velocity $U$; $S$ — sample scattering neutrons through an angle $\theta$ in the $(X,Z)$ plane; $D$ — detector. The transmission function $T(X,Y)$ is shown.

$\hbar\omega_{min} \sim \hbar/t_{max}$. The upper frequency limit is not determined by the time, which may be zero, but by the condition $\hbar\omega/E_0 \ll \delta\lambda/\lambda_0$.

We shall estimate the resolution of the method for typical parameters of a small-angle neutron experiment. Assuming that the divergence is $\Delta\varphi_{X,Y} \sim 1\times10^{-3}$ rad, we obtain the permissible ratio $\Lambda/L \leq 1/4\Delta\varphi_{X,Y}$ and the maximum $L/\Lambda \sim 250$. For $\lambda_0 = 2$ nm neutrons passing through rotating filters on a rotor of diameter 50 cm at frequency $f \sim 100$ Hz (6000 rpm) with the linear velocity $U = 1.6\times10^4$ cm/s, we obtain $t_{max} \sim 2\times10^{-9}$ s and the resolution $\hbar\omega_{min} \sim 3 \times 10^{-7}$ eV. The resolution $\hbar\omega_{min}/E_0 \sim 1.5\times10^{-3}$ is not an extreme value and was estimated for normal (not excep-

tional) parameters. It can be obtained for a small transit base. For example for $\Lambda \sim 1$ mm we have $L \sim 25$ cm. We define the spectrum $\Phi(\lambda) = \exp[-(\lambda/\lambda_0-1)^2/2\sigma^2]$ of width $\sigma/\lambda_0 = 0.1$ and the relative line broadening $\Gamma\hbar/E_0 = 10^{-3}$ for scattering with the function $S(\omega) \propto 1/(\omega^2+\Gamma^2)$, which corresponds to the time function $S(t_m) = \exp(-t_m\Gamma)$. An example of the modulation of the spectrum as given by Eq. (1) is shown in Fig. 2a. A numerical simulation of the experiment (Fig. 2b) for these parameters in the range $0 \leq (t_m\Gamma) \leq 1$ yields values of the scattering function close to the accurate function $S(t_m) = \exp(-t_m\Gamma)$. The relative difference is in the range $\delta S \leq 1.4\%$ and is only caused by the finite spectral width.
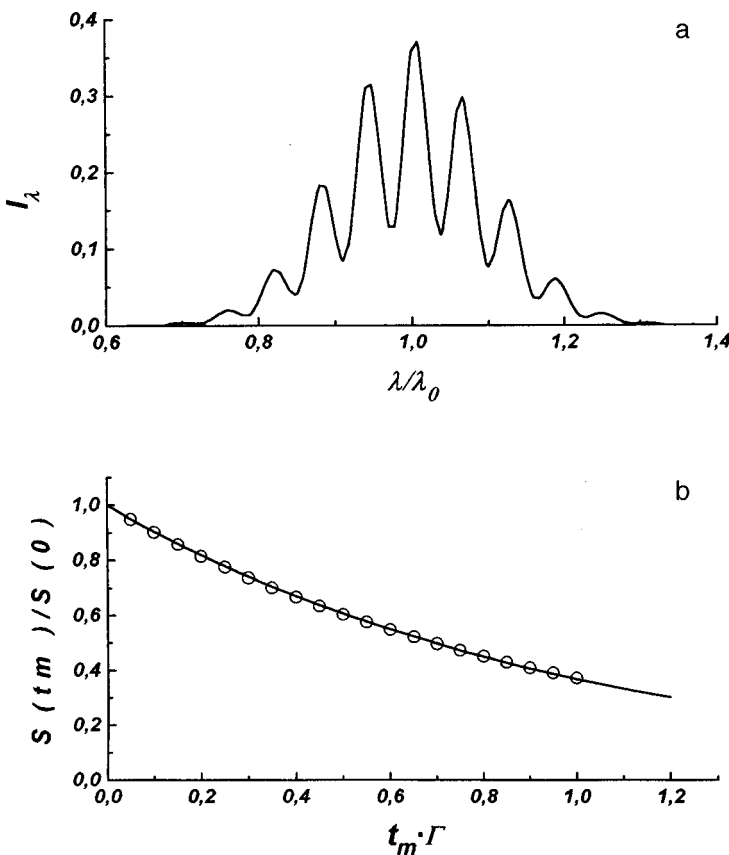




FIG. 2. Conversion of the spectrum (a) by moving modulator filters (with the parameter $t_m\Gamma = 0.05$) and resultant scattering function (b) obtained by a numerical simulation of the experiment (circles) compared with the accurate function $S = \exp(-t_m\Gamma)$ shown by the curve.

The proposed principle can be used to analyze inelastic scattering with a resolution appreciably exceeding that permitted by the initial line width (in this example, two orders of magnitude higher). It can be compared with the resolution of the spin echo method, although it does not require polarized light. This removes the constraints of the polarized neutron technique and extends the range of application of the Fourier method (cold, thermal, and hot neutrons). It can also be applied to molecular beams in general.

The authors are grateful to I. N. Ivanova for assistance with preparing this work.

[1] F. Mezei, Z. Physik. **255**, 146 (1972).
[2] *Neutron Spin Echo*, edited by F. Mezei, Lecture Notes in Physics Vol. 128 (Springer-Verlag, Berlin, 1980), 253 pp.
[3] V. T. Lebedev and G. P. Gordeev, Pis'ma Zh. Tekh. Fiz. **11**, 820 (1985) [Sov. Tech. Phys. Lett. **11**, 340 (1985)].
[4] B. Farago and F. Mezei, in *Proceedings of the International Conference on Neutron Scattering*, Santa Fe, 1985.
[5] V. T. Lebedev, G. P. Gordeev, and B. P. Toperverg, Physica B **213/214**, 990 (1995).
[6] V. T. Lebedev, A. D. Dudakov, L. Cser, L. Rosta, and Gy. Torok, J. Phys. (Paris) Suppl. IV **3**, Colloq. C8, 481 (1993).
[7] V. T. Lebedev, *Microbeam Fourier Time of Flight Spectrometer*, Preprint PNPI.N.2004 [in Russian], Gatchina (1994), 7 pp.

Translated by R. M. Durham

# Application of fractals to the analysis of friction processes

S. Yu. Tarasov, A. V. Kolubaev, and A. G. Lipnitskiĭ

*Institute of Strength Physics and Materials Science, Siberian Branch of the Russian Academy of Sciences, Tomsk*

An attempt is made to estimate the fractal dimension of the lateral surface of a steel sample formed as a result of friction by analyzing an image obtained using a scanning electron microscope. © *1999 American Institute of Physics.* [S1063-7850(99)01502-5]

The deformation of a solid (under tension or compression) is accompanied by the formation of a relief on the surface whose form reflects the degree of deformation inside the material. Since the deformation process is self-consistent, a surface relief having scaling properties may form. An estimate of the upper limit of the dimensions of the scaling structures can be used to assess the degree of spatial correlation of the deformation process. An estimate of the fractal dimension also indicates the actual surface area[1] and to some extent the nature of the energy dissipation accompanying the deformation.[2]

Under friction conditions, in addition to the volume strain, other factors caused by the specific loading characteristics also influence the formation of the surface relief in solids. In this case, the deformation is initially localized in the surface layer and then extends into the material. Under steady-state friction the deformed layer of material has a fragmented structure with fragment sizes of $\sim 0.01$ $\mu$m (Ref. 3). The reliefs formed during friction and wear at the friction surface and at the lateral surface of the sample caused by deformation of the material in the friction zone are very different and depend on the test conditions. It is naturally desirable to relate the geometric characteristics of the surface (such as the fractal dimension) to the nature of the surface layer deformation. Moreover, scanning electron microscopy can easily be used to determine the fractal dimension of a rough surface by analyzing the secondary electron intensities.[4]

Here we attempt to estimate the fractal dimension of the lateral surface of alloyed 36NKhTYu steel after friction in various regimes by analyzing SEM images of the lateral surface, which had been previously polished to a high degree. This indirect method of studying the self-similarity of friction structures is used because the friction surface itself is severely distorted as a result of wear and smearing of previously removed wear particles. Friction tests were carried out using a standard UMT-1 system without lubricant using a ''finger–disk'' system. The structure of the worn samples was studied using an RÉM-200 scanning electron microscope. The image was fed to a computer via an interface card.

To quantify the fractal properties of the sample surface, a numerical analysis was made of the SEM images using a technique which assumes that the grating line may be considered to be the surface profile along the scanning line if allowance is made for the brightness of the image at each point on this line.[5] The change in brightness is proportional to the slope of the curve at each point on this line. This approach to the interpretation of the SEM images can be used to calculate the fractal dimension ($d_{sem}$) of the surface. In our case, $d_{sem}$ was determined from the linear section of a graph of $\log_{10}(\langle |J - J'| \rangle)$ as a function of $\log_{10}(x)$, where $x$ is the distance between two elements of the scanned surface, and $J$ and $J'$ are the number of secondary electrons collected from these elements at the collector, expressed in terms of the pixel brightness of the SEM image. The angular brackets denote averaging over all the surface elements corresponding to this distance $x$. The direction of the rectilinear sections on the logarithmic plot indicates some self-similarity of the surface relief on specific scales. It was noted by Ivanova *et al.*[2] that the fractal dimension of the fracture surface calculated using this technique correlates quite clearly with the fracture energy. An investigation of the fractal dimension of the surface of a deformed solid also revealed consistency between the fractal dimension calculated from the SEM images and the degree of deformation of the solid.[5]

Figure 1 shows the friction surface of a 36NKhTYu steel sample (a) and the lateral surfaces (b, c) of the same sample after tests in various regimes. The lateral surface clearly shows a relief caused by plastic deformation during friction. With increasing distance from the friction surface, the degree of deformation of the material decreases.

An analysis of the electron images of the lateral surface in the deformation zone using the method described above yielded the results plotted in Fig. 2. Each figure shows different friction regimes: Fig 2a shows oxidizing wear where the wear is uniform and steady-state, while Fig. 2b shows intensive adhesive wear with mixing and transport of material in the friction zone. The calculated points are approximated by straight lines whose slope with respect to the abscissa gives the fractal dimension of the surface for the particular scale of the SEM images. The figures clearly show an interval on the abscissa given by the linear sections, which indicates the region of existence of self-similarity of the surface relief. Outside this interval no self-similarity exists.

This result evidently indicates that at any given time the friction process is accompanied by deformation, which does
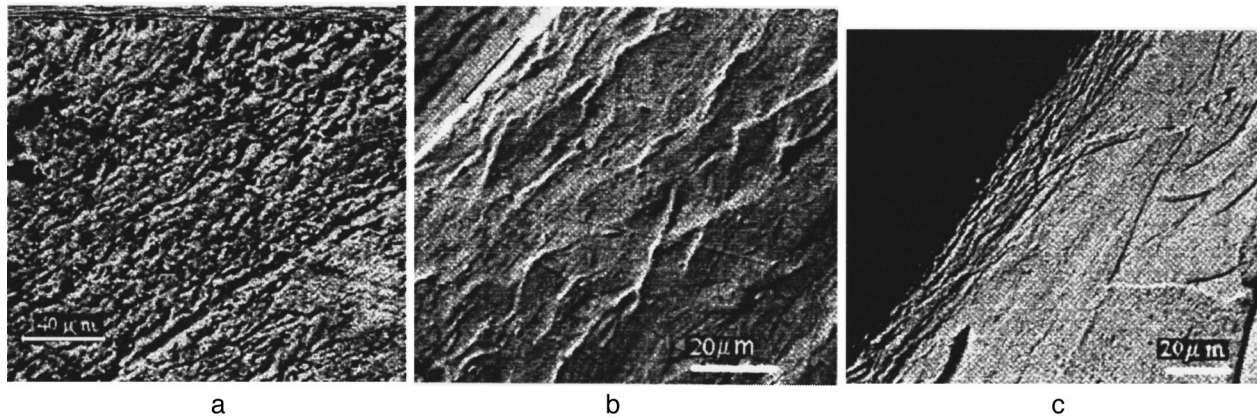
FIG. 1. Friction surface of 36NKhTYu steel sample (a) and lateral surfaces of the same sample after testing under different degrees of loading (b, c).

not embrace the entire friction surface but is localized in regions associated with the points of contact. Subsequently other sections of the sliding surface undergo deformation, and after some time the entire surface layer participates in the deformation process. However, this deformation consists of isolated deformed regions whose relief is intercorrelated only within the limits corresponding to the size of the contact spot. This type of deformation under friction may explain why the relief exhibits self-similarity in a bounded range of scales. In addition, the region of existence of the scaling gives an idea of the dominant structural mesolevel of the plastic deformation process of the surface layer under friction. In our case, the elementary structural volume responsible for the deformation and formation of a self-similar surface relief is a $0.01\,\mu$m fragment of the crystal structure. This is indicated by the lower limit for the existence of scaling. The upper limit of self-similarity of the surface relief sections depends on external factors, i.e., the load and strain rate, and is evidently determined by the size of the deformed region associated with the contact spot.

An analysis of the experimental results revealed that within the limits of action of a single dominant wear mechanism the surface relief and its characteristics are relatively constant, whereas the wear is proportional to the pressure and strain rate. This indicates that the wear intensity cannot be characterized by the fractal properties of the surface. A change in the wear regime, such as a transition from oxidizing to adhesive wear, is accompanied by a change in the fractal properties of the friction surface and the lateral surface of the sample. In this case, the wear is characterized by a fragmented layer of appreciable thickness[3] (up to 30–40 $\mu$m) and highly active transport processes, oxidation, and dynamic recrystallization at high temperatures. In our view, saturation due to defects and small structural elements promotes these processes. The possibility of the layer dissipating energy by forming new surfaces leads to a change in the fractal characteristics. The increase in the degree of dissipation of the fracture energy under these conditions may be compared with an increase in the SEM fractal dimension of the friction surface, as in studies of fracture surfaces. A change in the scaling correlation scale of the surface sections

corresponds to an increase in the structural level responsible for the energy dissipation.

Figure 3 gives results of calculations of the SEM fractal dimension of the lateral surface obtained for different mag-
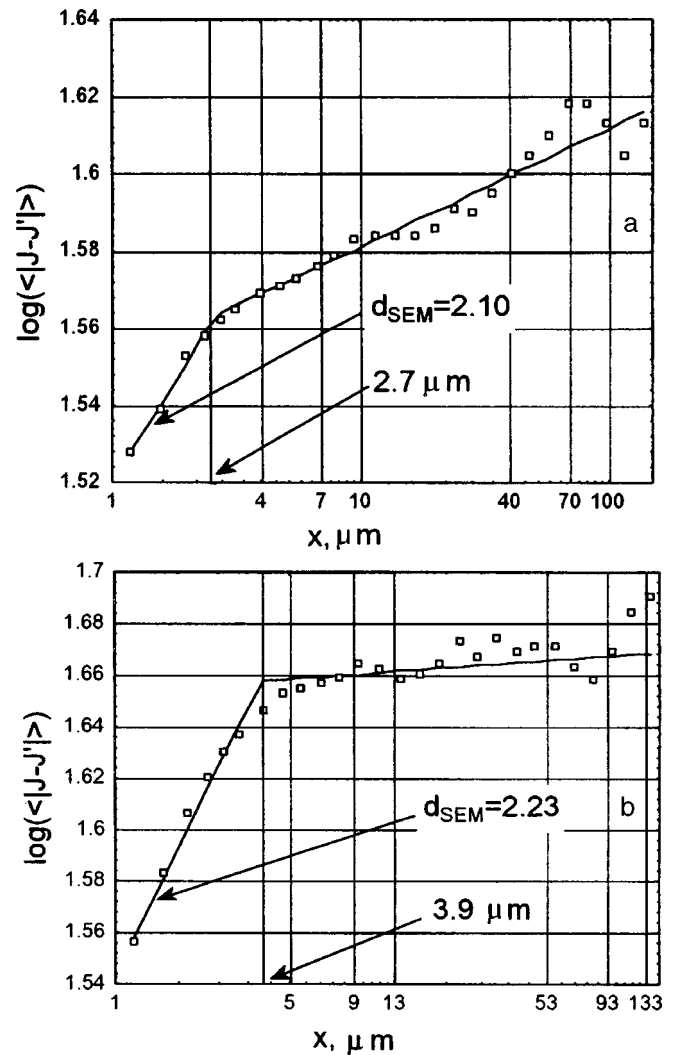


FIG. 2. Dependence of $\log_{10}(\langle |J-J'| \rangle)$ on $x$ obtained by scanning SEM images of the lateral surface: a — oxidizing wear, b — adhesive wear.
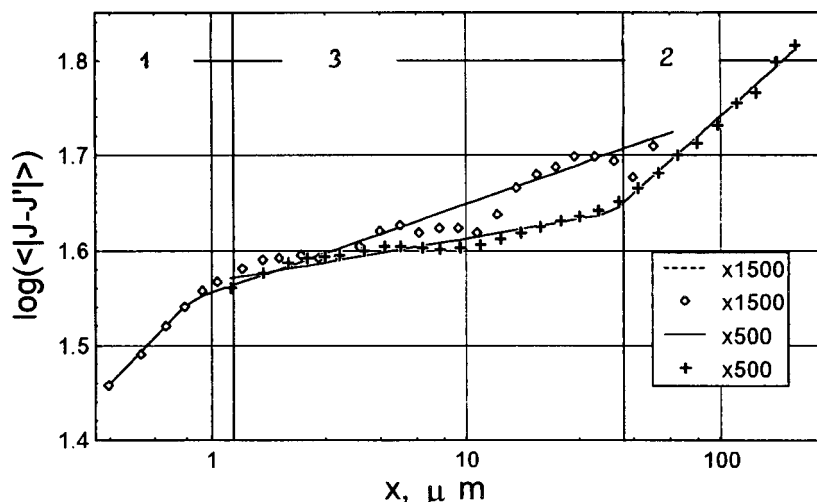
FIG. 3. Results of calculation SEM images for two magnifications: *1* — first mesolevel, *2* — second mesolevel, and *3* — region with no correlation.

nifications. A comparison between the experimental points and the straight lines approximating these calculated for various magnifications reveals two structure scales with intensities correlating according to a power law. At 1500 magnification the relief of the lateral surface exhibits scaling behavior for image sections from 1 $\mu$m and smaller (as was noted above). In the range between 1 and $\sim 40\,\mu$m no scaling behavior is observed. From $40\,\mu$m an intensity correlation is observed (on both curves!). This factor may suggest that a self-similar relief formed on the surface with a minimum structural element of $40\,\mu$m. The agreement between this scale and the thickness of the fragmented layer is remarkable. The appearance of this scale is clearly caused by the evolution of deformation on a higher mesoscopic level as a result of the migration of elements of the surface layer as a whole. This motion is promoted by vortex structures which are observed during deformation of this layer and also by large wear particles whose size is comparable with the thickness of the fragmented layer. We also note that the deformation on this mesoscopic level extends to large depths of $100\,\mu$m or more.

To conclude, the application of this method to study the deformation of surface layers of materials under friction is extremely interesting, since it provides information on the mass transfer kinetics. A correlation can also be established between the relief of the deformed surface and the friction regimes. Of particular note in this context is that the deformation caused by friction takes place on different scale levels, which may be identified from measurements of the regions of existence of self-similar structures. We established that the transition to intensive adhesive wear is accompanied by the appearance of a higher mesoscale level for which the size of the deformation structural element is the same as the fragmented layer thickness.

[1] A. I. Olemskoĭ and A. Ya. Flat, Usp. Fiz. Nauk **163**(12), 1 (1993) [Phys. Usp. **36**, 1087 (1993)].

[2] V. S. Ivanova, A. S. Balankin, and I. Zh. Bunin, *Synergetics and Fractals in Materials Science* [in Russian], Nauka, Moscow (1994), 383 pp.

[3] S. Yu. Tarasov and A. V. Kolubaev, Izv. Vyssh. Uchebn. Zaved. Fiz. **8**, 9 (1991).

[4] Z. H. Huang, J. F. Tian, and Z. G. Wang, Mater. Sci. Eng., A **118**, 19 (1989).

[5] V. E. Panin, P. V. Kuznetsov, E. E. Deryugin, S. V. Panin, and T. F. Epsukova, Fiz. Met. Metalloved. **84**(2), 189 (1997).

Translated by R. M. Durham

# Spiral wave self-organization in a coupled-map lattice: hydrodynamic scaling

V. I. Sbitnev

*B. P. Konstantinov Institute of Nuclear Physics, Russian Academy of Sciences, St. Petersburg*
(Submitted April 14, 1998)
Pis'ma Zh. Tekh. Fiz. **25**, 89–94 (February 12, 1999)

The dimensions of spiral waves reveal a scaling correspondence with the diffusion length, which is a fundamental unit of length in a coupled map lattice. © *1999 American Institute of Physics.* [S1063-7850(99)01602-X]

Coupled-map lattices supporting space–time chaos[1,2] are of extremely great interest for various reasons. Perhaps the most important of these is the possibility of applying these maps to solve the problem of synthesizing information where dynamic chaos may play a constructive role.[3,4] A "cellular neural network" in which the working elements are Chua circuits[5] is an excellent example of a technical realization of these maps. This net can reproduce a wide range of space–time patterns, which makes it fairly popular.

Among all the patterns formed as a result of space–time chaotic activity, only a few are attracting attention in research into the self-organization of dynamic structures.[6,7] Spiral waves (Fig. 1) are among these patterns. The arm of a spiral wave can extend over large distances, although the interaction between its constituent active elements is usually short-range. In order to describe this effect, it is sufficient to allow only for diffusion between neighboring elements of the active medium.[8] In this type of interaction the formation of patterns with long-range spiral-wave ordering comes as a surprise. For this reason, these dynamic structures are attractive objects for studying the self-organization mechanisms which form the basis of information synthesis.

Spiral-wave self-organization was observed in a two-dimensional coupled-map lattice.[9] There is a wide range of variations of the control parameters for which this self-organization is a generic property of this lattice. The present paper describes the scaling characteristics of these spiral waves. They are homologous to the similar characteristics in the hydrodynamics of turbulent flows.[10]

The coupled-map lattice has the following form:[11]

$$x_{n,m}^{t+1} = (1-\epsilon)u_{n,m}^t + \frac{q_e}{1+\exp(-\beta(u_{n,m}^t - v_e))}$$
$$-q_i \theta(x_{n,m}^t - v_i),$$
$$u_{n,m}^t = x_{n,m}^t + \zeta\Delta_{n,m}^t. \tag{1}$$

The subscripts $n,m = 1, 2, \ldots, N$ determine the position of the points on a lattice of dimensions $N^2$ and $t$ is the discrete time. The key parameters are $q_e$ and $q_i$ (Ref. 9). Here they are fixed, $q_e = 40$ and $q_i = 80$. The thresholds $v_e$ and $v_i$ are dependent parameters[12] and are expressed in terms of $q_e$ and $q_i$ as follows:

$$v_\nu = \ln(q_\nu + \exp(-q_\nu)), \quad \nu = e, i. \tag{2}$$

The parameter $\beta$ in the sigmoid function is an analog of the reciprocal temperature. For simplicity this parameter is taken to be unity.

The lattice points are interrelated by means of diffusion:

$$\Delta_{n,m}^t = \frac{\sum_{j,k} \bar{\omega}_{n+j,m+k} x_{n+j,m+k}^t}{\sum_{j,k} \bar{\omega}_{n+j,m+k}} - x_{n,m}^t. \tag{3}$$

Here the subscripts $j$ and $k$ have the values $-1, 0, 1$. The term $\bar{\omega}_{n+j,m+k}$ is unity, provided that $n+j$ and $m+k$ are within the range $[1,N]$, and $|j|+|k| = 1$. Otherwise, this term is zero. Analytically this term is expressed in the form

$$\bar{\omega}_{n+j,m+k} = \delta_{|j|+|k|,1}\, \theta(n+j)\, \theta(m+k)\, \theta(N+1$$
$$-(n+j))\, \theta(N+1-(m+k)). \tag{4}$$

The step function $\theta(x)$ is zero for $x \leq 0$ and unity for $x > 0$; $\delta_{|j|+|k|,1}$ is the Kronecker delta function. The diffusion term defined in the form (3) introduces closed boundary conditions.[9]

The diffusion coupling force is regulated by the parameter $\zeta$. To within the factor 1/4 this is a dimensionless diffusion coefficient with its range of variation lying in the interval $[0,1]$. The parameter $\epsilon$ characterizes the reciprocal time for linear relaxation of the variable $x_{n,m}^t$ to the rest state.[4] On the basis of these two parameters, we can introduce the length unit

$$l_D = \sqrt{\zeta\,\epsilon^{-1}}, \tag{5}$$

which quite clearly is the diffusion length. This length represents the short-range scales, whereas the dimensions of the spiral waves (Fig. 1) are an order of magnitude larger.

We shall estimate the size of the spiral from its pitch, which is the shortest distance between neighboring turns of the spiral,

$$l_S = \sqrt{(n_1-n_2)^2 + (m_1-m_2)^2}. \tag{6}$$

Here $(n_1,m_1)$ and $(n_2,m_2)$ are the coordinates selected far from the center of the spiral on the inner or outer generatrices of its arm, between neighboring turns. Figure 2 gives the results of measuring the distances $l_S$ for various $\epsilon$, with $\zeta$ being set near the saddle-node bifurcation point $\zeta_b \sim 1 - \epsilon$
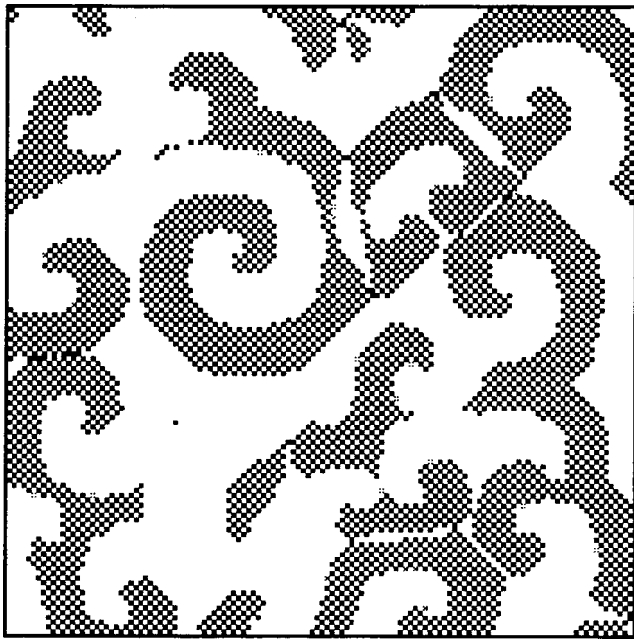
FIG. 1. Spiral waves formed as a result of setting random initial conditions in a coupled-map lattice ($I$) of dimensions $N^2 = 128 \times 128$. The variable $y^t_{n,m} = \theta(x^t_{n,m} - v_i)$ is mapped, this being zero for $x^t_{n,m} \leq v_i$ (white map) and unity for $x^t_{n,m} > v_i$ (black map). The lattice parameters are $q_e = 40$, $q_i = 80$, $\epsilon = 0.2$, $\zeta = 0.866$ ($l_D \approx 2.08$).



FIG. 2. Pitch of spiral arm $l_S$ for various $\epsilon$ (squares). The solid line gives the function $l_D$, preliminarily multiplied by the scale factor $\chi$ (in this case $\chi = 10.0$). The graph is a log–log plot.

(Refs. 4 and 9). Also plotted is $l_D$ with a preselected scale factor $\chi$, which ensures that this is matched with $l_S$. It can be seen that the two behave similarly:

$$l_S \propto l_D. \tag{7}$$

The scale factor $\chi = l_S / l_D \gg 1$ indicates the succession of the kinetic and hydrodynamic approaches in the description of the activity in the coupled-map lattice (1). In hydrodynamic problems there is a small parameter known as the Knudsen number **Kn**, which indicates a similar relationship.[10] In our case, this parameter is $\chi^{-1}$.

It is possible to isolate various characteristic lengths $l_D$ within which a qualitative difference is observed in the self-organization of the spiral waves: a) $l_D < 1$: the lattice does not exhibit any characteristics indicative of the spontaneous creation of spiral tips; b) $1 < l_D < 2$: spontaneous creation of such tips may be observed over these lengths; c) $l_D \geq 2$: in this case there is sufficient room for spiral arms to form (Fig.
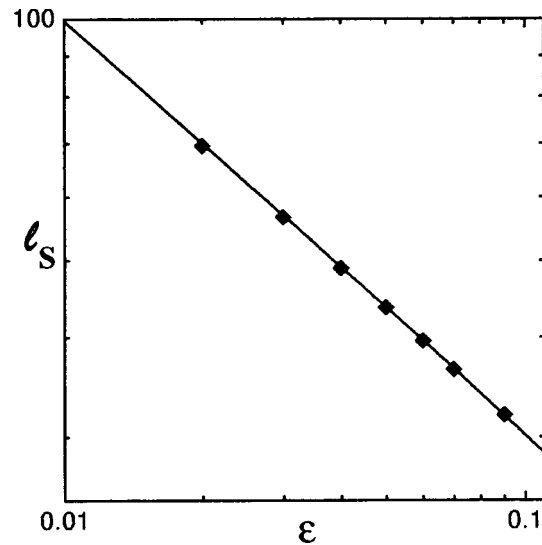
1); d) $l_D \gg 2$: as the parameter $l_D$ increases, the curvature of the spiral arm decreases. As a result, the spiral arm is an unstable object and decays. The range $1 < l_D < 2$ is given separately, since it has the center of the spiral as its significant component.[13]

[1] K. Kaneko, Prog. Theor. Phys. **74**, 1033 (1985).

[2] K. Kaneko, Physica D **34**, 1 (1989).

[3] V. S. Afraĭmovich, M. I. Rabinovich, and V. I. Sbitnev, Pis'ma Zh. Tekh. Fiz. **11**, 338 (1985) [Sov. Tech. Phys. Lett. **11**, 139 (1985)].

[4] A. O. Dudkin and V. I. Sbitnev, Biol. Cybern. 1998 (in press).

[5] L. O. Chua, Int. J. Bifurcat. Chaos **7**, 2219 (1997).

[6] H. Haken, Int. J. Bifurcat. Chaos **7**, 1927 (1997).

[7] M. C. Cross and P. C. Hohenberg, Rev. Mod. Phys. **65**, 851 (1993).

[8] Y. Kuramoto, *Chemical Oscillations, Waves, and Turbulence* (Springer-Verlag, New York, 1984), 156 pp.

[9] V. I. Sbitnev, Int. J. Bifurcat. Chaos **7**, 2569 (1997).

[10] Yu. L. Klimontovich, *Statistical Theory of Open Systems* [in Russian] TOO Yanus, Moscow (1995), 624 pp.

[11] V. I. Sbitnev, Int. J. Bifurcat. Chaos **6**, 1495 (1996).

[12] W. J. Freeman, Biol. Cybern. **33**, 237 (1979).

[13] J. M. Starobin, C. F. Starmer, and A. J. Starobin, Phys. Rev. E **56**, R3757 (1997).

Translated by R. M. Durham

# Universal nature of the instability of the thermodynamic parameters of transient processes accompanying the melting of crystalline substances in quasistatic regimes

L. A. Bityutskaya and E. S. Mashkina

*Voronezh State University*
(Submitted August 12, 1998)
Pis'ma Zh. Tekh. Fiz. **25**, 1–5 (February 26, 1999)

A numerical method of differential thermal analysis was used to study transient processes accompanying the melting of germanium and antimony in quasistatic regimes at heating rates of ~ 1 K/min. It is shown that the premelting initiation temperature and the melting initiation point are unstable and depend on the initial conditions. © *1999 American Institute of Physics.*
[S1063-7850(99)01702-4]

We have shown[1–4] that the melting of crystalline substances with different types of chemical bonds in dynamic heating regimes at heating rates $v = 5$ and 10 K/min is accompanied by the formation of excited pre- and postmelting regions and is characterized by a system of nonequilibrium thermodynamic parameters. In Ref. 5 we showed that under quasistatic heating regimes at rates $v \leq 1$ K/min the thermodynamic premelting and melting parameters of ionic KCl crystals such as the premelting initiation temperature $T'_{\text{pre-m}}$ and the melting initiation point $T_{\text{bm}}$ are unstable. We also showed that the values of these parameters depend on the initial conditions.

The aim of the present study is to identify the instability of the thermodynamic premelting parameters and the melting initiation point in quasistatic heating regimes for substances with a different type of chemical bond.

The samples were covalent crystals of germanium and antimony semimetal. Thermographic measurements were made in evacuated quartz Stepanov vessels at heating rates $v \leq 1$ K/min using a technique described by us earlier.[1–5] In order to determine the influence of the initial conditions

(sample prehistory) on the transient processes accompanying the melting of Ge and Sb the samples were heated in two regimes: for Ge (1) from room temperature to 1250 K and (2) from 1000 to 1250 K; for Sb (1) from room temperature to 1000 K and (2) from 820 to 1000 K.

The premelting exothermics change from stable cycles at $v = 5 - 10$ K/min (Refs. 2 and 3) to noisy ones at $v \leq 1$ K/min. However, the type of chemical bond imposes its own characteristics. As for KCl, for Sb at low heating rates the regions of instability are separated for heating regimes *1* and *2* (Fig. 1). Moreover, the transient premelting states at low heating rates correspond to a high dispersion $\sigma(T'_{\text{pre-m}})$, which also differs for different heating regimes. The dispersion was calculated for ten points and was found to be $\sigma_1(T'_{\text{pre-m}}) = 15.6$ for regime *1* and $\sigma_2(T'_{\text{pre-m}}) = 9.5$ for regime 2 (Ref. 6). However, whereas $\sigma_1(T'_{\text{pre-m}})$ is of the same
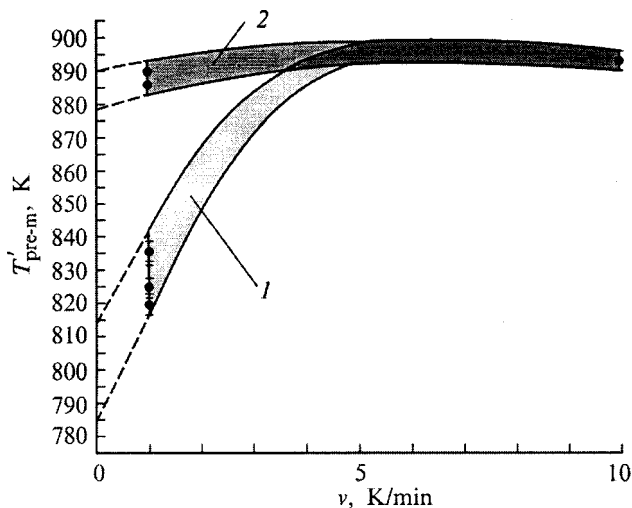


FIG. 1. Dependence of $T'_{\text{pre-m}}$ for Sb on the heating rate: *1* — heating from room temperature to 1000 K, *2* — heating from 820 to 1000 K.
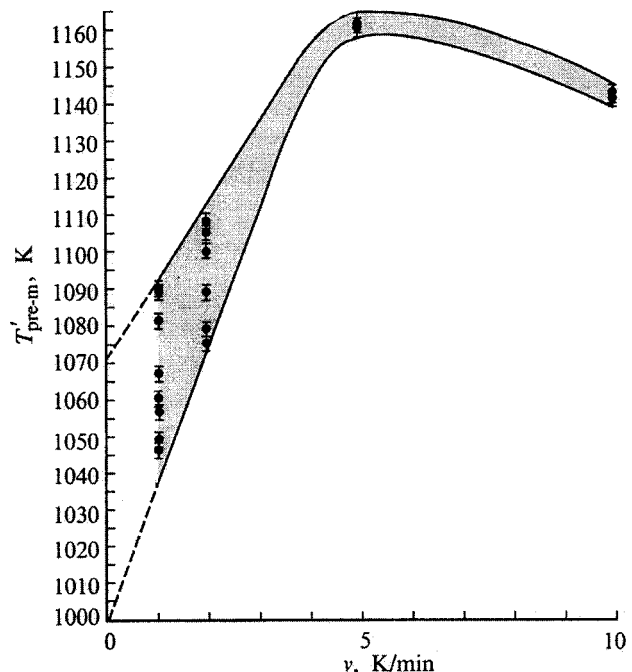


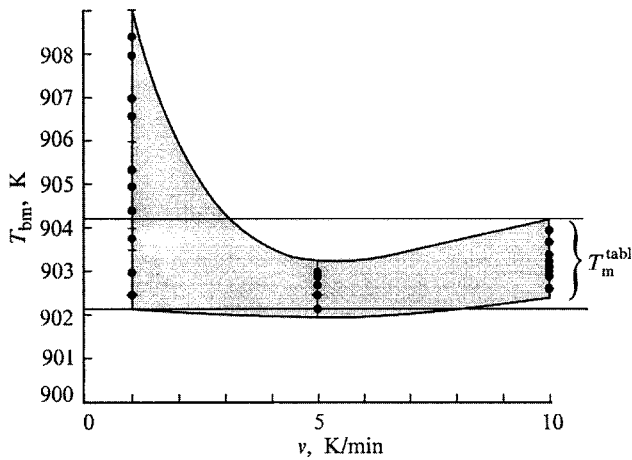FIG. 2. Dependence of $T'_{\text{pre-m}}$ for Ge on the heating rate.

FIG. 3. Instability of the melting initiation point of Sb ($T_m^{\text{tabl}}$ gives the range of tabular values of the melting point).

order of magnitude as $\sigma_2(T'_{\text{pre-m}})$ for ionic crystals, for Sb $\sigma_1(T'_{\text{pre-m}})$ is higher than $\sigma_2(T'_{\text{pre-m}})$.

Unlike KCl and Sb, covalent Ge crystals revealed no separation of the regions of instability of the premelting parameters for heating regimes *1* and *2* (Fig. 2). Moreover, the transient state corresponds to an anomalous value of the dispersion $\sigma(T'_{\text{pre-m}})$, 208.2. The average range of instability of $\sigma(T'_{\text{pre-m}})$ when extrapolated to zero rate is 65 K.

As for KCl, in anisotropic Sb crystals the instability of $\sigma(T'_{\text{pre-m}})$ at low heating rates produces instability of the melting point $T_{\text{bm}}$ (Fig. 3). Whereas for KCl the regions of instability for heating regimes *1* and *2* lie above the tabular values of $T_m$, for Sb the region of instability lies in and above the zone of tabular values[6] of $T_m$. The instability zone of $T_{\text{bm}}$ for Sb when extrapolated to zero rate is 7 K. For Sb the overheating relative to the tabular values was 4 K. However, unlike the case of ionic crystals at $v \lesssim 1$ K/min the re-

gions of instability of $T_{\text{bm}}$ are not separated. The dispersion of $T_{\text{bm}}$ was 3.96, calculated for ten points.

For Ge in the range of heating rates 1–10 K min the melting initiation point $T_{\text{bm}}$ is a stable parameter.

These results can be interpreted using the Frenkel–Khait model,[7,8] which is based on correlations in the phonon subsystems under conditions of crystal lattice anharmonicity caused by an abrupt increase in point defects. At heating rates $v \sim 1$ K/min a weakly correlated state is established in the phonon subsystem, characterized by an extended temperature–time interval, noisy cycles, sensitivity of the transient process parameters to the initial experimental conditions, and local clustering.

To sum up, a quasistatic regime with continuous heating creates instability of the thermodynamic premelting and melting parameters, which is a universal property of the melting process of crystalline materials and explains the nature of the overheating effects.

[1] L. A. Bityutskaya and E. S. Mashkina, Pis'ma Zh. Tekh. Fiz. **21**(18), 8 (1995) [Tech. Phys. Lett. **21**, 728 (1995)].

[2] L. A. Bityutskaya and E. S. Mashkina, Pis'ma Zh. Tekh. Fiz. **21**(18), 85 (1995) [Tech. Phys. Lett. **21**, 763 (1995)].

[3] L. A. Bityutskaya and E. S. Mashkina, Pis'ma Zh. Tekh. Fiz. **21**(20), 30 (1995) [Tech. Phys. Lett. **21**, 828 (1995)].

[4] L. A. Bityutskaya and E. S. Mashkina, Pis'ma Zh. Tekh. Fiz. **21**(24), 90 (1995) [Tech. Phys. Lett. **21**, 1032 (1995)].

[5] L. A. Bityutskaya, and E. S. Mashkina, Pis'ma Zh. Tekh. Fiz. **22**(21), 1 (1996) [Tech. Phys. Lett. **22**, 863 (1996)].

[6] *Handbook of Chemistry and Physics*, 33rd ed., edited by Ch. D. Hodgman (Chemical Rubber Publishing Co., Cleveland, Ohio, 1951–1952), pp 1925–1926.

[7] J. Frenkel, *Kinetic Theory of Liquids* (Clarendon Press, Oxford, 1946) [Russ. original, later ed., Nauka, Leningrad, 1975, 592 pp.].

[8] Yu. L. Khait, Phys. Status Solidi B **131**, K19 (1985).

Translated by R. M. Durham

# Investigation of the harmonic composition of the periodic solution of the Korteweg–de Vries equation

Yu. N. Zaĭko

*Volga Academy of Public Service, Saratov*
(Submitted June 2, 1998)
Pis'ma Zh. Tekh. Fiz. **25**, 6–10 (February 26, 1999)

An investigation is made of the behavior of the $n$th harmonic of the periodic solution of the Korteweg–de Vries equation as a function of the index $n$ in the intermediate region which is not usually investigated by soliton theory. The asymptotic forms obtained allow the harmonic behavior to be determined more accurately. © *1999 American Institute of Physics.*
[S1063-7850(99)01802-9]

The topic considered here is not absolutely new. We recall that studies have been made of the properties of periodic solutions of the equation

$$v_t + v v_x + B v_{xxx} = 0, \tag{1}$$

where $t$ and $x$ are the time and the coordinate, and $B$ is a coefficient whose form depends on the specific problem. Zaslavskiĭ and Sagdeev[1] showed that for solutions of Eq. (1) of the form $v(\theta)$, $\theta = x - ct$ with the period $\lambda$,

$$v(\theta) = \sum_{n=-\infty}^{\infty} a_n \exp\left(\frac{2\pi i n}{\lambda}\theta\right); \quad v(\theta + \lambda) = v(\theta), \tag{2}$$

the asymptotic dependence of the harmonic amplitudes $a_n$ on the index $n$ is given by ($c > 0$)

$$a_n \sim \begin{cases} \dfrac{3c}{N}, & n \leq N, \\[2mm] \exp(-n/N), & n \gg N, \end{cases} \tag{3}$$

where $N \sim (\pm c/B)^{1/2}\lambda$. These authors also note that this dependence is typical for periodic solutions of other nonlinear equations. The aim of the present study is to refine expression (3).

For solutions $v(\theta)$ of (1) a single integration yields the nonlinear oscillator equation $v_{xx} - (c/B)v = -(1/2B)v^2$. The theory of nonlinear operators in Banach spaces[2] states that for $\pm c/B = n^2$ ($\pm B > 0$) the $2\pi$ periodic solution of the initial Korteweg–de Vries equation has a bifurcation in the creation of the $n$th harmonic. This can be shown strictly by reducing the nonlinear oscillator equation to the Hammerstein integral equation,[2] as was done in Ref. 3. This conclusion is based on the continuity, positive definiteness, and symmetry of the kernel of the corresponding Hammerstein equation.[3]

This case has been little studied because of the even multiplicity of the characteristic values of the Hammerstein equation and the form of the eigenfunctions of its linearized part. For this reason it is difficult to make any additional general statements about the way bifurcation occurs in the creation of the next harmonic of the periodic solution of the

Korteweg–de Vries equation. However, this aspect can be investigated directly by using the known cnoidal solution of the Korteweg–de Vries equation:[4]

$$v(\theta) = \frac{2b}{s^2} dn^2(\zeta, s) + b_3; \quad s^2 = \frac{b_1 - b_2}{b_1 - b_3},$$

$$\zeta = \sqrt{\frac{b}{6B}}\frac{\theta}{s}, \quad b = \frac{b_1 - b_2}{2}. \tag{4}$$

Here $dn(\zeta, s)$ is a Jacobi elliptic function with modulus $s$. The wave amplitude is $b$; the values $b_{1,2,3}$ are constants which depend on the wave velocity $c$, where $b_1 > b_2 \geq b_3$, $b_2 \leq v \leq b_1$. The wave period is $\lambda = 2\pi = 2\sqrt{6B/b}\, s K(s)$,
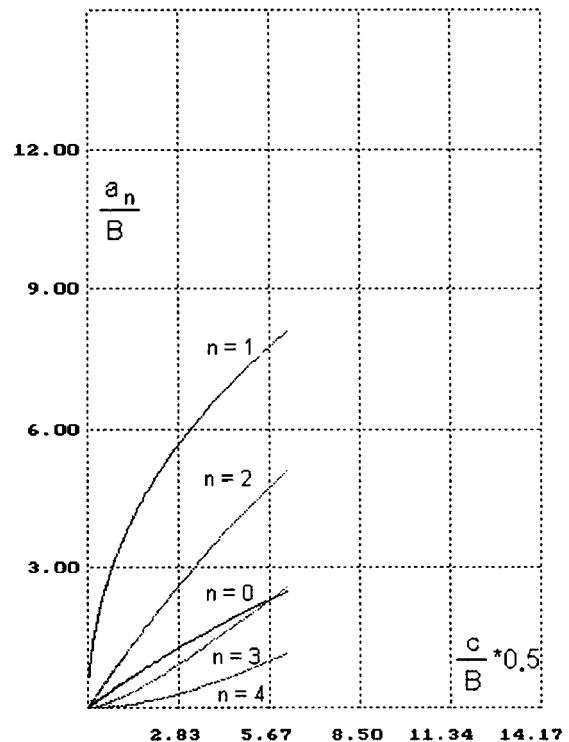


FIG. 1. Amplitude of the $n$th harmonic of the periodic solution of the Korteweg–De Vries equation (1) as a function of the parameters $c$ and $B$.
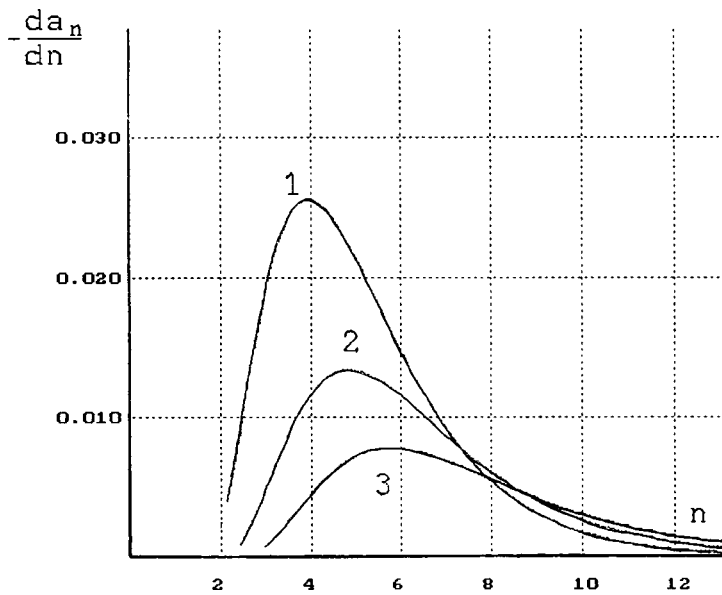
FIG. 2. The derivative $da_n/dn$ of the $n$th harmonic as a function of $n$ for various values of $c/B$: $1$ — $(c/B)^{1/2}=4$; $2$ — $(c/B)^{1/2}=5$; $3$ — $(c/B)^{1/2}=6$.

where $K(s)$ is a complete elliptic integral of the first kind. The theory of elliptic functions is used to derive expressions for $a_n$:

$$a_0 = 3B\left[\frac{4}{\pi^2}E(s)K(s)-1\right],$$

$$a_n = 6B\sum_{m=0}^{\infty}\frac{1}{\cosh(m\theta)\cosh((m-n)\theta)}, \quad n\geqslant 1,$$

$$\theta = \frac{\pi K'}{K}; \quad K=K(s); \quad K'=K(\sqrt{1-s^2}), \tag{5}$$

where $E(s)$ is a complete elliptic integral of the second kind.

Figure 1 gives the results of calculating the first few harmonics as a function of the parameter $c/B = 4\pi^2(2-s^2)K^2(s)-2$, for which the expressions and also those for the parameter $b_3 = -3B$ are obtained from the natural constraint that in the weak nonlinearity limit ($s\to 0$) the zeroth harmonic should coincide with the points $v=0$ or $v=2c$ for which the corresponding potential function $U(v) = -(c/2B)v^2+(1/6B)v^3$ has a minimum. The left-hand boundary of the range $c/B=0$ corresponds to the harmonic solutions of Eq. (1) where $s\to 0$ and the right-hand boundary corresponds to the strongly nonlinear solutions where $s\to 1$.

On the basis of these calculations, we can state that all the bifurcations are bilateral, i.e., nontrivial solutions of Eq. (1) exist on both sides of the bifurcation point. In this respect, this problem resembles the well-known Nekrasov problem of waves on the surface of water.[5] In addition, as the parameter $c/B$ passes through zero, the zeroth harmonic undergoes a finite change of $2c$ as a result of a change in the equilibrium position defined by the potential function $U(v)$.

A more detailed study of the behavior of the harmonics may be made by using the asymptotic expression for $a_n$, which can be obtained by replacing the sum in Eq. (5) by an integral for moderately small $n$:

$$a_n \sim \frac{6B}{\cosh(n\theta)}\left\{1-\frac{1}{\tanh(n\theta)}\ln\left[\frac{\cosh(1)}{\cosh(n\theta-1)}\right]\right\}, \quad n\gg 1. \tag{6}$$

Expression (6) yields various asymptotic forms for $a_n$:

$$a_n \sim \begin{cases} 6B, & n\theta\ll 1, \\ 12Bn\theta\exp(-n\theta), & n\theta\gg 1, \end{cases}$$

$$a_n = \begin{cases} -\dfrac{n}{16^n}s^{2n-4}\ln(s^2), & s\ll 1, \\[2mm] \dfrac{\pi^2}{\ln^2(1-s^2)}, & s\to 1. \end{cases} \tag{7}$$

Figure 2 gives the derivative $da_n/dn$ as a function of $n$ for various values of $c/B$, from which it can be concluded that at the bifurcation point $c/B=n^2$ the $n$th harmonic shows the maximum rate of change. As $n$ increases, the error caused by the finite accuracy of the program for calculation of the elliptic integral increases ($2\times 10^{-8}$; see Ref. 6).

[1] G. M. Zaslavskiĭ and R. Z. Sagdeev, *Introduction to Nonlinear Physics* [in Russian], Nauka, Moscow (1988), 368 pp.

[2] *Functional Analysis*, edited by S. G. Kreĭn, Wolters-Noordhoff, Groningen (1972) [Russ. original, Nauka, Moscow (1964), 424 pp.].

[3] Yu. N. Zaĭko, Pis'ma Zh. Tekh. Fiz. **18**(23), 63 (1992) [Sov. Tech. Phys. Lett. **18**, 787 (1992)].

[4] V. I. Karpman, *Nonlinear Waves in Dispersive Media* (Pergamon Press, Oxford, 1975) [Russ. original, Nauka, Moscow 1973, 176 pp.].

[5] S. A. Gabov, *Introduction to the Theory of Nonlinear Waves* [in Russian], Moscow State University Press, Moscow (1988), 177 pp.

[6] *Handbook of Special Functions*, edited by M. Abramowitz and I. A. Stegun (Dover, New York, 1965; Nauka, Moscow, 1979, 832 pp.).

Translated by R. M. Durham

# Mechanism for antiphase synchronization in neuron models

D. É. Postnov and S. K. Han

*Saratov State University;*
*Chungbuk National University, Cheongju, South Korea*
(Submitted September 2, 1998)
Pis'ma Zh. Tekh. Fiz. **25**, 11–18 (February 26, 1999)

Antiphase synchronization with weak diffusive coupling is a characteristic feature of the
dynamics of coupled neuron oscillators. We show that this effect is caused by a saddle equilibrium
state in the vicinity of an attractor and appears in the immediate vicinity of a homoclinic
bifurcation point. The mechanism discussed is a fairly general one which goes outside the scope
of neuron models. © *1999 American Institute of Physics.* [S1063-7850(99)01902-3]

One of the most rapidly developing lines of research involves studying the dynamics of neuron systems. Depending on the specific problems, the neuron models used range from the detailed four-dimensional Hodgkin–Huxley model[1] to extremely simplified one-dimensional models.[2]

One of the most important trends is the study of small ensembles, where each neuron together with the coupling between them is described by a relatively realistic mathematical model based on experimental data and concepts on the nature of the processes in nerve cells (see the review presented by Abarbanel *et al.*[3]).

The main properties of an isolated neuron are reasonably well described by two-dimensional models, the best known being the Morris–Lecar model[4] and the Hindmarsh–Rose model.[5] The most important characteristic of a neuron is that it has two functioning regimes: a state with a constant potential level (resting state) and one in which short positive pulses are generated (spikes). A transition from one state to another is caused by the action of other neurons, by electrical (synaptic current) or chemical coupling. As a result, the dynamics of these neuron models is characterized by two coexisting attractors on the phase plane, i.e., an equilibrium state and a limit cycle whose basins of attraction are separated by the stable manifold of the saddle equilibrium state. When the control parameter is varied (the synaptic current decreases), the limit cycle "gets caught" in the saddle and disappears. In terms of oscillation theory this corresponds to a nonlocal bifurcation, i.e. a saddle separatrix loop.[6] Here we show that the functioning of a neuron near this bifurcation point determines the existence of antiphase synchronization[7,8] and the unique features of the interaction of these systems.

As we know, any oscillator with a single degree of freedom may be represented in the form

$$\ddot{x} + F_1(x,\dot{x},\mathbf{p})\dot{x} + F_2(x,\mathbf{p}) = 0, \tag{1}$$

where $\mathbf{p}$ is the generalized vector of the control parameters and $F_1$ and $F_2$ are generally nonlinear functions. The corresponding transformations for neuron models (the explicit form of the functions is not given here because of their involved nature) can demonstrate the following properties:

1) $F_2$ has the form of a cubic parabola and determines the existence of three equilibrium states $P_1$, $P_2$, and $P_3$, of which the middle is a saddle $(\partial F_2/\partial x|_{P_2} < 0)$;

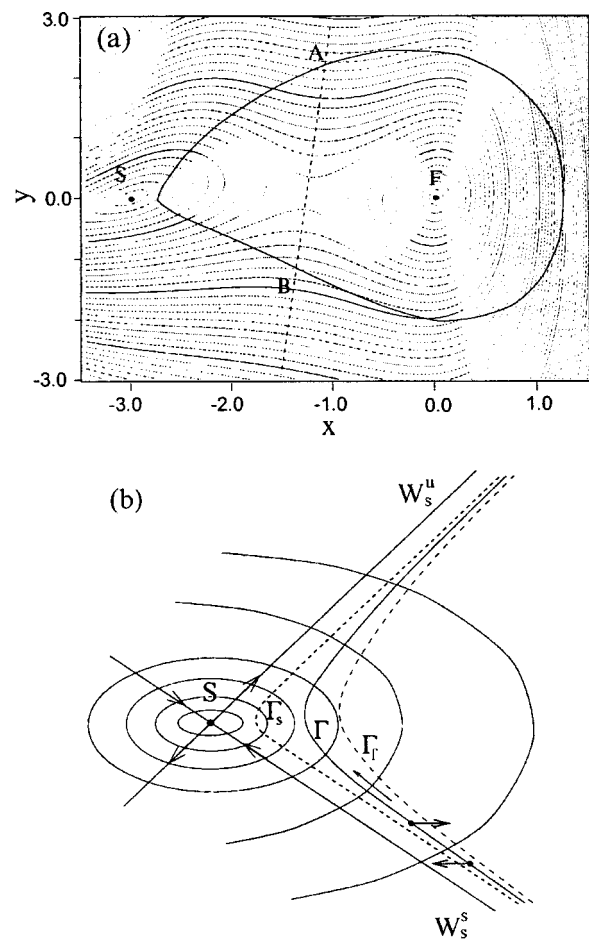2) $F_1$ ensures negative dissipation in the vicinity of $P_1$



FIG. 1. a — Contours of the phase velocity magnitude showing two qualitatively different zones in the configuration of the limit cycles shown for $\mu = 1.0$, $\varepsilon = 0.2$, $d = 3$. b — Illustration showing how diffusive coupling in terms of a single variable can increase the initial phase shift of the subsystems. $S$ — equilibrium saddle state with stable $W_s^s$ and unstable $W_s^u$ manifolds. Here $\Gamma$, $\Gamma_s$, and $\Gamma_f$ denote the unperturbed, slow, and fast trajectories, respectively.
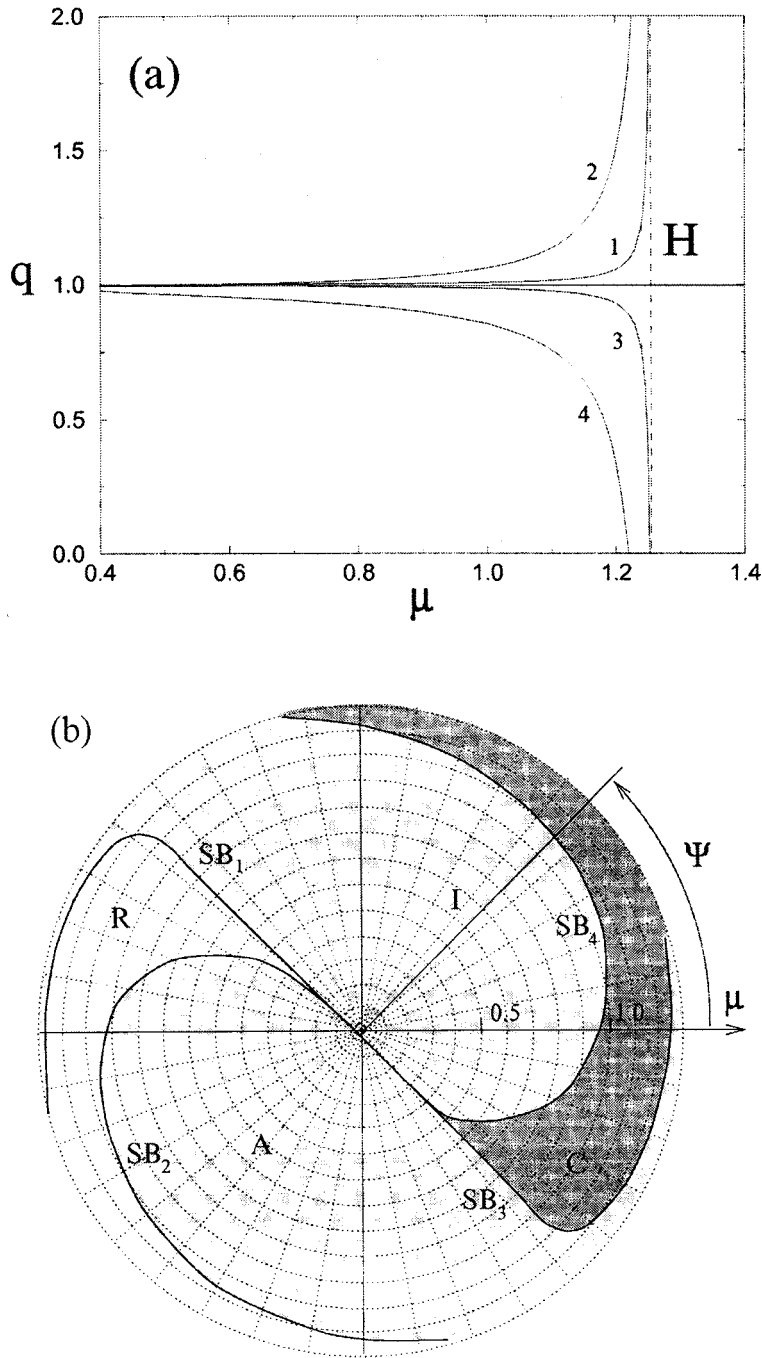
FIG. 2. a — Scattering or focusing force of subsystem trajectories near the saddle $S$ characterized by the value of $q$ as a function of the parameter $\mu$ for various forces and coupling configurations. Curves *1* and *2* — $K_y=0$, $K_x=0.001$ and 0.01, respectively. Curves *3* and *4* — $K_x=0$, $K_y=0.001$ and 0.01. In all cases the value of $p$ was $p \approx 0.996$. The line $H$ corresponds to a homoclinic bifurcation, $\mu \approx 1.255$. b — bifurcation diagram of the system (3) in the weak coupling limit. The outer boundary corresponds to the homoclinic bifurcation point $\mu \approx 1.255$. The letters indicate qualitatively different regions of behavior of the system: $I$ — uniquely stable cophasal system (the oscillations of both subsystems are identical); $A$ — uniquely stable antiphase regime (the oscillations of the subsystems are identical apart from the phase shift $\pi$); $R$ — a pair of mirror-symmetric cycles is stable; $C$ — regimes $I$ and $A$ coexist, separated by a pair of symmetric unstable cycles. $SB_i$, $i=1\ldots4$ — bifurcation curves on which symmetry is lost.

or $P_2$, making it possible for a limit cycle to exist.

This information can be used to formulate a simplified model which gives the principal properties of a neuron in a general form. In particular, conditions (1) and (2) are satisfied by taking

$$F_1 = \varepsilon(x^2 - \mu), \quad F_2 = \frac{(x+d)^3}{d^2} - (x+d), \tag{2}$$

where $\varepsilon$, $\mu$, and $d$ are control parameters. By varying the parameter $\mu$, it is possible to vary the properties of the model from those close to a classical van der Pol generator ($\mu \ll 1$) to neuron-like behavior near the homoclinic bifurcation point $\mu \approx 1.255\ldots$.

The object of our analysis below is a system of two coupled oscillators of the form (1) with allowance for (2):

$$\dot{x}_1 = y_1 + K_x(x_2 - x_1), \quad \dot{y}_1 = -F_1 y_1 - F2 + K_y(y_2 - y_1),$$

$$\dot{x}_2 = y_2 + K_x(x_1 - x_2), \quad \dot{y}_2 = -F_1 y_2 - F2 + K_y(y_1 - y_2), \tag{3}$$

where coupling in terms of both variables allows the existence of a delay (phase shift) typical of the finite speed of coupling via the neuron synapse. Quite clearly, by taking $K_x=0$ or $K_y=0$, we can convert to the more usual diffusive coupling in terms of a single variable.

By assuming weak coupling $Kx, Ky \to 0$, we can make a qualitative analysis of the system behavior by projecting the oscillations of both coupled subsystems onto the phase plane of a single model[8] (Fig. 1a). For small $\mu$ the limit cycle is positioned near $F$, where the structure of the vector field is similar to the case of a van der Pol generator. For fairly large $\mu$ the trajectory visits the zone to the left of the line $AB$ near the equilibrium saddle state $S$ which is of particular interest. Figure 1b shows a qualitative mapping of the projection of the trajectories in both subsystems onto the phase plane $(x_i, y_i)$ near $S$. Quite clearly, the singular point corresponds to the minimum of the absolute value of the phase velocity $|v_{phase}| = 0$, which is shown by the concentric contours $|v_{phase}|$. Introducing the unperturbed (in the absence of coupling) trajectory $\Gamma$ and considering the action of coupling to be a weak shift in the direction defined by $K_x, K_y$, we can conclude that

1) the action of coupling "shifts" the subsystem state point either in the direction of the "slow" trajectory $\Gamma_s$ or in the direction of the fast trajectory $\Gamma_f$;

2) the direction of the shift is determined by the relative position of the state points of the interacting subsystems and by the direction of action of the coupling.

Figure 1b shows the case where coupling shifts the trajectory of the lagging subsystem into a region of even slower motion, thereby increasing the phase shift. For the system (3) this situation is found when $K_x > 0$, $K_y = 0$. Obviously the case $K_x = 0$, $K_y > 0$ corresponds to the opposite situation.

Although the effect described above is local, it may influence the stability of the synchronous regime as a whole. Having divided the limit cycle into two zones by the line $AB$, we set these in correspondence with two mappings $P$ and $Q$ which convert some initial time shift of the subsystems $\Delta t_{A,B}$ into its transform by intersecting this line. Confining ourselves to small initial shifts $\Delta t \to 0$, we can reduce these (generally nonlinear) mappings to the coefficients

$$\Delta t_B = p \Delta t_A, \quad \Delta t_A = q \Delta t_B. \tag{4}$$

Clearly the value of $pq$ characterizes the stability ($pq < 1$) or instability ($pq > 1$) of the cophasal oscillation regime.

As was to be expected, the value of $q$ depends strongly on the closeness of the trajectory to the saddle point, i.e., on the value of the parameter $\mu$ (Fig. 2a). An abrupt increase (curves *1* and *2*) or an equally abrupt decrease (curves *3* and *4*) in the value of $q$ from the level $q = 1$ reflects the action of this mechanism.

Curves *3* and *4* were obtained for coupling an order of magnitude stronger and thus show the structural stability of this effect.

In fact, the region in the vicinity of the equilibrium saddle state $S$ acts a kind of "lens" which, depending on the coupling characteristics, "diverges" or "focuses" the initially phase-shifted states of the two subsystems.

It is clear that the direction of interaction, defined by relationship between and signs of $K_x$ and $K_y$, plays an important role in these effects. For this reason it is convenient to represent the degree of coupling as a vector with the coordinates

$$K_x = K \cos \Psi, \quad K_y = K \sin \Psi, \tag{5}$$

where $K$ is the magnitude of the coupling coefficient and $\Psi$ is its angle. Clearly, with a suitable choice of $\Psi$ we obtain particular cases of coupling in terms of a single variable.

The existence of various types of synchronous regimes of the system (3) and their stability were investigated by calculating the so-called "effective coupling" (see Ref. 9) assuming that $K \to 0$. The results are plotted in Fig. 2b.

For small $\mu$ this system behaves as two coupled van der Pol oscillators, i.e., it has regions of cophasal ($I$) and antiphase ($A$) oscillations, which is determined by the value of $\Psi$ (i.e., by the combination of signs of $K_x$ and $K_y$).

An increase in the parameter $\mu$ leads to a shift of the sectors occupied by these regimes with respect to $\Psi$ and also leads to the appearance of an additional pair of symmetrically positioned stable (in zone $R$) or unstable (in zone $C$) oscillation regimes. Thus, the influence of the equilibrium saddle state described above is observed as a change in the type of synchronization (from cophasal to antiphase or conversely) as the control parameter $\mu$ is varied.

In addition to neuron models, the mechanism described here is also relevant to various problems involving the synchronization of systems with a saddle (saddle-focus) equilibrium state near an attractor.[10,11] An example may be the well-known "Chua circuit"[12] for which coupling along different coordinates leads to cophasal or antiphase synchronization of regular and chaotic oscillations.

[1] A. L. Hodgkin and A. F. Huxley, J. Physiol. (London) **117**, 500 (1952).

[2] M. A. Arbib, in *The Handbook of Brain Theory and Neural Networks* (MIT Press, Cambridge, Mass. 1995), p. 879.

[3] H. D. I. Abarbanel, M. I. Rabinovich, A. Selverston, M. V. Bazhenov, R. Huerta, M. M. Sushchik, and L. L. Rubchinskiĭ, Usp. Fiz. Nauk **166**, 365 (1996).

[4] C. Morris and H. Lecar, Biophys. J. **35**, 193 (1981).

[5] J. Hindmarsh and M. Rose, Proc. R. Soc. London, Ser. B **221**, 87 (1984).

[6] V. I. Arnol'd, V. S. Afraĭmovich, Yu. S. Il'yashenko, and L. P. Shil'nikov, *Bifurcation Theory*, Ser. Itogi Nauki i Tekhniki, Sovr. Prob. Mat., Fundament. Naprav. [in Russian], VINITI, Moscow (1986).

[7] A. Sherman and J. Rinzel, Proc. Nat. Acad. Sci. (USA) **89**, 2471 (1992).

[8] S. K. Han, C. Kurrer, and Y. Kuramoto, Phys. Rev. Lett. **75**, 3190 (1995).

[9] Y. Kuramoto, *Chemical Oscillations, Waves, and Turbulence* (Springer-Verlag, Tokyo, 1984).

[10] E. I. Volkov and V. A. Romanov, Phys. Scr. **51**, 19 (1995).

[11] M. N. Stolyarov, V. A. Romanov, and E. I. Volkov, Phys. Rev. E **54**, 163 (1996).

[12] *Chua's circuit: A Paradigm for Chaos*, edited by R. N. Madan (World Scientific, Singapore, 1993), 1041 pp.

Translated by by R. M. Durham

# Characteristics of phase transitions in inhomogeneous silicon monoxide/chromium thin films exposed to pulsed laser irradiation

P. E. Shepelyavyĭ, V. P. Kunets, E. V. Mikhaĭlovskaya, and I. Z. Indutnyĭ

*Institute of Semiconductor Physics, National Academy of Sciences of Ukraine, Kiev*

An investigation was made of the behavior of SiO/Cr cermet films of nonuniform composition exposed to pulsed laser irradiation. It is shown that radiation-stimulated surface segregation of chromium may be observed in these films and can be used for the optical recording of information. © *1999 American Institute of Physics.* [S1063-7850(99)02002-9]

Homogeneous cermet films of silicon monoxide and chromium (SiO–Cr) have been extensively studied and are widely used in microelectronics[1] and optical technology.[2] Preliminary investigations of inhomogeneous SiO/Cr films in which the composition of the components varies continuously transversely from the insulator to the metal, have shown that these may also be of serious practical interest. For example, using these inhomogeneous films as light-absorbing matrices on screens of color picture tubes can improve the optical engineering and operating characteristics.[3] At present increasing scientific interest is being directed toward film structures with a spatially inhomogeneous composition, which reveal effects not observed in homogeneous films of the same composition.[4]

Here we describe an effect, which we are the first to observe, involving the surface segregation of metal (Cr) in inhomogeneous SiO/Cr films exposed to pulsed laser radiation.

The films were prepared by thermal evaporation of a mixture of finely dispersed chromium powder and silicon monoxide on quartz substrates in a vacuum of $10^{-3}$ Pa. As a result of the difference in the rates of evaporation of the mixture components, we obtained layers whose composition varied smoothly as a function of depth: the SiO content in the deposited layer decreased with increasing thickness while the Cr content increased. The distribution of the concentration of SiO and Cr components over the film thickness was given in Ref. 3. After deposition the layers were treated with a 15% aqueous solution of HCl to remove metallic Cr from

their surface. The thickness of the films was 100–200 nm. The films were irradiated by nitrogen laser pulses ($\lambda = 337.1$ nm) of 8 ns duration and $\sim 10^3$ W output power. The radiation was focused to a light spot of diameter 150–200 $\mu$m using an optical system which increased the power density to $10^6$–$10^7$ W/cm$^2$. The power density was varied by inserting calibrated glass attenuator plates into the unfocused part of the light beam.

The action of unfocused radiation pulses on an inhomogeneous SiO/Cr film did not cause any visible changes of its surface. When the power density reached $\sim 4 \times 10^6$ W/cm$^2$, distinct spots could be identified on the surface of the film at the irradiation sites and these exhibited a characteristic metallic luster and sharp edges approximately corresponding to the size of the irradiated zone. Figure 1a shows a photomicrograph of these spots on the surface of SiO/Cr film obtained by moving the sample in the focal plane of the focusing system. The high contrast at the illuminated sites indicates a substantial change in the reflection coefficient of the layer. Unlike the inhomogeneous SiO/Cr layers, SiO–Cr layers of homogeneous composition obtained by coevaporating SiO and Cr and irradiated under similar conditions showed negligible changes in the surface at the irradiated sites (Fig. 1b). At intensities in excess of $(6-8) \times 10^6$ W/cm$^2$ both the homogeneous and the inhomogeneous layers sustained thermal damage.

In order to obtain a quantitative estimate of the observed changes in the reflection of these inhomogeneous SiO/Cr
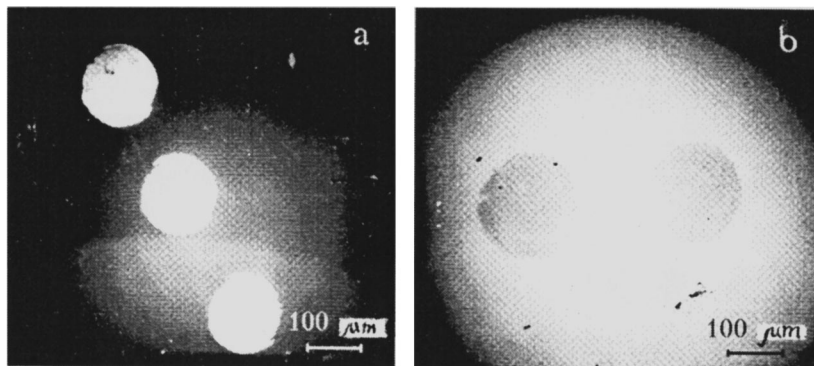


FIG. 1. Photomicrograph of the surface of cermet SiO/Cr films of inhomogeneous (a) and homogeneous (b) composition after exposure to laser pulses of intensity $4 \times 10^6$ W/cm$^2$.
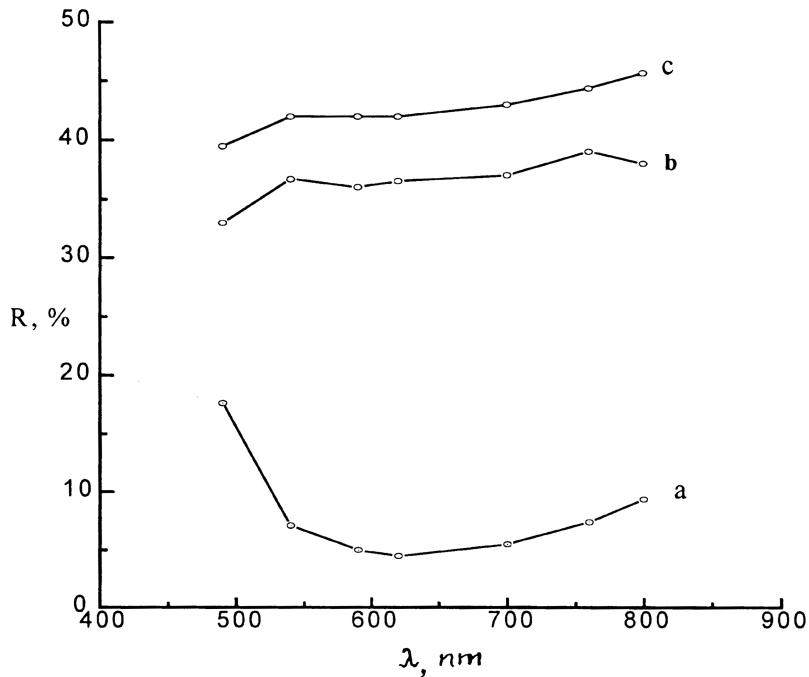
FIG. 2. Spectral dependence of the reflection coefficient of unirradiated (a) and irradiated (b) inhomogeneous SiO/Cr structures and reflection spectrum of the deposited Cr layer (c).

films exposed to nitrogen laser radiation, we measured their reflection coefficient $R$ before and after irradiation by single pulses of intensity $\sim 4 \times 10^6$ W/cm$^2$. The spectral curves $R(\lambda)$ are plotted in Fig. 2. A comparison shows that after pulsed laser irradiation, the values of $R$ measured at the free surface of the SiO/Cr film increase by almost an order of magnitude. For example, in the 620 nm range the reflection from the unirradiated film is $\sim 0.04$, whereas after exposure to a single pulse it is approximately 0.37. The increase in $R$ is observed over the entire visible range and does not depend on which side (substrate or layer) the laser pulse acts. This substantial increase in $R$ indicates that under the action of the laser radiation, the free surface of the inhomogeneous SiO/Cr layer becomes enriched in the Cr metal component. This is also evidenced by the visually observed metallization. Irradiation on the substrate side does not alter the pattern: Cr is again released on the free surface side. The similarity between the reflection coefficients $R(\lambda)$ of the irradiated SiO/Cr film and a pure Cr film (Fig. 2, curves b and c) confirms the conclusion that surface segregation of Cr occurs. In addition, the metallized parts of the SiO/Cr film can be selectively removed using well-known etchants for chromium.

The action of high-intensity pulsed laser irradiation on an absorbing thin-film medium is an effective means of stimulating various chemical processes such as structural conversions, phase transitions, surface chemical reactions, and diffusion processes. The nature of a particular process is determined to a considerable extent by the structural characteristics of the absorbing layer. For instance, irradiation of homogeneous SiO/Cr layers by laser pulses of below-threshold intensity causes thermally stimulated formation of chromium silicides.[5] In contrast, it has been shown that for our inhomogeneous SiO/Cr layers similar laser treatment causes the phase separation of metallic chromium at the free surface of the film. In our view, this characteristic is attributable to the gradient of the component composition of the inhomogeneous layer, which may give rise to elastic stresses in the layer. We also know that pulsed laser heating of an absorbing layer is accompanied by the creation of large thermoelastic stress gradients.[6] In our case, the irradiation-induced thermoelastic stresses increase the stresses already present in the layer. After the total field of elastic stresses has reached a certain critical value, which is determined by the radiation power density ($\sim 4 \times 10^6$ W/cm$^2$), an avalanche-like mass transfer of chromium is observed toward the free surface of the layer. This assumption is confirmed by the observed release of chromium at the surfaces of these layers under the action of local mechanical loading, for example under the pressure from the tip of a metal needle. A similar effect is not observed in homogeneous SiO–Cr layers.

To conclude, when inhomogeneous SiO/Cr layers whose composition varies smoothly with depth, are exposed to single 337.1 nm nanosecond laser pulses, phase transitions occur and these are accompanied by the release of the metallic component (Cr) at the free surface of the film. A similar effect occurs when local mechanical loads are applied. The observed surface segregation of chromium may be caused by the action of elastic stress fields whose magnitude increases appreciably under the action of pulsed laser radiation, local mechanical loading, and so on. Further studies of their thermophysical, electrophysical, and optical characteristics are required before the observed mass transfer processes in these layers can be modeled. The observed laser-radiation-stimulated phase separation of chromium in inhomogeneous SiO/Cr layers may have practical applications, for example for the optical recording of information.

[1] *Physics of Thin Films*, edited by G. Hass, M. Francombe, and R. W. Hoffman (Academic Press, New York, 1975; Mir, Moscow, 1978, 359 pp.).

[2] É. I. Levitina and V. M. Chekmarev, *Vacuum Light-Absorbing Coatings in Optical Instrument Manufacture* [in Russian], State Optical Institute Press, Leningrad (1990), 225 pp.

[3] P. E. Shepelyavyĭ, E. V. Mikhaĭlovskaya, I. Z. Indutnyĭ *et al.*, Opt. Tekhn. No. **2**(6), 16 (1995).

[4] I. I. Popovich, O. V. Luksha, I. M. Migolinets *et al.*, Pis'ma Zh. Tekh. Fiz. **15**(20), 64 (1989) [Sov. Tech. Phys. Lett. **15**, 814 (1989)].

[5] V. I. Smilga, T. D. Fetisova, G. R. Levinson, and I. G. Stoyanova, Izv. Akad. Nauk SSSR, Ser. Fiz. **38**, 2323 (1974).

[6] V. P. Voronkov and G. A. Gurchenok, Fiz. Tekh. Poluprovodn. **24**, 1831 (1990) [Sov. Phys. Semicond. **24**, 1141 (1990)].

Translated by R. M. Durham

# Observation of segregation deposits in iron–nickel–titanium alloy using scanning tunneling microscopy

V. L. Arbuzov, K. V. Shal'nov, S. E. Danilov, A. É. Davletshin, N. L. Pecherkina, and V. V. Sagaradze

*Institute of Metal Physics, Urals Branch of the Russian Academy of Sciences, Ekaterinburg*

Scanning tunneling microscopy and electron microscopy were used to study the aging process of the fcc alloy Fe+36.5%Ni+2.5%Ti under annealing. The possibility of using scanning tunneling microscopy to study new-phase deposits formed during aging is examined. The sizes of the $\gamma'$-phase particles was determined. © *1999 American Institute of Physics.*
[S1063-7850(99)02102-3]

Studies of the degradation characteristics of austenitic stainless steels and alloys are an important topic because the shape and sizes of the incipient new-phase deposits determine many macroscopic characteristics such as the radiation resistance and strength. However, classical methods of examination, i.e., x-ray and electron microscopy, cannot always be used to reliably study the process of formation of a new phase, especially in the initial stages. Thus, scanning electron microscopy (a method of examining the surface structure of samples with nanometer resolution) holds great promise for studying aging processes.

In order to identify the capabilities and characteristics of using scanning tunneling microscopy (STM) to study thermal and radiation-induced structural-phase transitions in metals and alloys, it was necessary to confirm that, in principle, STM could be used since the literature contains no examples of STM being used for this purpose. Scanning tunneling microscopy is usually used in studies of surface physics, nanostructures, and nanotechnology.[1] In our case we needed to monitor the formation of a new phase in the bulk of the material.

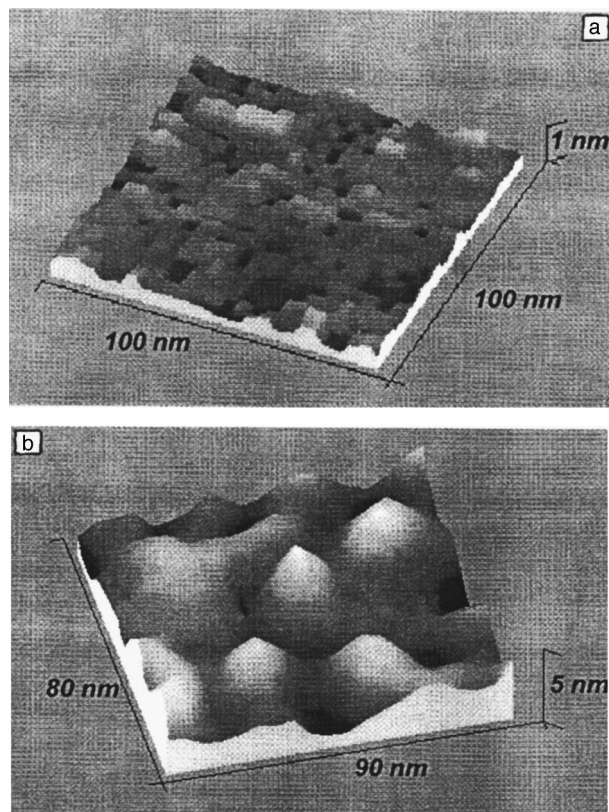The model alloy used for these investigations was the



FIG. 1. Typical STM images obtained at the surface of N36T2 alloy: a — after quenching in water at 1100 °C, b — after annealing at 750 °C for 10 h.
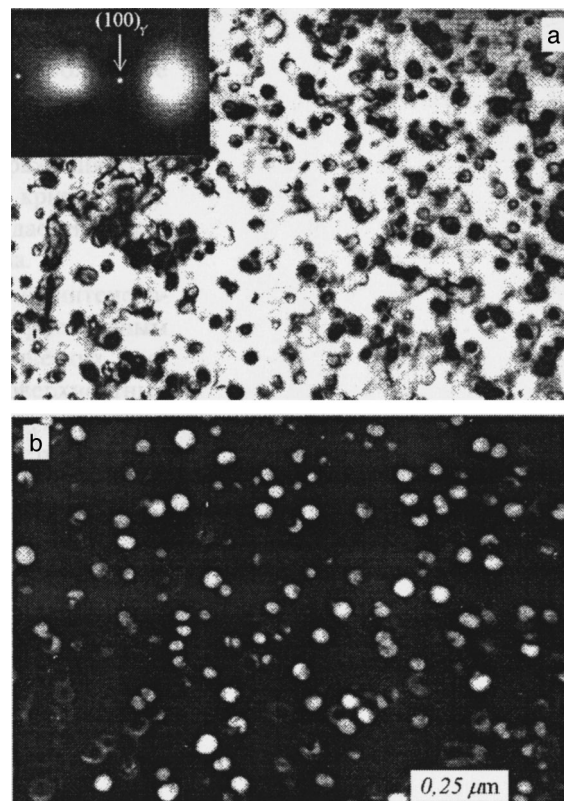


FIG. 2. Light-field (a) and dark-field (b) electron-microscope images of the $\gamma'$ phase in aged N36T2 alloy. The inset to Fig. 2a shows an electron diffraction pattern of N36T2 alloy.

fcc alloy Fe+Ni(36.5 wt.%)+Ti(2.5 wt.%). In the quenched state this alloy is a supersaturated solid solution and, as a result of aging, an ordered $\gamma'$ phase should be formed, similar in composition to $Ni_3Ti$. This phase has a lattice parameter similar to that of the matrix and is coherently bound with the matrix. These factors make it difficult to identify this phase at the initial stages of aging using x-ray and electron microscopic methods. However, after fairly long aging times, when the size of the deposits is 8–20 mm, these $\gamma'$ phase deposits can be identified fairly easily by electron microscopy.[2]

Samples of N36T2 alloy were annealed in a purified helium stream for 30 min at 1100 °C and then quenched in water at a rate of $\sim 500$ K/s to obtain a supersaturated solid solution with a homogeneous titanium distribution. The samples were polished in a reagent containing $H_2SO_4$ $+CrO_3$ to smooth the relief and remove any surface oxides. The surface of the samples was then examined by STM. Figure 1a shows a typical image of the surface after quenching. It can be seen that the surface of the quenched sample is fairly smooth, without any characteristic features.

An electron-microscope examination of samples aged at 750 °C for 10 h showed that fcc $\gamma'$-phase $Ni_3Ti$ deposits formed in N36T3 alloy after aging. These $\gamma'$-phase particles are ordered and give superstructure reflections (Fig. 2a). A dark-field image of the $\gamma'$ particles in the $(100)_{\gamma'}$ superstructure reflex is shown in Fig. 2b. The average size of the $\gamma'$ phase particles determined from measurements using dark-field photographs is 35 nm and their density is 5 $\times 10^{14}$ cm$^{-3}$.

The aged sample was then electrically etched using the same reagent as the quenched one. The depth of etching was $\sim 1$ $\mu$m. We assume that the rates of etching of these new phases and the matrix will differ, which will create a surface relief during etching when these deposits are present in the bulk.

Figure 1b shows an STM image of the surface of an aged sample after electrical etching. This clearly shows spherical irregularities with an average size of $\sim 17-25$ nm. Bearing in mind that these irregularities were not observed on the quenched sample after etching, we can postulate that the spherical irregularities observed on the surface of the aged sample are deposits of a new phase. The deposits are smaller than those obtained by electron microscopy for two reasons: first, the STM examination is made at the surface of the sample and the visible part of the deposit may be smaller than that in the bulk; second, the $\gamma'$ particles may become smaller as a result of the etching. It is also possible that particles smaller than the average may be present in this part of the sample during the STM examination.

Thus, we have shown that: 1) intermetallide aging with the formation of $\gamma'$-phase deposits whose sizes reach 35 nm is observed in the fcc alloy N36T2; 2) STM examinations may be used to investigate deposits of a new phase in the bulk of the material.

[1] V. S. Édel'man, Prib. Tekh. Éksp. No. 1, 24 (1991).
[2] V. M. Alyab'ev, V. G. Volgin, and S. F. Dubinin, Fiz. Metall. Metalloved. No. 8, 142 (1990).

Translated by R. M. Durham

# Dynamics of a map lattice with threshold coupling

A. A. Koronovskiĭ

*"Kolledzh" State Educational-Scientific Center, Saratov State University*
(Submitted April 29, 1998)
Pis'ma Zh. Tekh. Fiz. **25**, 28–34 (February 26, 1999)

An analysis is made of the dynamics of a logistic map lattice with threshold coupling and it is shown that, depending on the values of the control parameters, various types of spatial structures are formed in these lattices. For these structures there is a set of numerical values characterizing the type of structure which depends on the values of the control parameters. It is shown that in the spatially steady-state structures formed in a coupled-map lattice, there are small regions of nonstationary processes in which periodic oscillations occur. © *1999 American Institute of Physics.* [S1063-7850(99)02202-8]

The logistic mapping has been extensively studied and may be described as a standard tool of nonlinear dynamics (see Ref. 1, for example). This standard mapping is used as the basis to construct and study systems of coupled logistic maps,[2,3] as well as one-dimensional chains and two-dimensional lattices of logistic maps with various types of coupling.[4–6] In particular, analyses have been made of two logistic maps with mutual threshold coupling[7] and a chain of logistic maps with unidirectional threshold coupling.[8]

Here an analysis is made of a lattice of logistic maps coupled by means of threshold coupling:

$$u_{ij}^{k+1}=u_{ij}^k\left(a-s\,\mathrm{sgn}\left(\left\{\sum_{l=i-1}^{i+1}\sum_{s=j-1}^{j+1}u_{ls}^k\right\}-u_{ij}^k-u_{\mathrm{th}}\right)-u_{ij}^k\right),\tag{1}$$

where $i$ and $j$ are the discrete spatial coordinates of a lattice element and $k$ is the discrete time. The parameters $a$ and $s$ are assumed to be the same for all the lattice elements. It can be seen from Eq. (1) that an arbitrary lattice element is influenced by elements in the immediate neighborhood of this element. The numerical values of the parameters $a$ and $s$ are selected so that the behavior of this map corresponds to a fixed point on the Lameré diagram if no oscillations occur in the elements adjacent to that being considered, in other words $a+s<3$. The parameter $u_{\mathrm{th}}$ is the threshold above which ($\{\sum_{l=i-1}^{i+1}\sum_{s=j-1}^{j+1}u_{ls}^k\}-u_{ij}^k$), the stable fixed point in the map with the discrete coordinates $i,j$, undergoes an abrupt change. Strictly speaking, this is why this type of coupling has been called "threshold." The term $-u_{ij}^k$ after the signum function is introduced to eliminate the influence of coupling between an element with the discrete coordinates $i,j$ and itself.

Thus, the dynamics of a lattice element with the discrete coordinates $i,j$ is influenced by its neighbors and this element in turn influences them.

Since in the present paper we are considering bounded map lattices, we need to impose constraints on the boundary elements. We shall subsequently assume that for elements with the discrete coordinate $i=0$ the following relation holds:

$$u_{0j}^{k+1}=u_{0j}^k\left(a-s\,\mathrm{sgn}\left(\left\{\sum_{l=0}^{1}\sum_{s=j-1}^{j+1}u_{ls}^k\right\}-u_{0j}^k-u_{\mathrm{th}}\right)-u_{0j}^k\right).\tag{2}$$

Similar relations can also be written for the other boundary elements of a map lattice with the coordinates $j=0$, $i=I_{\mathrm{max}}$, and $j=J_{\mathrm{max}}$. In other words, we can say that a
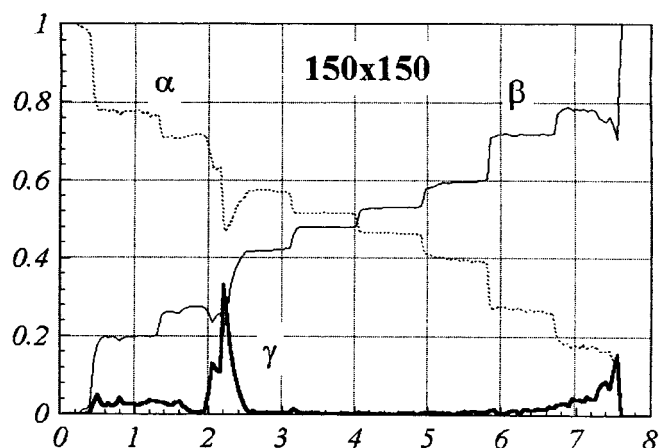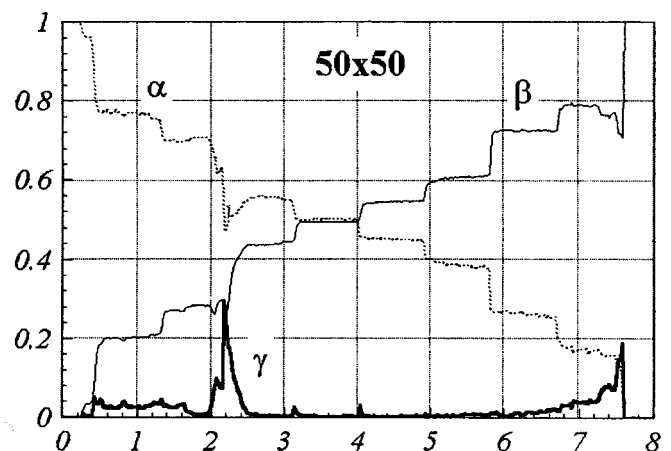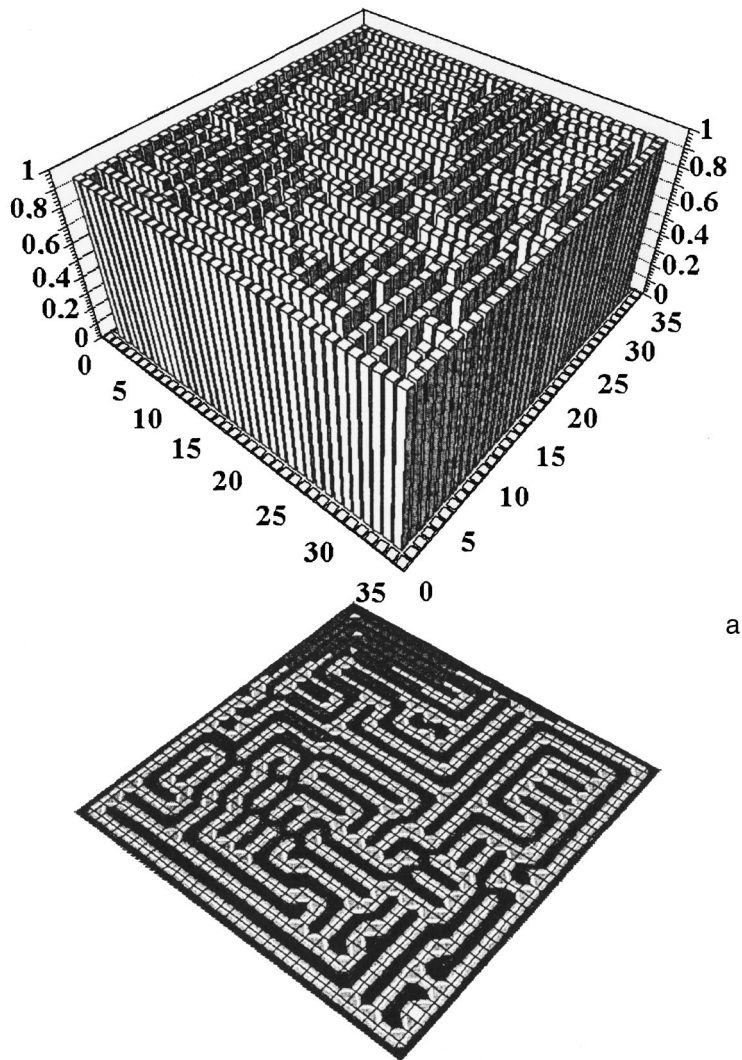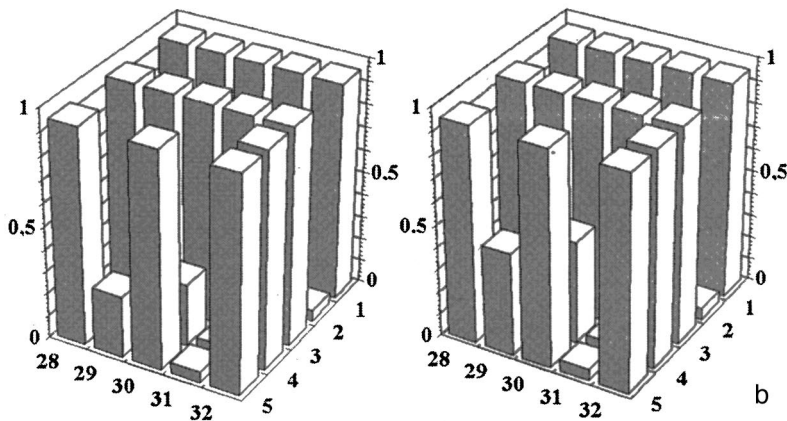


FIG. 1. Dependences of $\alpha_{150\times150}$, $\beta_{150\times150}$, $\gamma_{150\times150}$, and $\alpha_{50\times50}$, $\beta_{50\times50}$, $\gamma_{50\times50}$ on the control parameter $u_{\mathrm{th}}$ ($a=1.5$, $s=0.45$).

FIG. 2. a — structure formed in a $35 \times 35$ logistic map lattice with threshold coupling for values of the control parameters $a = 1.5$, $s = 0.45$ and $u_{th} = 4.4$; b — fragment of the same structure showing oscillatory behavior with an oscillation period of 2.

lattice with free edges is being considered, since the boundary elements of the lattice are influenced only by their immediate neighbors located inside and along the boundaries of the lattice.

The results of numerical experiments show that after a transition process has taken place, an equilibrium state is established in a logistic map lattice with threshold coupling whose form depends on the parameters of the system and the initial conditions. An interesting point is that the established spatially steady-state structures contain ''islands'' of several elements in which oscillations exist. For the same values of the parameters but different initial distributions different structures are established in the lattice map, but nevertheless we can introduce some ''global'' characteristics which will be the same for these structures.

We shall analyze an $m \times n$ lattice with free edges described by relations (1) and (2) with a random initial distribution. Let us assume that $N_+$ is the number of map lattice elements whose value after the completion of a transition process is constant and greater than $U_{th}$ (it can be said that these elements are in an excited state), $N_-$ is the number of map lattice elements with a constant value lower than $u_{th}$ (unexcited state), and $N_0$ is the number of lattice elements in which oscillations occur after a transition process (oscillating state). We then introduce the quantities

$$\alpha_{mn} = \frac{N_+}{m \times n}, \quad \beta_{mn} = \frac{N_-}{m \times n}, \quad \gamma_{mn} = \frac{N_0}{m \times n},$$

which are in fact the relative number of elements in the excited, unexcited, and oscillating states. The results of a numerical investigation of this type of lattice indicate that the external form of the structures formed from different initial distributions is different but the values of $\alpha_{mn}$, $\beta_{mn}$, and $\gamma_{mn}$ for these structures remain almost the same.

Quite understandably, the size of this lattice influences the numerical values of $\alpha_{mn}$, $\beta_{mn}$, and $\gamma_{mn}$: the smaller the lattice, the greater the role played by the edge effects. Thus, it is worth also introducing the parameters $\alpha$, $\beta$, and $\gamma$ for an unbounded lattice of elements: DLB

$$\alpha = \lim_{\substack{m \to \infty \\ n \to \infty}} \alpha_{mn},$$

$$\beta = \lim_{\substack{m \to \infty \\ n \to \infty}} \beta_{mn},$$

$$\gamma = \lim_{\substack{m \to \infty \\ n \to \infty}} \gamma_{mn}.$$

It is quite clear that the larger the $m \times n$ lattice being studied, the closer are the values of $\alpha_{mn}$, $\beta_{mn}$, and $\gamma_{mn}$ to $\alpha$, $\beta$, and $\gamma$. Figure 1 gives the values of $\alpha_{150 \times 150}$, $\beta_{150 \times 150}$, $\gamma_{150 \times 150}$, and $\alpha_{50 \times 50}$, $\beta_{50 \times 50}$, $\gamma_{50 \times 50}$ as a function of the control parameter $u_{th}$. Some characteristic features of the dynamics of a coupled logistic map lattice with threshold coupling can be clearly identified: first, the figure clearly shows the difference in the values of $\alpha_{mn}$, $\beta_{mn}$, and $\gamma_{mn}$ for lattices of different dimensions caused by the influence of edge effects. Second, it can be seen that the range of variation of the control parameter $u_{th}$ is divided into several characteristic sections within which the values of $\alpha_{mn}$, $\beta_{mn}$, and $\gamma_{mn}$ vary little. Finally, it can be seen that the range of variation of the parameter $u_{th}$ has regions within which a large number of ''islands'' of oscillatory motion appear in the lattice of threshold-coupled logistic maps. Figure 2a illustrates the structure formed in the map lattice and Fig. 2b shows the time behavior of an island of oscillatory motion within the spatially uniform structure formed in the lattice.

It is also interesting to determine what happens to the structure established in the lattice after a transition process if the control parameter $u_{th}$ begins to vary slowly. Initially, we can envisage two possible modes of behavior of the steady-state structure: either the steady-state structure will not undergo any changes with varying $u_{th}$ (the stationary regions will remain stationary and oscillations will occur in the islands of oscillatory motion) until $u_{th}$ goes outside the range in which the values of $\alpha_{mn}$, $\beta_{mn}$, and $\gamma_{mn}$ vary weakly; or the steady-state structure will undergo negligible changes as the parameter $u_{th}$ varies, some of the previously stable maps will be converted into islands of oscillations and, conversely, in oscillatory regions the oscillations will cease and stationary states will be established. However, these small changes should not affect the general structure formed in the lattice. When $u_{th}$ goes outside the range of negligible changes in $\alpha_{mn}$, $\beta_{mn}$, and $\gamma_{mn}$, the structure established in the logistic map lattice with threshold coupling should undergo substantial rearrangement.

As a result of these investigations it was established that a second scenario can also occur in a logistic map lattice with threshold coupling as the parameter $u_{th}$ varies: if $u_{th}$ does not go outside a certain range of $\alpha_{mn}$, $\beta_{mn}$, and $\gamma_{mn}$ as it varies, the structure formed in the lattice will undergo negligible changes with varying $u_{th}$ (islands of oscillations will form and disappear, and individual elements may be transferred from excited to unexcited states, and conversely), but when $u_{th}$ goes outside this range, the structure undergoes major rearrangement.

To sum up, an analysis has been made of a logistic map lattice with threshold coupling. It has been established that if the lattice control parameters in these lattices are selected so that in the absence of oscillations in neighboring elements an isolated logistic map exhibits no oscillatory dynamics, spatially steady-state structures appear with islands of oscillations which depend on the control parameters.

[1] A. P. Kuznetsov and S. P. Kuznetsov, Izv. Vyssh. Uchebn. Zaved. Prikl. Nelin. Dinam. **1**, No. 1, 2, 15 (1993).
[2] S. P. Kuznetsov, Izv. Vyssh. Uchebn. Zaved. Radiofiz. **33**, 788 (1990).
[3] S. P. Kuznetsov, Zh. Tekh. Fiz. **55**, 1830 (1985) [Sov. Phys. Tech. Phys. **30**, 1071 (1985)].
[4] S. P. Kuznetsov, Pis'ma Zh. Tekh. Fiz. **9**(2), 94 (1983) [Sov. Tech. Phys. Lett. **9**, 41 (1983)].
[5] A. P. Kuznetsov and S. P. Kuznetsov, Izv. Vyssh. Uchebn. Zaved. Radiofiz. **34**, No. 10, 11, 12 (1991).
[6] A. P. Kuznetsov and S. P. Kuznetsov, Izv. Vyssh. Uchebn. Zaved. Radiofiz. **34**(2), 142 (1991).
[7] A. A. Koronovskiĭ, V. I. Ponomarenko, and D. I. Trubetskov, Izv. Vyssh. Uchebn. Zaved. Prikl. Nelin. Dinam. **5**(2), 63 (1997).
[8] A. A. Koronovskiĭ, Pis'ma Zh. Tekh. Fiz. **23**(6), 61 (1997) [Tech. Phys. Lett. **23**, 236 (1997)].

Translated by by R. M. Durham

# Ferromagnetic circuit breaker

G. A. Shneerson, Yu. N. Bocharov, I. P. Efimov, and S. I. Krivosheev

*St. Petersburg State Technical University*

Current can be transferred to the load of an inductive energy storage device by rapidly increasing the inductance of a circuit element connected in parallel with the load. The present paper suggests using a coil with a ferromagnetic core for this purpose. In addition to the principal (toroidal) field, an orthogonal (poloidal) control field is generated in the core. The results presented here demonstrate that under certain conditions, the magnetization and therefore the inductance can be changed abruptly by this orthogonal control field. It is also shown that the switching process can be controlled by fairly small currents. Under favorable geometric conditions, the inductance can vary by a factor between 3 and 10. The proposed system is suitable for multiple use, since it contains no elements that are damaged during the switching process, as is the case with exploding conductors, and is effective for a low-inductance load.   © *1999 American Institute of Physics.* [S1063-7850(99)02302-2]

1. We shall first discuss the operating principle of a ferromagnetic circuit breaker with transverse magnetization. Current is transferred rapidly to inductive and inductive-capacitive energy storage devices by using systems in which the intermediate impedance of the circuit element increases abruptly. This process can be accomplished by various methods, including a jump in the inductance of the circuit (Fig. 1) from the initial value $L_1'$ to a final level $L_1''$. In this case, the current in the load and the current $i_1$ will be given by[1]

$$i_2'' = i_0' \frac{K-1}{L_2/L_1' + K(1+L_2/L_0)},$$

$$i_1'' = i_0' \frac{1+L_2/L_1'+L_2/L_0}{L_2/L_1' + K(1+L_2/L_0)}, \tag{1}$$

where $i_0'$ is the initial value of the current $i_0$, $i_2''$ is the current in the inductive load, and $K=L_1''/L_1'$ is the change in inductance.

A megampere current pulse with a rise time of the order of $10^{-6}$ s or less is required to generate ultrastrong magnetic fields in single-turn low-inductance solenoids. In this case, an inductive-capacitive storage system can be used to shorten the pulse rise time.[2] In these experiments the condition $L_2 \ll L_0$ is usually satisfied, where $L_0$ is the inductance of the energy source.

Here we consider the possibility of using a jump in the magnetization of the coil core $L_1$ as a result of some external influence for switching purposes. In the initial state, the core should be deeply saturated and then, at the required time, the core material should be transferred to an unsaturated state, accompanied by a sharp rise in the inductance to $L_1''$ and transfer of current to the load $L_2$. The process should also be controlled so that the inductance jump and when it occurs are determined by the external influence and not by the current in the storage circuit. Here we suggest using an orthogonal field system for this purpose.[3]

In the proposed device, the inductance $L_1$ is a coil with a toroidal core with the current $i_1$ flowing through its winding, generating a toroidal field with the induction $B_\theta$ (Fig. 1). A circuit with the current $i_\theta$ is located on the axis of the core. The induction of the toroidal field generated by the current $i_1$ is orthogonal to the induction of the poloidal field $B_\varphi$ generated by the current $i_\theta$. The inductance $L_1$ can be varied widely by means of the control current $i_\theta$, as is shown, for example, when the core material is isotropic and the dependence of the induction on the magnetic field strength has the form $\bar{B}=\mu(H)\bar{H}$. In this formula the magnetic permeability depends on the strength modulus $H=(H_\varphi^2+H_\theta^2)^{1/2}$. Let us assume that in the initial state of the system we have $H_\varphi \gg H_s$ and $H_\theta \gg H_s$ (point *1* on the curve $B(H)$ plotted in Fig. 1). Here $H_s$ is the threshold strength, corresponding to the point of intersection of the two sections of the broken curve which approximates the magnetization curve. In the initial state the core saturates rapidly as a result of the action of the poloidal field $H_\varphi$. When the current $i_\theta$ is switched off, the field $H_\varphi$ becomes zero and the system is at point *2*. The inductance $L_1$ increases sharply and the currents $i_0$, $i_1$, and $i_2$ in the circuit elements of the inductive storage device vary accordingly. Note that instead of switching off the current $i_\theta$, a current $-i_\theta$ could be switched on in the same circuit or in a nearby circuit inside the core.

We now give some estimates of the parameters of a ferromagnetic circuit breaker, we consider its possible application for switching in low-inductance circuits, and also give some results of calculations.

2. We now present some approximate characteristics of a ferromagnetic circuit breaker. For an approximate description of the magnetic circuit of a circuit breaker the magnetization curve can be replaced by the broken line (Fig. 1):

$$B(H)=\begin{cases} \mu H, & B \leq B_S, \\ \mu_{\text{eff}} H, & B \geq B_S, \end{cases} \tag{2}$$
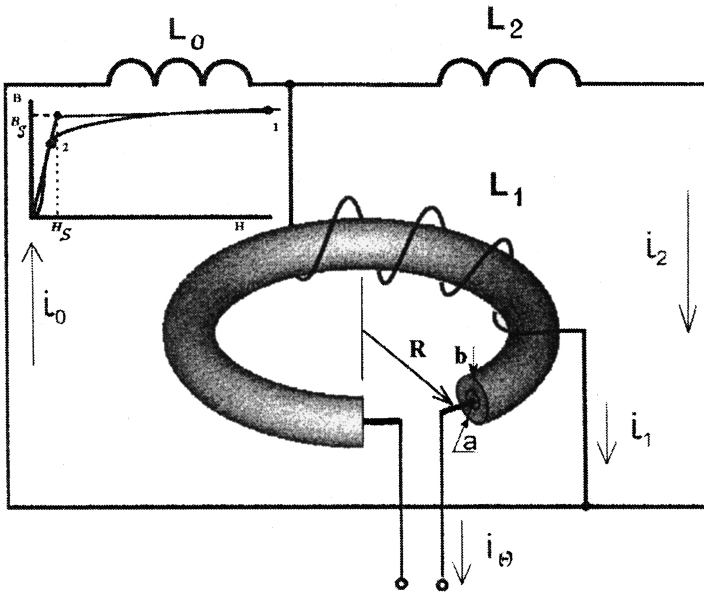
where

FIG. 1. Circuit for transferring current to an inductive load as a result of a change in the inductance $L_1$.

$$\mu_{\text{eff}} = \frac{B_S + (H - H_S)\mu_0}{H} = \mu_0 \left[ 1 + \frac{B_S}{\mu_0 H} \left( 1 - \frac{\mu_0}{\mu} \right) \right].$$

We take as the calculation model a system in the form of a hollow toroid in which the condition $b < a \ll R$ is satisfied (Fig. 1). In the saturation state we have $H \approx H_\varphi = i_\theta / 2\pi a$. Under the conditions $\mu \gg \mu_0$ and $H_\varphi \gg H_\theta$ we have in the initial state

$$\mu_{\text{eff}} = \mu'_{\text{eff}} \approx \mu_0 \left( 1 + \frac{B_S}{\mu_0 H_\varphi} \right) = \mu_0 \left( 1 + \frac{l_\varphi B_S}{\mu_0 i_\theta} \right). \tag{3}$$

Here $l_\varphi = 2\pi a$ is the length of a poloidal field line and $H_\varphi$ is its strength. For the following estimates we take $B_S = 1.5\,\text{T}$, which corresponds to magnetic materials such as permalloy, amorphous iron, etc., used in pulse transformers and magnetic flux compression devices.

If the currents $i_1$ and $i_\theta$ are the same, the ratio is $H_\varphi / H_\theta \approx l_\theta / a$. If $l_\theta / a \gg 1$, the condition $H_\varphi / H_\theta \gg 1$ can be satisfied if the control current $i_\theta$ is smaller than $i_1$. Thus, in a system with orthogonal fields the switching process can be controlled externally using a relatively weak current.

If the condition $w_1 i''_1 < B_S l_\theta / \mu = i_{1s}$ is satisfied, the core will not be saturated after switching ($w_1$ is the number of turns). The current $i''_1$ can be obtained by using formula (1), which can be conveniently expressed as follows:

$$i''_1 = i'_0 \frac{\alpha}{K + \beta} < i_{1s} / w_1, \tag{4}$$

where $\alpha = (1 + L_2/L'_1 + L_2/L_0)/(1 + L_2/L_0)$ and $\beta = (L_2/L'_1)/(1 + L_2/L_0)$ are dimensionless numbers determined by the inductance ratios. In the particular case $L_2/L_0 \ll 1$, we have $\alpha = 1 + L_2/L'_1$ and $\beta = L_2/L'_1$. Formula (4) yields a constraint on the switchable current

$$w_1 i'_0 \leqslant \frac{i_{1s}}{\alpha} (K + \beta). \tag{5}$$

The magnetization current is relatively weak. Nevertheless, condition (5) can even be satisfied for a large switchable current if the ratio $\mu / \mu'_{\text{eff}} = K$ is fairly large. Using formula (2), we obtain general expressions for $K$, the permissible switchable current, and the current in the load:

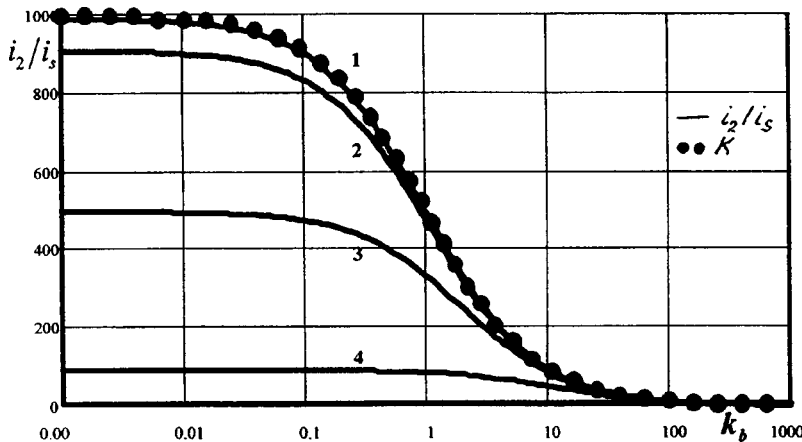$$K = \frac{L''_1}{L'_1} = \frac{\mu_0 / \mu}{1 + (1 - \mu_0 / \mu) p}, \tag{6}$$



FIG. 2. Dependence of $i_2/i_s$ and $K$ on the parameter $k_b = B_S/(\mu_0 H_\varphi)$. For $L_2/L_1^0$: *1* — 0.01, *2* — 0.1, *3* — 1, and *4* — 10.
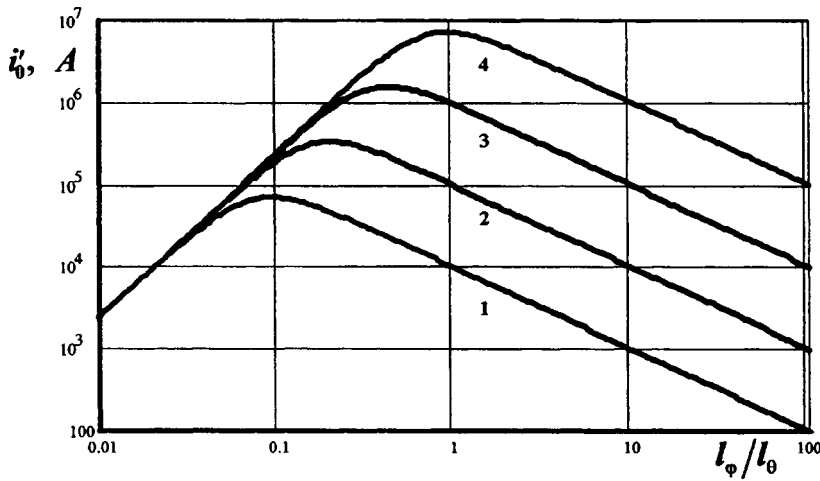
FIG. 3. Dependence of the permissible switching current $i_0'$ on the ratio $l_\varphi/l_\theta$. For $i_\theta$: *1* — $10^4$ A, *2* — $10^5$ A, *3* — $10^6$ A, and *4* — $10^7$ A.

$$i_0' = \frac{l_\theta B_S}{\mu}\left(1 + \frac{\mu}{\mu_0}\left[1 + p + \frac{L_2 l_\theta}{\mu_0 S[1+p]} + \frac{L_2 l_\theta}{\mu_0 S}\frac{p}{p+1}\right]^{-1}\right), \tag{7}$$

$$i_2'' = \frac{l_\theta B_S}{\mu_0}\left[1 + p + \frac{L_2 l_\theta}{\mu_0 S[1+p]} + \frac{L_2 l_\theta}{\mu_0 S}\frac{p}{1+p}\right]^{-1}. \tag{8}$$

Curves illustrating these dependences as a function of the dimensionless parameter $p = B_S/(\mu_0 H_\varphi)$ are plotted in Fig. 2.

3. We shall now consider the weak saturation regime, which corresponds to the right-hand side of the curves plotted in Fig. 2, where the condition $B_S/(\mu_0 H_\varphi) > 1$ is satisfied. Subject to this condition and in accordance with condition (5), the following estimates are valid for the currents and $K$:

$$K \approx H_\varphi/H_S, \quad i_0' \approx \frac{i_\theta l_\theta}{l_\varphi(1 + L_2 l_\theta i_\theta/(SB_S l_\varphi))},$$

$$i_2'' \approx \frac{l_\theta H_\varphi}{1 + L_2 l_\theta H_\varphi/(B_S S)}. \tag{9}$$

The formulas (9) can be used to optimize the parameters of an inductive storage device with a ferromagnetic switch. The optimization problem may be posed as the choice of the parameter $l_\varphi$, the length of the poloidal field line for which the maximum switchable current $i_0'$ can be achieved in a solenoid of fixed length for a given control current $i_\theta$ (Fig. 3). The results show that for a continuous solenoid of around 1 m length, switchable currents of the order of $10^5$ A can be achieved while the amplitude of the control currents can be several times smaller. In order to achieve currents close to $10^6$ A, it is necessary to increase the core length, which (for a constant control current $i_\theta$) increases proportionately as $(i_0')^2$. It should be noted that in this case, although the ratio $K$ is lower than the limiting value of $\mu/\mu_0$, it is still high (of order tens or higher).

4. We shall now consider strong saturation, which corresponds to the condition $B_S/\mu_0 H_\varphi \ll 1$ (left-hand side of Fig. 2). Under the conditions $\mu/\mu_0 \gg 1$, $K \gg 1$ the currents and $K$ have values of

$$K \approx \frac{\mu}{\mu_0(1 + B_S/\mu_0 H_\varphi)},$$

$$i_2'' \approx \frac{B_S l_\theta}{\mu_0(1 + L_2/L_1')(1 + B_S/\mu_0 H_\varphi)},$$

$$i_0 \approx \frac{B_S l_\theta}{\mu} + \frac{B_S l_\theta}{\mu_0[1 + (1 + B_S/\mu_0 H_\varphi)L_2/L_1']}. \tag{10}$$

Strong saturation may be used to achieve megampere currents in a low-inductance load. In this case the length $l_\theta$ should be fairly large and the solenoid cross section should be selected so that the ratio $L_2/L_1'$ is not large. If the length and the solenoid cross section are fairly large and the load inductance is low, the ferromagnetic circuit breaker can transfer a megampere current to the load of the inductive storage device in a controlled fashion. For example, if $B_S/\mu_0 H_\varphi = 1$, $\mu_{eff}' = 2\mu_0$ and $B_S = 1.26$ T is assumed, then for $S = 10^{-2}$ m$^2$ and $l_\theta = 5$ m, and inductances $L_2$ of 5 and 1 nH we obtain 1.25 and 2.08 MA, respectively.

5. The following conclusions can be drawn:

a. A controlled change in the inductance in a system with orthogonal fields can be used to transfer current to the load of an inductive storage device. In this case, the controlled inductance is an analog of a circuit breaker.

b. A ferromagnetic circuit breaker can switch megampere currents in systems with a low-inductance load (on the order of $10^{-9}$ H).

c. The circuit breaker parameters can be optimized when the core material is initially weakly saturated. In this regime the circuit breaker is best used to switch currents of $10^4$–$10^5$ A.

[1] G. A. Shneerson, *Field and Transients in Superhigh Pulse Current Devices* (Nova Science Publishers, New York, 1997).
[2] I. A. Burtsev, N. V. Kalinin, and A. V. Luchinskiĭ, *Electrical Explosion of Conductors* [in Russian], Énergoatomizdat, Moscow (1990), 289 pp.
[3] L. I. Dorozhko and M. S. Libkind, *Reactors with Transverse Magnetization* [in Russian], Énergiya, Moscow (1977).

Translated by R. M. Durham

# Nonlinear anomalies of conducting media with conical microconstrictions

Ch. S. Kim and A. M. Satanin

*N. I. Lobachevskiĭ State University, Nizhniĭ Novgorod; Department of Physics, Chonnam National
University, Kwangju, Korea*

An investigation is made of the divergence of the higher moments of the field in conducting
structures with conical singular regions. Calculations are made of the critical values of the
parameters which determine the nonlinear anomalies of a medium. © *1999 American
Institute of Physics.* [S1063-7850(99)02402-7]

The effective nonlinear characteristics of inhomogeneous media are determined by the local values of the material parameters and by the microgeometry of the components.[1] Geometric effects that enhance the nonlinearity of a medium have been studied in two-dimensional fractal media[2,3] and periodic lattices.[4,5] Here we shall show that similar anomalies also occur in three-dimensional media. A medium with conical microconstrictions is taken as an exactly soluble model. Regions of this type may be formed, for example, in periodically packed cubes whose conductivities $\sigma_1$ and $\sigma_2$ differ very significantly. We assume that in the first packing layer the cubes form a ''checkerboard'' lattice and in the next layer, cubes of conductivity $\sigma_2$ are positioned above cubes of conductivity $\sigma_1$, and so on. In other words, the two types of cubes are packed in a lattice with a sodium chloride structure.

In this case, the regions of contact between cubes of similar conductivity $\sigma_1$ are pyramids whose apices are in contact and are surrounded by a medium of conductivity $\sigma_2$. Since an anomaly is caused by a concentration of current near the apices, the nature of the divergence may be demonstrated for simpler regions of contact. Since we are interested in whether the type of anomaly changes qualitatively on transition from the two-dimensional system considered previously[4,5] to a three-dimensional one and we require an exact solution, we replace the pyramidal regions of contact with conical ones. Note that the problem of two contiguous cones is also of independent interest. First, these structures may be produced by microtechnological methods and second, this generalizes the well-known problem of conical defects (depressions) in a metal surface.[6,7] We shall present results of an exact solution of this problem.

We shall study the flow of current along the axis of the structure shown in Fig. 1. As in the well-known problem of a tip,[8] we are interested in the behavior of the solution near a singularity. We assume that the bases of highly conducting cones are connected to Ohmic contacts at the characteristic distance $L$ from the apices of the cones. In order to find the effective linear conductivity of the structure, we need to solve the equations for the current $\mathbf{j}$ and the field $\mathbf{e}$:

$$\mathbf{j} = \sigma\mathbf{e},$$

$$\mathrm{div}\,\mathbf{j} = 0, \quad \mathrm{curl}\,\mathbf{e} = 0 \tag{1}$$

with the boundary conditions

$$\sigma_1(\mathbf{e}\cdot\mathbf{n})_1 = \sigma_2(\mathbf{e}\cdot\mathbf{n})_2, \quad (\mathbf{e}\cdot\boldsymbol{\tau})_1 = (\mathbf{e}\cdot\boldsymbol{\tau})_2, \tag{2}$$

where $\mathbf{n}$ and $\boldsymbol{\tau}$ are the unit normal and tangential vectors to the phase interface. The effective linear conductivity can be determined from the condition for energy dissipation

$$\langle\sigma\mathbf{e}^2\rangle = \sigma_e\langle\mathbf{e}\rangle^2, \tag{3}$$

where the notation $\langle(\ldots)\rangle = \int(\ldots)dV/V$ is used for averaging over the volume $V$. We then utilize the fact that for a weakly nonlinear medium with local coupling $\mathbf{j} = \sigma\mathbf{e} = -\chi\mathbf{e}^2\mathbf{e}$ the effective nonlinear conductivity $\chi_e$ is determined by the fourth-order correlation function of the field in a linear medium (this is demonstrated in Refs. 9 and 10)

$$\chi_e = \frac{\langle\chi\mathbf{e}^4\rangle}{\langle\mathbf{e}\rangle^4}. \tag{4}$$

It follows from Eq. (3) that the effective linear conductivity is determined by the quadratic moment of the field; the effective nonlinear conductivity is expressed in terms of the fourth moment of the field (4). We are also interested in higher moments of the field $\langle\mathbf{e}^{2n}\rangle$. According to Dudson *et al.*,[11] the amplitudes of the harmonics excited in a medium by an alternating field are given by

$$B_{3(n-1)} \sim \langle\mathbf{e}^{2n}\rangle, \quad n = 2,3,\ldots, \tag{5}$$

where the field is also obtained from the linear equations (1). The aim of the present paper is to demonstrate the divergence of the higher moments of the field for a finite (critical) value of the system parameters, the conductivity ratio $h = \sigma_2/\sigma_1$ or the cone expansion angle $\vartheta_0$.

We shall seek a solution of the equations (1) in the form

$$\mathbf{j} = -\sigma\nabla\varphi, \tag{6}$$

where the potential is $\varphi = r^\lambda f(\vartheta)$ and the function $f(\varphi)$ is determined from

$$\frac{1}{\sin\vartheta}\frac{\partial}{\partial\vartheta}\sin\vartheta\frac{\partial}{\partial\vartheta}f + \lambda(\lambda+1)f = 0. \tag{7}$$

The solution of Eq. (7) for $\vartheta < \vartheta_0$ should be taken in the form
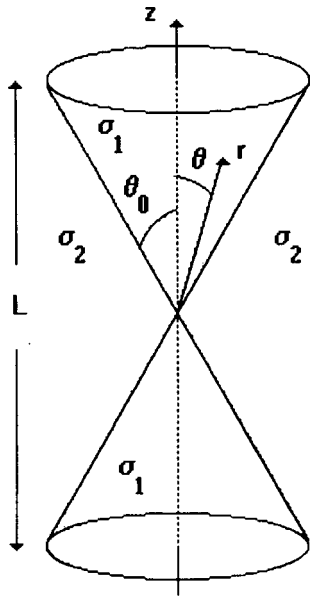
$$f_1 = AP_\lambda(\cos\vartheta), \tag{8}$$

FIG. 1. Schematic of conical regions (linear conductivity $\sigma_1$) immersed in a medium of (poor conductivity $\sigma_2$.)



FIG. 2. Critical structure parameter $h_c$ as a function of the cone expansion angle $\vartheta_0$ for various moments: the dotted curve gives the dependence for the fourth moment (nonlinear conductivity); the dashed and solid curves give those for $n=3$ and $n=4$, respectively.

where $P_x(x)$ is a Legendre function. For the angles $\vartheta_0 < \vartheta < \pi/2$ the solution has the form

$$f_2 = B\left[\frac{1}{2}(1-\cos \pi\lambda)P_\lambda(\cos \vartheta) + \frac{\sin \pi\lambda}{\pi}Q_\lambda(\cos \vartheta)\right],$$
(9)

where $Q_\lambda(x)$ is a Legendre function of the second kind. The functions $f_1$ and $f_2$ at the surface of the cone satisfy the boundary conditions

$$f(\vartheta_0)_1 = f(\vartheta_0)_2, \quad f'(\vartheta_0)_1 = hf'(\vartheta_0)_2,$$
(10)

where $f' = \partial f/\partial \vartheta$. Note that a solution in the range of angles ($\vartheta > \pi/2$) may obtained from Eqs. (8) and (9) by continuation, keeping the result odd in the angle (because of the boundary conditions for the external field).

Substituting Eqs. (8) and (9) into the boundary conditions (10), we can easily find that a general solution is obtained if the following relation is satisfied

$$hP_\lambda(x)\left[\frac{1}{2}(1-\cos \pi\lambda)P_{\lambda+1}(x)\right.$$

$$\left. + \frac{\sin \pi\lambda}{\pi}Q_{\lambda+1}(x) - xF_\lambda(x)\right]$$

$$= F_\lambda(x)[P_{\lambda+1}(x) - xP_\lambda(x)],$$
(11)

where $x = \cos \vartheta_0$, and $F_\lambda(x) = 1/2(1-\cos \pi\lambda)P_\lambda(x) + (\sin \pi\lambda/\pi)Q_\lambda(x)$. Equation (11) can be used to determine the dependence of the parameter $\lambda$ on $h$ and $\vartheta$.

Substituting this solution for the field into Eq. (5), we can calculate the contribution to the correlation function caused by the current singularities in the conical region

$$\langle \mathbf{e}^{2n}\rangle = \frac{\text{const}}{V}\int_0^L drr^2 r^{2n(\lambda-1)}\int_0^\pi d\vartheta \sin \vartheta[(f')^2 + \lambda^2 f^2].$$
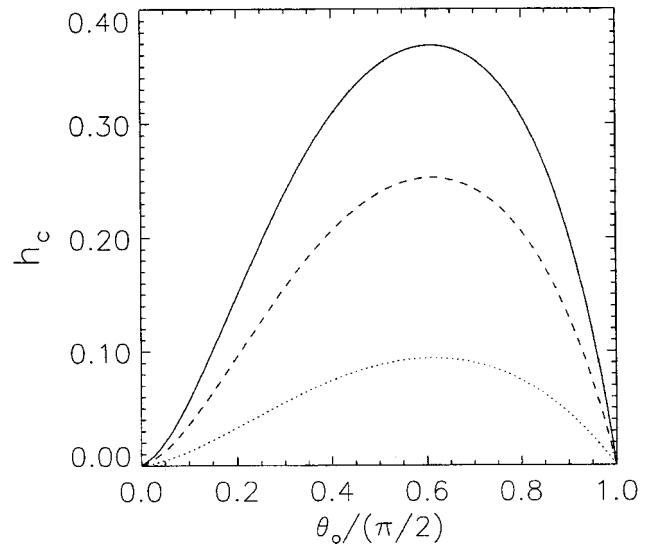(12)

It follows from Eq. (12) that the integral diverges for $\lambda_c = 1 - 3/2n$. Knowing $\lambda_c$, we use Eq. (11) to find the critical value of the parameter $h_c$ as a function of the angle $\vartheta_0$. Figure 2 gives the dependence of $h_c$ on $\vartheta_{0c}$ obtained by solving Eq. (11) numerically for various orders $n$ of harmonics. The maximum critical values of the parameters ($h_c$, $\vartheta_{0e}$) depend on $n$. We shall give the value for several lower moments: for $n=2$ we obtain ($h_c = 0.094$, $\nu_{0c} = 55.50$); for $n=3$ we have ($h_c = 0.253$, $\vartheta_{0c} = 55.30$), and for $n=4$ we have ($h_c = 0.369$, $\vartheta_{0c} = 55.18$). The critical values of the parameters ($h_c$, $\vartheta_{0c}$) in the three-dimensional case differ substantially from the two-dimensional case (the problem of sectors is discussed by Satanin et al.[5]). For example, the critical angle (because of the dual symmetry) in a two-dimensional system is the same for all moments and is equal to $\pi/2$, whereas in a three-dimensional system it depends on the orders of the harmonics.

The prediction of anomalies and calculations of the critical values of the parameters of conical singularities constitute the main result of the present study. Clearly, as a result of geometric factors or thermal effects, the growth of harmonics stabilizes in a real system. We have not discussed the mechanisms for the elimination of anomalies since this will be considered in a separate study.

In order to observe anomalies it is convenient to measure the dependence of the harmonic amplitudes on the microparameters of the system. Existing micro- and nanotechnological methods can be used to produce media with a particular microgeometry. A random medium with conical singularities may be obtained by specially forming the microparticles.[12] A model system can also be used to exhibit anomalies. For example, to obtain a medium with variable $h$ it is convenient to use an electrolyte in which a conical electrode positioned above a metal surface is immersed.

[1] *Proceedings of the Fourth International Conference on Electrical Transport and Optical Properties of Inhomogeneous Media*, Physica A **241**, No. 1–2 (1997).

[2] A. M. Satanin, S. V. Khor'kov, and A. Yu. Ugol'nikov, JETP Lett. **62**, 322 (1995).

[3] A. M. Satanin, Pis'ma Zh. Tekh. Fiz. **21**(16), 44 (1995) [Tech. Phys. Lett. **21**, 652 (1995)].

[4] A. M. Satanin, V. V. Skuzovatkin, and S. V. Khor'kov, JETP Lett. **64**, 538 (1996).

[5] A. M. Satanin, V. V. Skuzovatkin, and S. V. Khor'kov, Zh. Éksp. Teor. Fiz. **112**, 643 (1997) [JETP **85**, 351 (1997)].

[6] R. N. Hall, J. Appl. Phys. **20**, 925 (1949).

[7] J. D. Jackson, *Classical Electrodynamics*, 2nd ed. (Wiley, New York, 1975) [Russ. transl. of 1st ed., IL, Moscow, 1965].

[8] L. D. Landau and E. M. Lifshits, *Electrodynamics of Continuous Media*, transl. of 1st Russ. ed. (Pergamon Press, Oxford, 1960) [Russ. original, later ed., Nauka, Moscow, 1982].

[9] A. Aharony, Phys. Rev. Lett. **58**, 2726 (1987).

[10] D. Stroud and P. M. Hui, Phys. Rev. B **37**, 8719 (1988).

[11] M. A. Dubson, Y. C. Hui, M. B. Weissman, and J. C. Garland, Phys. Rev. B **39**, 6807 (1989).

[12] J. Wu and D. S. McLachlan, Physica A **241**, 360 (1997).

Translated by R. M. Durham

# Solitons of a surface magnetostatic spin wave in a ferrite–insulator–metal structure

A. S. Kindyak

*Minsk Research Institute of Radio Materials, Minsk*
(Submitted April 30, 1998)
Pis'ma Zh. Tekh. Fiz. **25**, 48–54 (February 26, 1999)

The nonlinear Schrödinger equation is analyzed in order to theoretically investigate nonlinear
surface magnetostatic spin waves in a planar ferrite–insulator–metal structure. It is shown
that for specific distances between the metal screen and the ferromagnetic film, pulses of surface
magnetostatic spin waves may propagate as envelope solitons. © *1999 American Institute
of Physics.* [S1063-7850(99)02502-1]

Yttrium iron garnet films in an external magnetic field are the most suitable material for studying the nonlinear properties of surface magnetostatic spin waves. Recently, many experiments have been carried out aimed directly at observing magnetostatic spin wave (MSW) solitons.[1–5] These studies confirmed the results of the first theoretical investigations of the MSW instability in thin ferromagnetic films and thus the possible propagation of MSWs in the form of envelope solitons. The basic principles of the theory of MSW propagation as solitons were put forward by Zvezdin and Popkov.[6] The method of analyzing MSWs used in Ref. 6 and known in the literature as the ''envelope'' method,[7] was developed subsequently and investigated in detail for surface MSWs in Refs. 8–12. One of the results obtained by Karpman[7] and then confirmed experimentally and theoretically in later studies, was the conclusion that a surface mag-netostatic spin wave is stable with respect to longitudinal perturbations, i.e., it is impossible for envelope solitons of surface MSWs to exist.

Theoretical studies of surface MSW instability are based on analyzing solutions of the nonlinear Schrödinger equation in which the coefficients are determined using the MSW dispersion relations:[5–12]

$$i\left[\frac{dA}{dt} + v_g \frac{dA}{dy}\right] + \frac{1}{2}\beta_2 \frac{d^2A}{dy^2} - \gamma|A^2|A = 0. \tag{1}$$

Here $v_g = d\omega/dk$ is the MSW group velocity, $\beta_2 = d^2\omega/dk^2$ is the group velocity dispersion, and $\gamma = (d\omega/d|A|^2)_{|A|=0}$ is the nonlinear coefficient, where $A$ is the dimensionless amplitude of a MSW pulse and $\omega$ and $k$ are its frequency and wave vector, respectively. Note that $v_g$
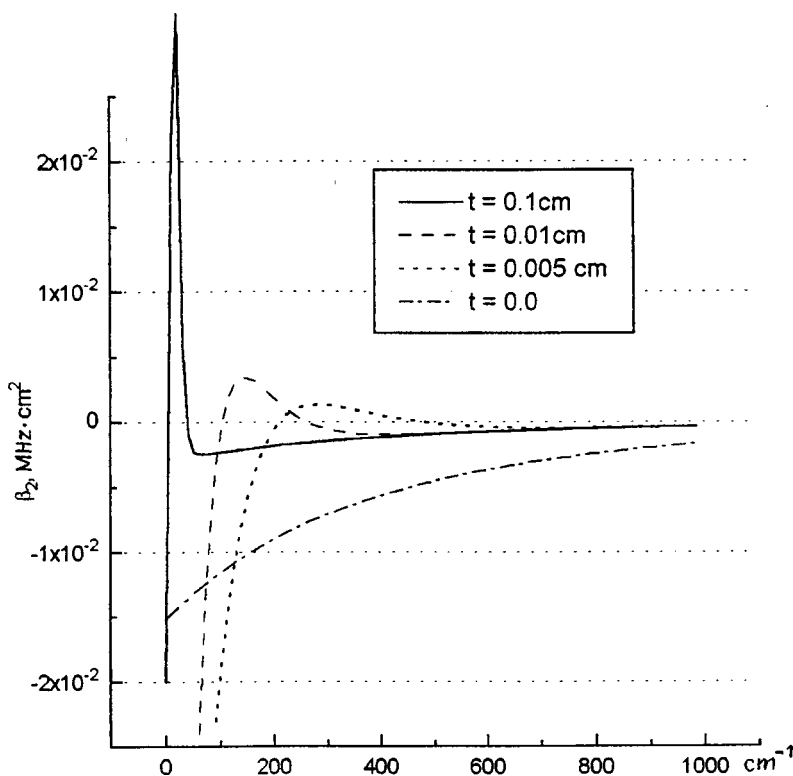


FIG. 1. Dispersion of surface MSW group velocity as a function of the wave vector for various distances between the metal screen and the ferromagnetic film.
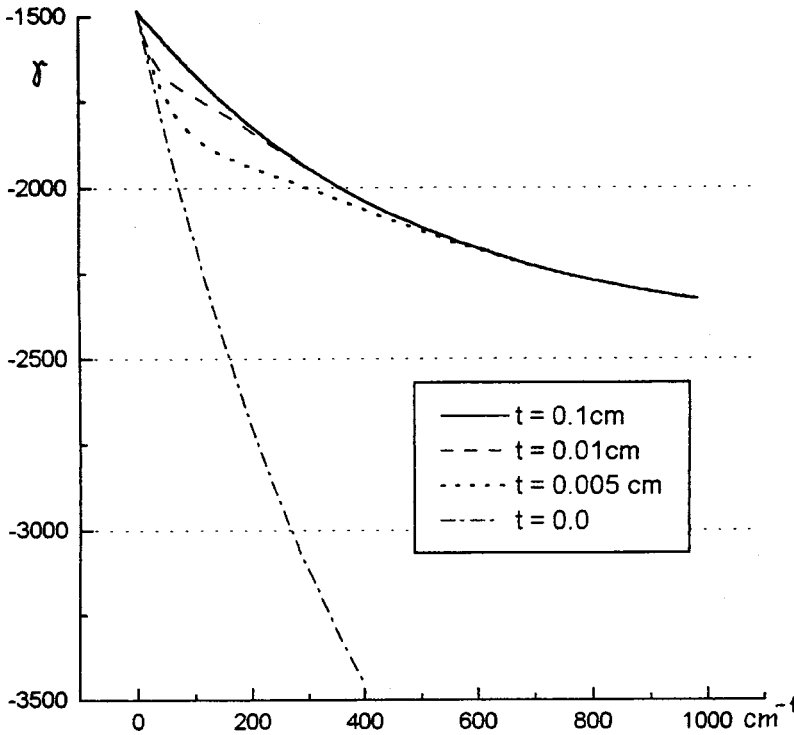
FIG. 2. Coefficient of nonlinearity of a surface MSW as a function of the wave vector for various distances between the metal screen and the ferromagnetic film.

and $\beta_2$ are determined using a linear dispersion equation and the nonlinear coefficient is obtained using the nonlinear MSW dispersion relation. The condition for the onset of MSW instability known as the Lighthill condition,[7] has the form

$$\beta_2 \gamma < 0. \tag{2}$$

It can be seen from Eqs. (1) and (2) that the onset of MSW instability is determined by its dispersion law. Thus, by varying the MSW dispersion law, we can vary the conditions for the onset of MSW instability relative to longitudinal perturbations and thereby control the region of existence of MSW solitons.

It is known[13,14] that the existence of metal screens some distance from a ferromagnetic film substantially changes the surface MSW dispersion law. Thus, from the scientific and practical point of view, it is interesting to study the influence of a metal screen on the conditions for the onset of longitudinal instability and soliton formation for a surface MSW propagating in a planar ferrite–insulator–metal structure.

Let us consider a surface MSW propagating in a planar structure consisting of an yttrium iron garnet film of thickness $d$, an insulator of thickness $t$, and a metal screen. A surface magnetostatic wave propagates along the $Y$ axis and an external magnetic field lies in the plane of the structure and is directed along the $Z$ axis. The dispersion equation for the surface MSW then has the form[15]

$$e^{-2kd} = \frac{(\mu - \mu_a + 1)[\mu + \mu_a + \tanh(kt)]}{(\mu + \mu_a - 1)[\mu - \mu_a - \tanh(kt)]}. \tag{3}$$

Here $\mu$ and $\mu_a$ are the diagonal and off-diagonal elements of the magnetic permeability tensor of the ferromagnet, and $k$ and $\omega$ are the carrier frequency of the surface MSW.

Rewriting Eq. (3) in the form

$$\omega^2 - \omega_h^2 - \omega_h \omega_m - \frac{\omega_m^2}{4}(1 - \beta)$$

$$= \alpha(1 - \beta)\left[(\omega + \omega_h)\frac{\omega_m}{2} + \frac{\omega_m^2}{4}\right], \tag{4}$$

we obtain

$$\omega = \frac{\omega_m}{4}\alpha(1 - \beta) + \frac{1}{4}\{[2(\omega_m + 2\omega_h) + \omega_m \alpha(1 - \beta)]^2 - 4\omega_m^2\beta\}^{1/2}. \tag{5}$$

Here we have $\omega_m = 4\pi\gamma M_0$, $\omega_h = \gamma H$, $\alpha = \exp(-2kd)$, $\beta = \exp(-2kt)$, $4\pi M_0$ is the saturation magnetization of the ferromagnet, and $\gamma$ is the gyromagnetic ratio. Equation (5) readily yields an expression for the surface MSW group velocity:

$$v_g = -\frac{\omega_m}{2}[t - (t + d)\beta]\alpha - \frac{\omega_m}{2}\{[t - (t + d)\beta]\alpha S - 2\omega_m d\beta\}/\{S^2 - 4\omega_m^2\beta\}^{1/2}, \tag{6}$$

where

$$S = 2(\omega_m + 2\omega_h) + \omega_m \alpha(1 - \beta). \tag{7}$$

The group velocity dispersion then has the form

$$\beta_2 = \omega_m[t^2 - (t + d)^2\beta]\alpha + \omega_m(S^2 - 4\omega_m^2\beta)^{-3/2}$$

$$\times \{(S^2 - 4\omega_m^2\beta)[S[t^2 - (t + d)^2\beta]\alpha + \omega_m[t - (t + d)\beta]^2\alpha^2 - 4\omega_m d^2\beta] - \omega_m Q^2\}, \tag{8}$$

where

$$Q = S[t - (t + d)\beta]\alpha - 2\omega_m d\beta.$$

Since the nonlinearity is assumed to be weak, the deviations of the magnetization from the equilibrium state will be small and the $z$-component of the magnetization may be expressed in the form

$$m_z = M_0[1 - (|m_x|^2 + |m_y|^2)/2M_0^2].\qquad(9)$$

Then, in the limit $kd \ll 1$, we have $m_z \approx M_0 - M_0|A|^2$ and $\omega_m \approx \omega_m(1 - |A|^2)$ (Refs. 6–12). Substituting the value of $\omega_m$ into Eq. (5) and calculating the derivative with respect to $|A|^2$, we obtain

$$\frac{d\omega}{d|A^2|}\bigg|_{A=0} = -\frac{\omega_m}{4}\alpha(1-\beta) - \left\{ \omega_m\omega_h[2+\alpha(1-\beta)] \right.$$

$$\left. + \frac{\omega_m^2}{4}[(2+\alpha)^2 - \beta\alpha^2](1-\beta) \right\} \Big/ 2$$

$$\times \left\{ \frac{\omega_m^2}{4}[(2+\alpha)^2 - \beta\alpha^2](1-\beta) \right.$$

$$\left. + 2\omega_m\omega_h[2+\alpha(1-\beta)] \right\}^{1/2}.\qquad(10)$$

A necessary condition for the formation of solitons from a surface MSW pulse is that inequality (2) hold. This condition was analyzed for values of $\omega$ and $k$ which are solutions of Eq. (5) for various distances $t$ between the metal screen and the ferromagnet. Formulas (6), (8), and (10) were tabulated for $4\pi M_0 = 1750$ H, $H = 1000$ Oe, $d = 0.001$ cm, and $k \in [1,1000]$ cm$^{-1}$.

Figure 1 gives calculated behavior of the group velocity dispersion as a function of the wave vector. It can be seen that for $t < 0.1$ cm the curves have a region of positive values. As the distance $t$ between the metal screen and the ferromagnetic film decreases, the region is shifted toward the short-wavelength part of the spectrum and disappears for a metallized ferromagnetic film. The position of the region of positive values of $\beta_2$ corresponds to the region of anomalous behavior of the dispersion dependence $\omega(k)$.

As can be seen from Fig. 2, the nonlinear coefficient $\gamma$ is less than zero for any $t$. Thus, the Lighthill criterion (2) is only satisfied for those frequencies for which the group velocity dispersion is positive.

To sum up, it has been shown theoretically for the first time that in principle, longitudinal instability may exist and envelope solitons of a surface MSW may form in a planar ferromagnetic–insulator–metal structure. It has been established that by varying the position of the metal screen relative to the ferromagnetic film, it is possible to control the frequency range of surface MSW soliton formation and its parameters.

[1] B. A. Kalinikos, N. G. Kovshikov, and A. N. Slavin, JETP Lett. **38**, 413 (1983).

[2] P. De Gasperis, R. Marcelli, and G. Miccoli, Phys. Rev. Lett. **59**, 481 (1987).

[3] V. A. Kalinikos, N. G. Kovshikov, and A. N. Slavin, Zh. Éksp. Teor. Fiz. **94**(2), 139 (1988) [Sov. Phys. JETP **67**, 303 (1988)].

[4] M. Chen, M. A. Tsankov, J. M. Nash, and C. E. Patton, Phys. Rev. B **49**, 12 773 (1994).

[5] J. N. Boyle, S. A. Nikitov, A. D. Boardman et al., Phys. Rev. B **53**, 12 173 (1996).

[6] A. K. Zvezdin and A. F. Popkov, Zh. Éksp. Teor. Fiz. **84**, 606 (1983) [Sov. Phys. JETP **57**, 350 (1983)].

[7] V. I. Karpman, Nonlinear Waves in Dispersive Media (Pergamon Press, Oxford, 1975) [Russ. original, Nauka, Moscow 1973, 176 pp.]

[8] A. D. Boardman and S. A. Nikitov, Phys. Rev. B **38**, 11 444 (1988).

[9] A. D. Boardman, Yu. G. Gulyaev, and S. A. Nikitov, Zh. Éksp. Teor. Fiz. **95**, 2140 (1989) [Sov. Phys. JETP **68**, 1238 (1989)].

[10] A. D. Boardman, S. A. Nikitov, and N. A. Waby, Phys. Rev. B **48**, 13 602 (1993).

[11] A. D. Boardman, Q. Wang, S. A. Nikitov et al., IEEE Trans. Magn. **30**, 14 (1994).

[12] A. D. Boardman, S. A. Nikitov, K. Xie, and H. Mehta, J. Magn. Magn. Mater. **145**, 357 (1995).

[13] D. S. Stal'makhov and A. A. Ignat'ev, Lectures on Spin Waves [in Russian], Saratov University Press, Saratov (1983).

[14] A. S. Kindyk, V. A. Kolosov, and L. N. Makutina, J. Mater. Sci.: Mater. Electron. **6**, 25 (1995).

[15] S. N. Bajpai, R. L. Carter, and J. M. Owens, IEEE Trans. Microwave Theory Tech. **36**, 132 (1988).

Translated by R. M. Durham

# Reconstruction of chaotic oscillations after passage through linear filters

A. A. Kipchatov and E. L. Kozlenko

''Kolledzh'' State Educational Scientific Center, Saratov State University

An analysis is made of the diagnostics of chaotic oscillations generated by a dynamic system and distorted by some linear inertial circuit. A method is developed to reconstruct the initial signal and determine the characteristics of the distorting filter using a time series of the process under study. © *1999 American Institute of Physics.* [S1063-7850(99)02602-6]

It is known that after passing through linear inertial systems, chaotic oscillations are distorted, their reconstructed attractors are more complex, and their dimension increases.[1,2]

Depending on the properties of the filter, the dimension is increased in two ways. For circuits possessing the properties of recursive filters, the initial attractor of the chaotic oscillations undergoes fractal separation (superfractalization), which causes an increase in the dimension in the infinite resolution limit ($\varepsilon \to 0$) (Ref. 3). This is a real increase in dimension. In the limit of advanced chaos and strong filtering this increase is equal to the order of the filter.[6] Circuits which possess only the properties of nonrecursive filters should not increase the dimension,[4] but the attractor should undergo some rearrangement; in this case the attractor becomes ''broken'' but conserves its fine structure. As a result, on some range of spatial scales the dimension is estimated as higher. This is an observable increase in dimension. In any case, in the range of spatial scales $[\varepsilon_{min}, \varepsilon_{max}]$ accessible to the calculations an increase in dimension will be observed with filtering and the initial dynamic system will be masked.

The question then arises, is it possible to identify any influence of these transmitting circuits without having any concept of the system design and based exclusively on information which can be gleaned from the time series of the ''black box.'' Here we show that this is indeed possible, and we also propose a procedure which can be used to achieve this in practice.

The fundamentals of the method were presented in Ref. 5 and are based on the linearity of these inertial systems, which can be used to synthesize an additional filter whose transmission characteristic is the reciprocal of that of the unknown filter. Then their total transmission characteristic will not depend on the frequency and oscillations will be observed at the exit of the additional filter, which are identical to the initial oscillations apart from a constant time shift.

Let us assume that the unknown filter has the form

$$z_n = \beta_0 x_n + \sum_{k=1}^{m} \beta_k x_{n-k} + \sum_{k=1}^{p} \alpha_k z_{n-k},$$

where $x_n$ is the input signal and $z_n$ is the output signal. The transmission characteristic of this filter has the form

$$H(\omega) = \left( \beta_0 + \sum_{k=1}^{m} \beta_k e^{-jk\omega T} \right) \Big/ \left( 1 - \sum_{k=1}^{p} \alpha_k e^{-jk\omega T} \right).$$

Then, if the transmission characteristic of the additional filter is denoted by $H'(\omega)$, the identity $H(\omega)H'(\omega) \equiv 1$ should be satisfied and $H'(\omega)$ should have the form

$$H'(\omega) = \left( 1 - \sum_{k=1}^{p} \delta_k e^{-jk\omega T} \right) \Big/ \left( \gamma_0 + \sum_{k=1}^{m} \gamma_k e^{-jk\omega T} \right),$$

where $\gamma_k = \beta_k$, $\delta_k = \alpha_k$. Assuming that there is no noise, this filter gives the same signal as the initial dynamic system at the exit.

The problem now reduces to finding the coefficients of the ''antifilter'' $\gamma_k$ and $\delta_k$. The choice of antifilter coefficients is based on the hypothesis that if chaotic oscillations were generated by a dynamic system, if $H(\omega) \not\equiv 1$, a linear filter can only increase the dimension of the attractor of these oscillations. At the same time, the attractor dimension of the oscillations at the exit of a dynamic system plus filter system can be reduced to the level of the attractor dimension of the
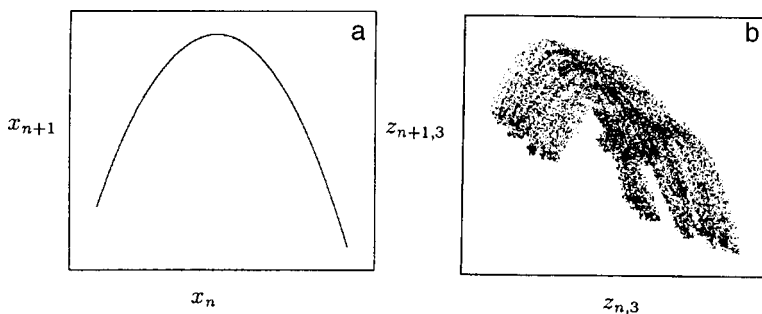


FIG. 1. Attractor reconstructed using the series $\{x_n\}$, generated by the logistic mapping (a) and attractor reconstructed using the series $\{z_{n,3}\}$ at the exit of the system (b).
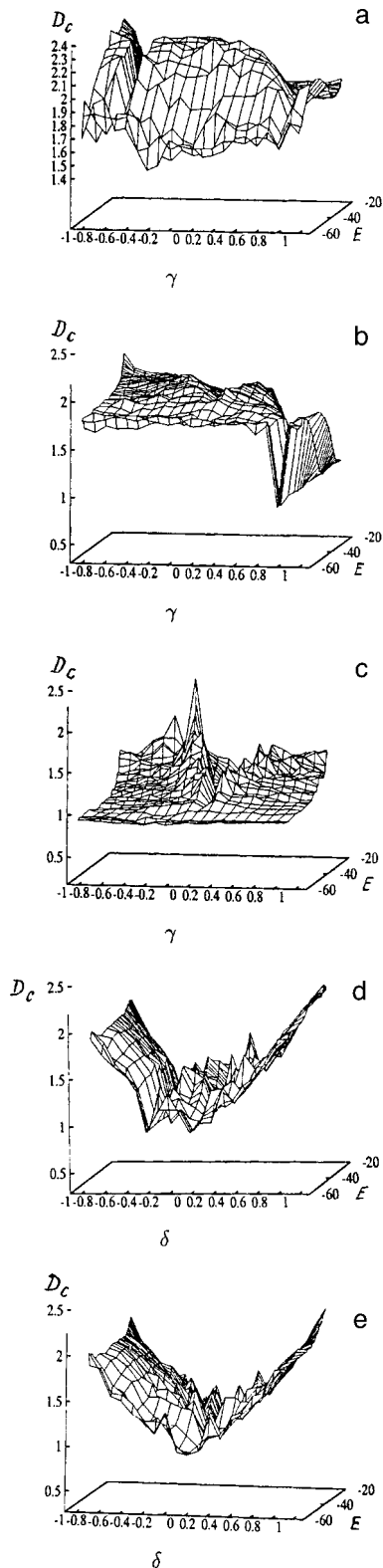
FIG. 2. Graphs of the correlation dimension as a function of the observation scale and antifilter coefficient plotted using the signal obtained at the exit of the first (a), second (b), and third (c) nonrecursive additional filters, and graphs constructed using the signal after passing through nonrecursive additional filters and through the first (d) and second (e) recursive additional filters: $D_c$ is the correlation dimension, $E$ is the spatial observation scale, and $\gamma$ and $\delta$ are the coefficients of the additional filters.

initial signal (at the exit of the dynamic system) by selecting an appropriate additional filter. Moreover, the dimension can be used as the criterion for selecting the coefficients of the additional filter.[5] We shall explain this using a simple example, considering a first-order recursive filter $z_n = \alpha_1 z_{n-1} + x_n$, where $\alpha_1 \in [-1,1]$. It is easily established that the nonrecursive filter $w_n = \beta_1 z_{n-1} + z_n$, where $\beta_1 = -\alpha_1$, should be taken as the additional filter (for which it is sufficient to substitute $z_n$ into the expression for $w_n$).

For $\beta_1 = -\alpha_1$ the attractor dimension of the signal $\{w_n\}$ will be minimal and equal to the attractor dimension of the initial signal $\{x_n\}$. For all values of $\beta_1$ the dimension will be higher, since the resultant filter will be a recursive filter with a nonzero coefficient. Thus, if the attractor dimension of the resultant oscillations is calculated for all $\beta_1 \in [-1,1]$ and the three-dimensional graph $D_c = D_c(E, \beta_1)$ is plotted, where $D_c$ is the correlation dimension and $[E = 20 \log (\varepsilon/\varepsilon_0)]$ is the scale of the observation in decibels, a minimum should be observed for $\beta_1 = -\alpha_1$.

We shall generalize this procedure to a higher-order filter. We shall assume that the unknown filter can be represented as a chain of $p$ recursive and $m$ nonrecursive filters (note that this is not always possible). The additional filter will then be represented as a chain of $m$ recursive and $p$ nonrecursive filters. The coefficients of the filters in the constructed chain can be obtained systematically by building up a chain of additional filters using this procedure.

We shall consider the following example. The system consists of the logistic mapping $x_n = 1 - \lambda x_{n-1}^2$, which generates the chaotic series $\{x_n\}$, for $\lambda = 1.9$ and chains of two recursive and one nonrecursive filter

$$z_{n,1} = x_n + \alpha_1 z_{n-1,1}$$

$$z_{n,2} = z_{n,1} + \alpha_2 z_{n-1,2}$$

$$z_{n,3} = z_{n,2} + \beta_1 z_{n-1,2}.$$

Here the first subscript indicates the discrete time and the second indicates the filter number in the chain. The values of $\alpha$ and $\beta$ lie in the range $[-1,1]$. The combined system with $\alpha_1 = -0.7$, $\alpha_2 = 0.8$, $\beta_1 = -0.4$ is a "black box" and only the series $\{z_{n,3}\}$ is accessible to analysis. The attractors reconstructed using the series $\{x_n\}$ and $\{z_{n,3}\}$ are plotted in Figs. 1a and 1b, respectively. It can be seen that the attractor of the filtered signal differs appreciably from the initial one and will not be identified as being generated by a logistic mapping by the usual methods.

We shall first attempt to determine the coefficients of the recursive filters, for which we shall use a nonrecursive filter of the form

$$w_n = z_n - \gamma z_{n-1}, \tag{1}$$

where $z_n$ is the signal at the entrance to the antifilter and $w_n$ is the signal at the exit. We shall vary the coefficient $\gamma$ between $-1$ and $+1$ with the step $\Delta \gamma = 0.1$. For each value of $\gamma$ from this range we shall calculate the correlation dimension $D_c$ for the attractor of the signal $\{w_n\}$ using an algorithm based on the method proposed by Grassberger and Procaccia.[9] The parameters of the method are: number of realization points $N = 10^5$, number of reduction points

$M = 10^4$, embedding space dimension $d = 5$, and time delay $\tau = 1$. The effective range of the spatial scales $E$ is between $-60$ and $-20$ dB. The range of large scales ($E > -20$ dB) is cut off because of the influence of edge effects,[7] while the region of small spatial scales ($E < -60$ dB) is cut off because there are insufficient points.[8] We shall use these data to plot a graph of $D_c(E, \gamma)$ for $E \in [-60, -20]$ and $\gamma \in [-1, 1]$ (Fig. 2a), which clearly shows a minimum at $\gamma = -0.7$. We assume that we have found the first recursive coefficient of the antifilter $\alpha_1 = \gamma = -0.7$ [$\alpha_1 = \gamma$ and not $-\gamma$, since $\gamma$ has a minus sign in Eq. (1)]. Now we pass the signal $\{w_n\}$ obtained for $\gamma = -0.7$ through the filter (1) and we again plot the graph $D_c = D_c(E, \gamma)$ (Fig. 2b). On this occasion a clear minimum is observed for $\gamma = 0.8$, from which we conclude that $\alpha_2 = 0.8$. At the third step no minimum is observed (Fig. 2c), so we assume that all the recursive coefficients of the antifilter are obtained.

Following the proposed method, we shall seek the coefficients of the nonrecursive links of the unknown filters using a recursive additional filter of the type $w_n = z_n - \delta w_{n-1}$. In this case, the input signal will be the signal obtained from the last additional filter of the type (1) for which a minimum was observed. The dependence $D_c = D_c(E, \delta)$ is plotted in Fig. 2d, clearly showing a minimum at $\delta = -0.4$, i.e., $\beta_1 = -0.4$. Repeating the procedure we note that no minimum is observed on the graph of the dimension and thus all the nonrecursive coefficients are obtained (Fig. 2e).

Thus, we have found $\gamma_1$, $\gamma_2$, and $\delta_1$, which completely determine the coefficients of the unknown filter and we have completely reconstructed the form of the time series of the initial dynamic system.

[1] R. Badii and A. Politi, in *Proceedings of the Workshop on Instabilities in Quantum*, 1986.
[2] T. Sauer and J. Yorke, Int. J. Bifurcat. Chaos **3**, 737 (1993).
[3] A. A. Kipchatov and L. V. Krasichkov, Pis'ma Zh. Tekh. Fiz. **21**(4), 1 (1995) [Tech. Phys. Lett. **21**, 131 (1995)].
[4] D. Broomhead, J. Huke, and M. Muldoon, J. R. Stat. Soc. B **54**, 373 (1992).
[5] A. Chennaoui, K. Pawelzik *et al.*, Phys. Rev. A **41**, 4151 (1990).
[6] A. A. Kipchatov and E. L. Kozlenko, Pis'ma Zh. Tekh. Fiz. **23**(7), 8 (1997) [Tech. Phys. Lett. **23**, 254 (1997)].
[7] M. Ding, C. Grebogi, E. Ott *et al.*, Physica D **69**, 404 (1993).
[8] A. A. Kipchatov, Pis'ma Zh. Tekh. Fiz. **21**(15), 90 (1995) [Tech. Phys. Lett. **21**, 627 (1995)].
[9] P. Grassberger and I. Procaccia, Phys. Rev. Lett. **50**, 346 (1983).

Translated by R. M. Durham

# Two-level control of chaos in nonlinear oscillators

B. P. Bezruchko, R. N. Ivanov, and V. I. Ponomarenko

*Institute of Radio Engineering and Electronics, Russian Academy of Sciences (Saratov Branch)*

Control of chaos was achieved experimentally for the first time in a nonautonomous $RL$-diode circuit using a two-level system and modeled numerically using a multiparameter one-dimensional mapping). This system is a modification of the classical Ott–Grebogi–Yorke method but is distinguished by its ease of implementation in real systems. © *1999 American Institute of Physics.* [S1063-7850(99)02702-0]

1. The experimental implementation of methods of controlling chaos in nonlinear systems frequently comes up against the complexity of the algorithms for the variation of the control parameter and requires the development of simpler variants. Such approaches may include the modification of the Ott–Grebogi–Yorke method[1] proposed in Ref. 2, in which the variation of the parameter $p$, which in the classical variant is proportional to the deviation of the state of the system from that being stabilized, is replaced by switching between two fixed values $p$ and $p_2$, i.e., by the two-level equation

$$p = p_0 + k \, \text{sgn}(x_n - x_0) = \begin{cases} p_1, & \text{if } x_n \leq x_0 \\ p_2, & \text{if } x_n > x_0, \end{cases} \quad (1)$$

where $k = (p_2 - p_1)/2$, $p_0 = (p_1 + p_2)/2$, $p_2 > p_1$, and $x_n$ and $x_0$ are the instantaneous value of the variable and the value on the stabilized unstable orbit in the Poincaré cross section (in general a vector).

Here two-level stabilization is achieved in physical and numerical experiments in two variants: (a) with the algorithm (1) "switched on" when the mapping point in the phase space reaches a given vicinity of the stabilized orbit (on entering a "window") and (b) in a simpler variant under the continuous action of the algorithm (1) without introducing a window. The objects of the investigation are a nonlinear dissipative oscillator periodically excited by an external force, i.e., a nonautonomous $RL$ diode circuit (shown by the heavy line in Fig. 1) and a multiparameter one-dimensional mapping which accurately models the complex dynamics of the experimental system in the subharmonic resonance frequency range:

$$x_{n+1} = A + x_n \exp(-d/N) \cos(2\pi/(N(1 + \beta x_n))), \quad (2)$$

where $A$ is the analog of the amplitude of the external action, $N = T_0/T$ is the normalized frequency of the action, $d$ characterizes the dissipation, $\beta$ is the nonlinearity parameter, and $n = 1,2,3\ldots$ is the discrete time.[1]

We demonstrate the efficiency of this simplified control procedure and analyze its capabilities and shortcomings: the motion takes place in a given range of the dynamic variable near a selected orbit; an increase in the period of the stabilized motion is accompanied by a decrease in the range of parameters in which stabilization is possible.

2. We shall first analyze the two-level control procedure using the multiparameter mapping (2), which we rewrite in the form $x_{n+1} = A + f(x_n)$, where $A$ is the control parameter. In the immediate vicinity of the fixed point $x_0$, the dynamics of the system are described by

$$x_0 + \tilde{x}_{n+1} = A_0 + f(x_0) + \left. \frac{df}{dx_n} \right|_{x_0} \tilde{x}_n + \tilde{A}_n, \quad (3)$$

where $\tilde{x}_{n+1}$ and $\tilde{x}_n$ correspond to small perturbations and the variation of the control parameter $\tilde{A}_n$ is also introduced for control purposes. We separate Eq. (3) into the equation for the fixed point

$$x_0 = A_0 + f(x_0) \quad (4)$$

and the equation for the variations

$$\tilde{x}_{n+1} = \tilde{A}_n + \left. \frac{df}{dx_n} \right|_{x_0} \tilde{x}_n. \quad (5)$$

We set ourselves the task of using $\tilde{A}_n$ to restrict the motion to the immediate vicinity of the unstable fixed point $x_0$ (an unstable cycle of period 1) for values of the parameters $A_0$, $\beta$, $d$, and $N$ corresponding to chaos. For this purpose we determine the value of $x_0$ from Eq. (4), find the derivative of the function $f$ at this point, and define the window $\sigma$. We then iterate Eq. (3) beginning with various initial conditions until $x_n$ is within $\sigma$ of the point $x_0$, i.e., $|\tilde{x}_n| < \sigma$. The parameter $\tilde{A}_n$ should then be varied in accordance with rule (1) ($\tilde{A}_n = k$ for $x_n > 0$; $\tilde{A}_n = -k$ for $x_n < 0$), so that the mapping point does not leave the given vicinity of the fixed point, $|\tilde{x}_{n+1}| < \sigma$. This is possible if, in accordance with Eq. (5), the following inequality is satisfied:

$$-\sigma \left( 1 + \left. \frac{df}{dx_n} \right|_{x_0} \right) < k < \sigma. \quad (6)$$

Thus, the condition for finding $x_n$ near a fixed point of period 1 is $(df/dx_n)_{x_0} > -2$. This series of actions is easily trans-
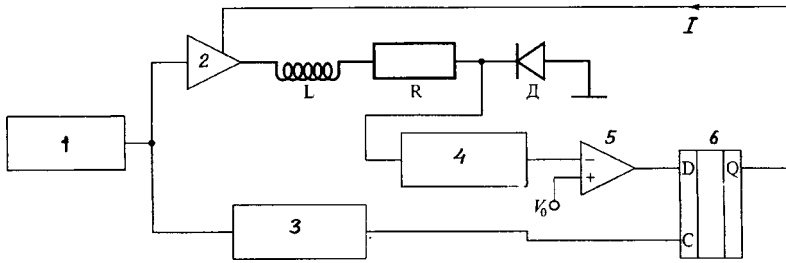
FIG. 1. Schematic of experiment (the heavy line indicates the system being studied): *1* — oscillator, *2* — amplifier, *3* — pulse shaper, *4* — amplitude detector, *5* — comparator, *6* — trigger, and *I* — control circuit.

ferred to cycles of period $m = 2,4,8\ldots$, if we use formulas for the corresponding iterations $x_{n+m} = f^m(x_n)$ rather than Eq. (2).

The results of numerical experiments to implement this control procedure using the mapping (2) for values of $A_0$, $\beta$, $d$, and $N$ corresponding to chaos are plotted in Fig. 2. With no control the steady-state motion of the system on the phase plane takes place on a chaotic attractor occupying an extended region of the parabola (Fig. 2a), but when the control is switched on it is confined to a given vicinity of the point $x_0$. The degree of ''compression'' of the attractor and the duration of the establishment process (between switching on the control and stabilization) is determined by the choice of $k$: for small $k$ the values of $x_n$ are positioned near $x_0$, as $k$ increases the spread of $x_n$ increases and the duration of the transition process decreases. This is illustrated by the time series of the oscillations in the system shown in Figs. 2b and 2c: for $k = 0.05$ stabilization occurs after 80 iterations, whereas for $k = 0.1$ it occurs after around 20. The calculations show that two-level control can also stabilize the motion near unstable cycles of period 2 and 4. However, the higher the period of the unstable cycle, the larger the factor multiplying the absolute value and the smaller the region in which stabilization can be achieved.

We shall simplify the control procedure by retaining two fixed values $A_0 + k$ and $A_0 - k$ after the parameter $A$ but removing the condition that $x_n$ must lie within $\sigma$ of the fixed point of period 1. In this case, the control parameter $A$ does not have values of $A_0$ as in the previous case. The calculations show that the new procedure also stabilizes the motion near the fixed point of period 1 but appreciably simplifies the experimental implementation of the control system.

3. In a physical experiment, the two-level control scheme (Fig. 1) was constructed in accordance with the second (simplified) variant of those considered in Sec. 2. An $RL$ circuit with a diode ($L = 100\,\mathrm{mH}$, KD202 diode) was excited by a pulsed signal from a generator via an amplifier. The gain $p$ could have two values: $p_1 = 1$ and $p_2 = 1 + \Delta$, where $\Delta$ was varied between 0.00 and 0.07 during the experiment. The control system was used to compare the voltage $V$ at the diode and at the reference voltage source $V_0$ at times when the external action has a certain phase. Depending on the sign of $V - V_0$ the level of the exciting signal was set at one of two values. The form of the stabilized motion was determined by defining the reference voltage $V_0$, the value of $\Delta$, and the time interval between the comparisons of the diode and reference voltage. Note that as in Ref. 2, there are two levels of the control parameter $p_1$ and $p_2$ in the experimental

procedure, but the control parameter never has the value $p_0 = (p_2 + p_1)/2$.

The results of the experimental investigations showed that the simplified two-level control variant is effective and revealed qualitative agreement with the results of the numerical modeling. Figure 2d illustrates the stabilization of the motion near an unstable cycle of the period of the external action for the case, where before control was switched on chaotic oscillations existed in the system, formed as a result of a series of doubling bifurcations of this cycle.[2] This figure
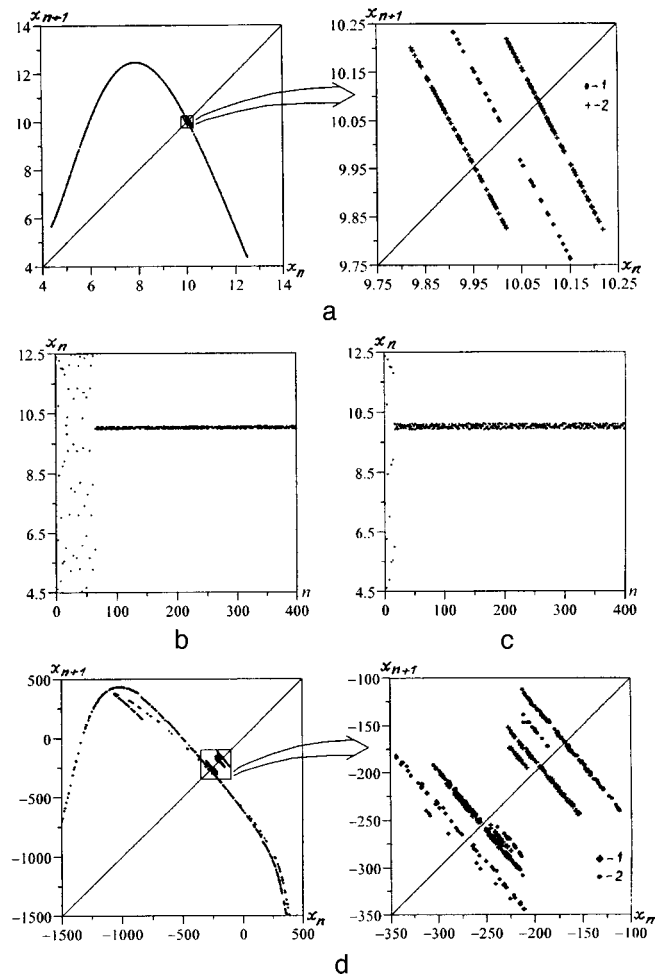


FIG. 2. a — Mapping on the plane $x_{n+1}$–$x_n$ with control switched off (*1*) and switched on (*2*); b, c — time series of oscillations in the system (2) for $A_0 = 7$, $d = 0.13$, $\beta = 0.205$, $N = 0.4$ for the same initial conditions for $k = 0.05$ and $k = 0.10$, respectively; d — mapping of the sequence of the experimental system without control (*1*) and with control for $\Delta = 0.04$(*1*) and $\Delta = 0.07$ (*2*).

gives the dependence $V_{i+1}(V_i)$, where $V_i$ is the voltage at the diode at discrete times $i$ after the period of action. The main diagram shows the case where the control system is switched off and the magnified fragment gives the dependence after switching on the control for various values of $\Delta$ (crosses denote $\Delta = 0.04$ and circles $\Delta = 0.07$). As in the numerical experiment, when the control is switched on, the points in the stroboscopic cross section form piecewise linear sets with a discontinuity near the reference value. As $\Delta$ decreases, the vicinity of the unstable cycle visited by the mapping point becomes shorter. As $\Delta$ approaches zero, control is abruptly terminated.

4. A two-level control system can organize the motion of the system in a given range of the phase space of nonautonomous oscillators in chaotic motion based on any of the subharmonic cycles. The method is fairly approximate and is stable with respect to the unavoidable perturbations in a physical experiment. An advantage of this control system is that the algorithm and thus the design of the control circuits is extremely simple. However, it can only confine the motion in a given interval and is not suitable for prolonged motion on an unstable orbit, as in the classical stabilization procedure.

[1]An *RL* diode circuit is widely used as a selective element with electronic tuning, as a frequency divider and multiplier, and has been considered as a memory cell with phase recording of information,[5] but recently, following the observation of chaotic dynamics[3] in this circuit, it has become a test bed for studying various nonlinear oscillatory phenomena. The model mapping (2) was obtained for dissipative oscillators with ''soft spring'' nonlinearity, periodically excited by forcing pulses during which additional losses are introduced into the system. For an *RL* diode circuit this is achieved when the pulses are positive for the diode.[4]

[2]The thickening of the lines of the experimental mapping and their separation in Fig. 2d is caused by the real system not being one-dimensional and by technical factors (the unavoidable propagation of the control signal of the electronic switch into the excitation signal of the oscillator circuit.

[1] E. Ott, C. Grebogi, and J. A. Yorke, Phys. Rev. Lett. **64**, 1196 (1990).

[2] Z. Galias and M. J. Ogorzalek, in *Proceedings of the Third International Workshop on Nonlinear Dynamics of Electronic Systems, NDES'95*, Dublin, Ireland, 1995, pp. 229–232.

[3] P. S. Linsay, Phys. Rev. Lett. **47**, 1349 (1981).

[4] B. P. Bezruchko, M. D. Prokhorov, and E. P. Seleznev, Chaos Solitons Fractals **5**, 2095 (1995).

[5] A. E. Kaplan, Yu. A. Kravtsov, and V. A. Rylov, *Parametric Oscillators and Frequency Dividers* [in Russian], Sovet-skoe Radio, Moscow (1966), 334 pp.

Translated by R. M. Durham

# Investigation of inhomogeneities in thin films of high-temperature superconductors by scanning probe microscopy

A. K. Vorob'ev, N. V. Vostokov, S. V. Gaponov, E. B. Klyuenkov, and V. L. Mironov

*Institute of Microstructure Physics, Russian Academy of Sciences, Nizhniĭ Novgorod*
(Submitted August 18, 1998)
Pis'ma Zh. Tekh. Fiz. **25**, 68–73 (February 26, 1999)

Scanning tunneling microscopy and atomic force microscopy were used to study inhomogeneities in thin films of Y–Ba–Cu–O high-temperature superconductors caused by secondary-phase precipitates. It was established that Y–Ba–Cu–O films with high global critical parameters may constitute a complex heterogeneous system containing regions of different thickness and electrical properties. It is shown that these inhomogeneities may strongly influence the parameters of devices formed using these films. © *1999 American Institute of Physics.*
[S1063-7850(99)02802-5]

Various elements and devices fabricated using thin films of high-temperature superconductors (HTSCs) are now extensively used in electronics. These particularly include passive microwave elements such as antennas, filters, and dividers and devices based on Josephson junctions such as Squid magnetometers and voltage standards. In addition to having high global values of the critical parameters (such as the zero resistance temperature and critical current), thin HTSC films should possess the required local uniformity of the properties for the reproducible fabrication of high-quality device structures. The required degree of uniformity is mainly determined by the $\sim 1-10\,\mu$m dimensions of the working regions and the $\sim 10$ nm barrier thicknesses in multilayer structures.

At present, various *in situ* methods are used to fabricate reproducible films with high critical parameters (for example, the best Y–Ba–Cu–O films have a zero resistance temperature of $\sim 92$ K and a critical current density of $\sim 10^6-10^7$ A/cm$^2$ at 77 K). However, despite the high electrical characteristics, these films are generally a complex heterogeneous system containing both the stoichiometric superconductor phase and various phases of the initial components.[1–3] The phases of the initial components exist in the films in the form of isolated particles (so-called secondary-phase particles or precipitates) having dimensions of up to 1 $\mu$m and a surface density of up to $10^{10}$ cm$^{-2}$ (Refs. 3 and 4). Thus, they may influence the properties of the fabricated devices.

It is therefore important to investigate how the inhomogeneities caused by secondary-phase particles in HTSC films influence their electrophysical parameters. In addition to the conventional methods such as scanning and transmission electron microscopy, and x-ray diffractometry, methods of scanning probe microscopy have recently been increasingly widely used to study inhomogeneities in HTSC films. In particular, these techniques include tunneling microscopy and atomic force microscopy,[5–7] which can reveal the surface relief and the distribution of the electrical properties of HTSC films with high spatial resolution.

Here we present results of an investigation of inhomo-geneities in Y–Ba–Cu–O films caused by the presence of secondary-phase particles, carried out using scanning tunneling microscopy and atomic force microscopy.

The Y–Ba–Cu–O films were deposited *in situ* in an inverted cylindrical magnetron sputtering system.[8] Films $\sim 50$ nm thick were deposited on NdGaO$_3$ substrates under conditions optimized in terms of the electrical properties.[9] The zero resistance temperature of the films was 90–91 K and the critical current density was $\sim (2-5) \times 10^6$ A/cm$^2$ at 77 K. The films contained copper-enriched secondary-phase particles (CuO) having dimensions of 0.1–0.5 $\mu$m and a surface density of up to $10^8$ cm$^{-2}$, which were evidently formed during the *in situ* growth process as a result of the condensate composition departing from stoichiometric.[10]

The surface relief of the films was investigated using an NT-MDT (Zelenograd, Russia) atomic force microscope (AFM) and the tunneling investigations were carried out using a scanning tunneling microscope (STM) of our own design.[11] This allowed us to study the electrophysical properties of the films in addition to the relief characteristics. The AFM examination of the surface relief showed that the precipitates are surrounded by $\sim 0.5\,\mu$m areas of film whose thickness is 3–5 nm less than the thickness of the main Y–Ba–Cu–O layer (Fig. 1). This is consistent with the results of Ref. 12, where similar regions were observed at the early stages of film growth.

More detailed studies of the regions adjacent to the precipitates were made using the STM. A study of the tunneling current–voltage characteristics obtained in different parts of the film showed that the secondary-phase CuO particles have current–voltage characteristics typical of a *p*-type metal–semiconductor Schottky barrier. Moreover, the return branch of the characteristic (sample voltage $U < 0$) obtained near a CuO particle has a low-current section determined by minority carriers and a rising current section ($U \lesssim -2--3$ V depending on the site) typical of avalanche breakdown in semiconductors. The CuO particles are surrounded by regions having current–voltage characteristics typical of a metal–metal tunnel junction (the STM tip was made of beryllium
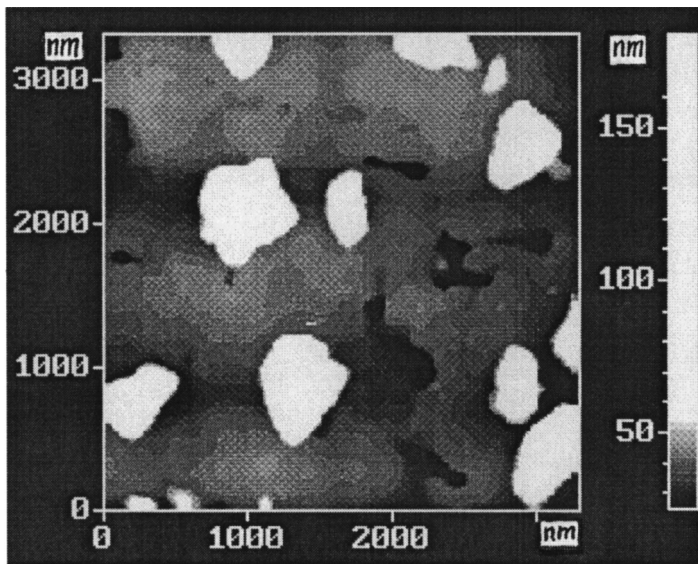
FIG. 1. AFM image of the surface relief of a Y–Ba–Cu–O film. The contrast of the image is selected so that the regions of film around the precipitates are more clearly visible.

bronze). The surface relief was recorded at a voltage across the tunnel gap $U \sim +1.5$ V, which corresponded to the forward branch of the current–voltage characteristic of a CuO particle. At each point on the scan the feedback loop was broken, the current–voltage characteristic was obtained, and the current was recorded at voltages across the tunnel gap corresponding to the return branch of the semiconductor characteristic. Thus, an image of the current distribution between the tip and the sample was formed at the same time as the relief. The contrast of this image is such that the semiconductor regions are sharply distinguished from the regions of metallic conductivity.

A typical image of the relief and the corresponding current distribution are shown in Fig. 2. On the image of the current distribution (Fig. 2b) the precipitates are far less localized than on the image of the relief (Fig. 2a) as a result of the overlap of regions with semiconducting properties. More detailed information on the properties of the film near the
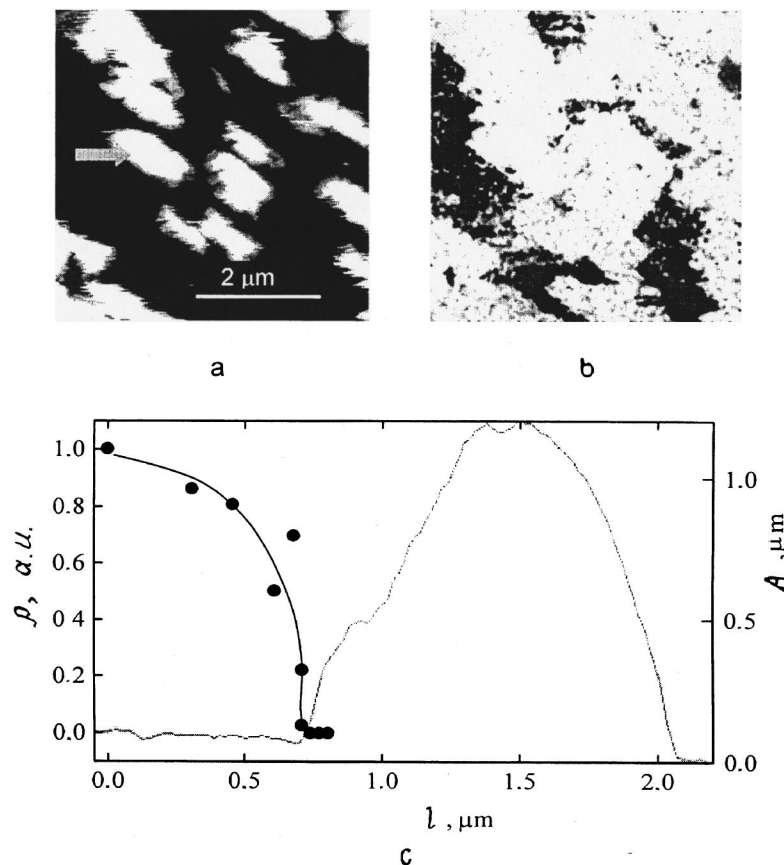


FIG. 2. a — STM image of the surface relief of a Y–Ba–Cu–O film obtained for $j_t$=const, sample potential $U$=1.5 V, and confinement current $j_t$=200 pA. The arrow shows the cross section along which the conductivity distribution was recorded. b — current distribution (for $U$=−1.5 V) between the tip and the Y–Ba–Cu–O sample in the region corresponding to that shown in Fig. 2a. The dark areas on the image correspond to higher current. c — surface relief along the arrow shown in Fig. 2a and corresponding distribution of the relative differential conductivity for $U$=0 ($l$ — coordinate, $A$ — profile).

precipitate is provided by the profile of the differential conductivity shown in Fig. 2c. It can be seen that near the precipitates there are regions of film having dimensions of around 0.5 $\mu$m with low tunnel conductivity. The reduction in the conductivity of these regions may be attributed to a change in their electrophysical properties as a result of the diffusive depletion in Cu atoms during the *in situ* growth process.[4] On the basis of an analysis of changes in the diffusion of Cu adatoms as a function of the condensation temperature, Drozdov *et al.*[4] suggested that precipitates may be surrounded by regions with a Cu atom deficiency. It was shown that if the size of these regions becomes comparable with the distances between the precipitates, they can substantially influence the global properties of the condensate which determine the parameters of microwave devices. The results presented here provide direct experimental confirmation of these assumptions. In addition, these results show that inhomogeneities in the form of precipitates with adjacent nonstoichiometric regions of film may strongly influence the parameters of devices based on Josephson junctions, since the typical sizes of the inhomogeneities are comparable with the sizes of the working regions.

Thus, even Y–Ba–Cu–O films with high global critical parameters are usually a complex heterogeneous system containing secondary-phase particles and regions of film of different thickness and electrical properties. The dimensions of the inhomogeneities are comparable with the distances between the precipitates and with the characteristic sizes of the working regions of the devices. Thus, these inhomogeneities may have a substantial influence on the parameters of microwave devices and devices based on Josephson junctions.

[1] K. Verbist, A. L. Vasiliev, and G. Van Tendeloo, Appl. Phys. Lett. **66**, 1424 (1995).

[2] W. Rauch, H. Behner, G. Gieres *et al.*, Physica C **198**, 389 (1992).

[3] Zhenge Han, T. I. Selinder, and U. Helmersson, J. Appl. Phys. **75**, 2020 (1994).

[4] Yu. N. Drozdov, S. V. Gaponov, S. A. Gusev *et al.*, Supercond. Sci. Technol. A **9**, 166 (1996).

[5] Koguchi Kazumasa, Matsumoto Takuya, and Kawai Tomoji, Science **267**, 71 (1995).

[6] B. Dam, N. J. Koeman, J. H. Rector *et al.*, Physica C **261**, 1 (1996).

[7] K. H. Wu, R. C. Wang, S. P. Chen *et al.*, Appl. Phys. Lett. **69**, 421 (1996).

[8] A. K. Vorob'eva, E. V. Klyuenkov, V. V. Talanov *et al.*, Pis'ma Zh. Tekh. Fiz. **19**(17), 785 (1993) [Tech. Phys. Lett. **19**, 479 (1993)].

[9] Yu. N. Drozdov, S. V. Gaponov, S. A. Gusev *et al.*, IEEE Trans. Appl. Supercond. **7**, 1642 (1997).

[10] Y. N. Drozdov, S. V. Gaponov, S. A. Gusev *et al.*, in *Extended Abstracts of ISEC'97*, Vol. 2 (1997), p. 49.

[11] D. G. Volgunov, S. V. Gaponov, V. F. Dryakhlushin *et al.*, Prib. Tekh. Éksp. No. 2, 132 (1998).

[12] J. A. Alarco, J. Brorsson, H. Olin *et al.*, J. Appl. Phys. **75**, 3202 (1994).

Translated by R. M. Durham

# Synchronization of the heartbeat rate of Daphnia by an external electric field

D. A. Usanov, Al. V. Skripal', and An. V. Skripal'

*N. G. Chernyshevskiĭ State University, Saratov*

Experimental investigations were made of the influence of an external alternating voltage on the amplitude and heartbeat rate of Daphnia freshwater crayfish. It was observed that the heartbeat rate of Daphnia was synchronized by an external electric field. © *1999 American Institute of Physics.* [S1063-7850(99)02902-X]

The phenomenon of synchronization and locking of an oscillator frequency by an external signal is well-known and extensively used in radioelectronics. It may be postulated that a similar mechanism for influence of an external signal should also be observed for oscillators of a different type. The heart of a biological specimen may be considered to be a particular type of oscillator (self-oscillatory system). It is most interesting to study the influence of an external signal on biological objects used as test specimens for ecological research. These include, in particular, Daphnia, for which the method of studying the heart-beat amplitude and rate was described in detail in Ref. 1.

We investigated the influence of an external electric field on the heartbeat rate and amplitude of Daphnia at external field frequencies close to the heartbeat rate and under conditions where the field frequency differed appreciably from the normal heartbeat rate.

The experimental investigations were carried out using the system shown in Fig. 1. Radiation from a semiconductor laser 7 (ILPN-206) stabilized by a current source 8 was fo-

cused by a lens 6 into the heart region of a specimen of Daphnia 3, which was inserted in a channel 4 on a transparent stage 5. The aqueous medium accommodating the Daphnia was contained in a glass receptacle 13 and electrodes 14 connected to a voltage source U were inserted in this medium. A night viewing device 1 was used to observe the infrared semiconductor laser radiation and its focusing into the heart region. Some of the radiation reflected by the Daphnia heart was returned to the semiconductor laser cavity and the change in its output power was recorded by a photodetector 9 (Ref. 2). The photodetector signal was passed via an amplifier 10 and an analog-to-digital converter 11 to a computer 12. The Daphnia heartbeat rate and amplitude were determined as described in Ref. 1.

Daphnia freshwater crayfish (*Daphnia magna Straus*) were bred under standard laboratory conditions. For the experiments we used specimens measuring 0.7–1.5 mm. A single Daphnia from the aquarium was placed in a chamber which restricted its movement. The chamber was attached to a microscope stage. The optical system was directed toward
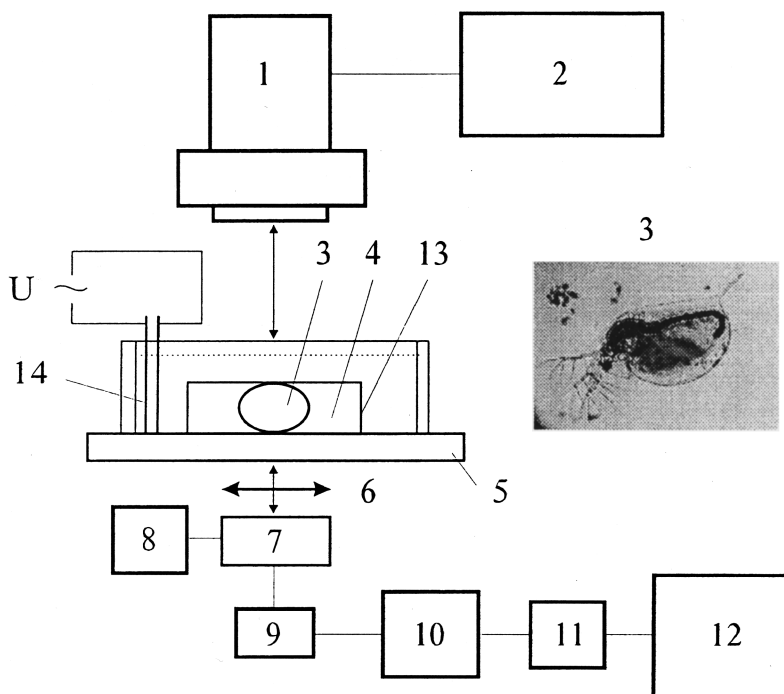


FIG. 1. Schematic of apparatus to study the influence of an external electric field on the Daphnia heartbeat rate and amplitude.
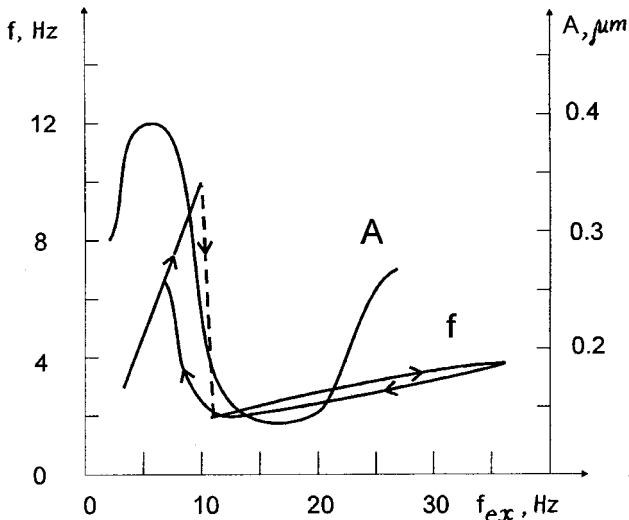
FIG. 2. Daphnia heartbeat rate and amplitude as a function of the frequency of an external periodic signal: the arrows indicate the direction of variation of the signal frequency.
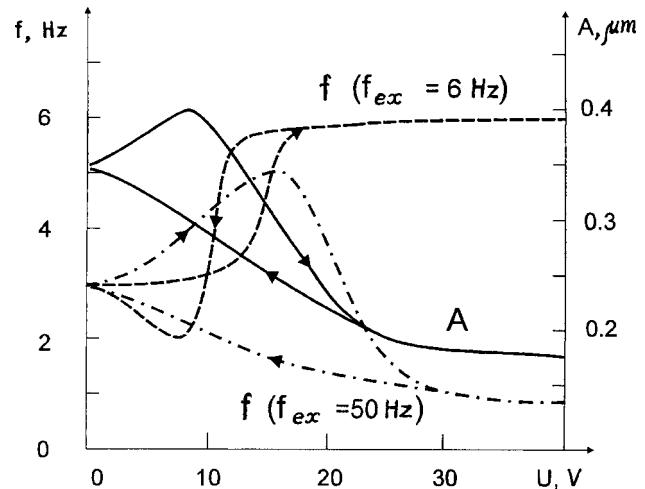


FIG. 3. Daphnia heartbeat rate and amplitude as a function of the amplitude of an external periodic signal: the arrows indicate the direction of variation of the signal amplitude.

the heart and the apparatus tuned to the maximum signal.

In the experiments, an ac electric field of different amplitude and frequency was used as the external perturbing influence. The influence of this field on the operation of the Daphnia heart was assessed from the change in the heartbeat amplitude and rate.

The experiments showed that the action of an ac electric voltage synchronizes the heartbeats with the frequency of this voltage. Figure 2 gives the rate $f$ and amplitude $A$ of the Daphnia heartbeats as a function of the frequency of the periodic signal when the amplitude of the external voltage is $U = 10$ V. It can be seen from these results that synchronization is observed at external voltage frequencies between 3 and 10 Hz, for which the heartbeat rate exactly matches the increasing frequency of the external signal. For $f_{ex} > 11$ Hz the synchronization is destroyed, the Daphnia heartbeat rate and amplitude decrease sharply and then begin to increase again with increasing $f_{ex}$. When the frequency of the external signal was decreased, the dependence of $f$ on $f_{ex}$ followed a different trajectory as far as $f_{ex} = 7$ Hz, i.e., this dependence exhibited unique hysteresis behavior. From 7 Hz onward the Daphnia heartbeat rate and the frequency of the external signal again coincided.

Figure 3 gives the Daphnia heartbeat rate and amplitude as a function of the amplitude of the external periodic signal. Under the experimental conditions, in the absence of any external signal the Daphnia heartbeat amplitude and rate were 0.35 $\mu$m and 3 Hz, respectively. The results plotted in Fig. 3 show that the action of an external ac voltage on the Daphnia heartbeat rate is a threshold process. At an external signal frequency of 6 Hz an increase in the voltage from zero to a threshold value $U = 8$ V did not appreciably change the

heartbeat rate. A further increase to $U > 8$ V caused a rapid increase in the heartbeat rate until this coincided with the frequency of the external periodic signal at $U > 16$ V. That is to say, synchronization and locking of the Daphnia heartbeat rate with the frequency of the external ac voltage were observed.

As the amplitude of the external signal decreased, synchronization was sustained in the range $12 \, \text{V} < U < 16$ V. The dependence of $f$ on $U_{ex}$ also exhibited hysteresis behavior.

The dependence of the Daphnia heartbeat rate showed slightly different behavior under the action of an external signal at frequency 50 Hz. As the voltage amplitude increased from 0 to 16 V, the Daphnia heartbeat rate increased, although the oscillations were not synchronized with the external alternating voltage. At the maximum of the curve $f(U)$ the value of $f$ was 5 Hz. A further increase in the amplitude of the external signal $U > 16$ V caused the Daphnia heartbeat rate to fall to values substantially lower than those in the absence of an external voltage. When the alternating voltage decreased from values higher than 40–48 V, the heartbeat rate increased monotonically from 1 to 3 Hz. The dependence of the Daphnia heartbeat amplitude as a function of the alternating voltage had a maximum at $U \approx 8$ V. A further increase in $U$ resulted in a monotonic decrease in the Daphnia heartbeat amplitude. This dependence also exhibited hysteresis behavior.

These investigations suggest that the Daphnia heartbeat rate is synchronized by an external electric field.

[1] D. A. Usanov, Al. V. Skripal', A. Yu. Vagarin, An. V. Skripal', V. V. Potapov, T. T. Shmakova, and S. S. Mosiyash, Pis'ma Zh. Tekh. Fiz. **24**(5), 39 (1998) [Tech. Phys. Lett. **24**, 183 (1998)].

[2] D. A. Usanov, A. V. Skripal', and M. Yu. Kalinkin, Izv. Vyssh. Uchebn. Zaved. Prikl. Nelin. Dinam. **6**(1), 3 (1998).

Translated by R. M. Durham

# Phase shift of surface magnetostatic waves propagating in nonuniformly magnetized ferrite films and ferrite–metal structures

V. A. Zubkov and V. I. Shcheglov

*Institute of Radio Engineering and Electronics, Russian Academy of Sciences, Fryazino*
(Submitted June 10, 1998)
Pis'ma Zh. Tekh. Fiz. **25**, 79–84 (February 26, 1999)

It is shown that when surface magnetostatic waves propagate in a ferrite–metal structure magnetized by a linearly nonuniform field, the phase shift of these waves is many times greater than that accompanying propagation in a ferrite film and also in a ferrite–metal structure magnetized by a uniform field, and may reach extremely high values of tens of thousands of radians. This indicates that ferrite–metal structures magnetized by nonuniform fields are potentially useful for developing microwave shifters. © *1999 American Institute of Physics.*
[S1063-7850(99)03002-5]

Surface magnetostatic waves (SMSWs) propagating in tangentially magnetized ferrite films and in film structures based on these are used to develop a wide variety of information processing devices in the microwave band.[1–4] By using nonuniform magnetizing fields, it is possible to reduce the geometric dimensions of known devices and also to fabricate devices based on completely new principles.[5–9] The trajectories of SMSWs and also the changes in the wave number and vectors of the phase and group velocities of a wave propagating[7–9] in a nonuniform magnetizing field $H_g$ have now been studied, but the phase shift of these waves has yet to be determined. However, a knowledge of the phase shift is needed to design phase shifters and various multifunctional microwave devices. Here for the first time we calculate the phase shift for SMSWs propagating in the field $H_g$.

We investigated the phase shift accompanying the propagation of SMSWs in a ferrite film and in a ferrite film with a metallized surface, which we shall subsequently call a ferrite–metal structure. The calculations were made using a geometric-optics method.[7–9] The ferrite film and the ferrite–metal structure were magnetized by a linearly nonuniform film $H_g$. We choose the coordinate system so that the $yz$ plane coincides with the plane of the ferrite film and the $x$ axis is perpendicular to it. A magnetizing, linearly nonuniform film $H_g$ is applied in the plane of the film along the $z$ axis. Its direction remains constant and the strength depends on the $z$ coordinate as given by

$$H_g = H_z(z) = 4\pi M_0(\Omega_H + za^{-1}), \tag{1}$$

where $4\pi M_0$ is the saturation magnetization of the ferrite film, $\Omega_H = H_0(4\pi M_0)^{-1}$, and $H_0$ is the uniform component of the field $H_g$.

We shall assume that a surface magnetostatic wave of frequency $\omega_i = 2\pi f_i$ and wave number $k_i$ is excited at the origin and the vector of its phase velocity forms the angle $\varphi$ with the $y$ axis (at the excitation point $\varphi = \varphi_0$). The phase shift $\Phi$ is defined as the integral of the product of the wave vector and the distance along the SMSW trajectory $z(y)$:

$$\Phi = \int_{y_b}^{y_e} k(y, z(y))\sqrt{1 + (dz/dy)^2}\,dy, \tag{2}$$

where $y_b$ and $y_e$ are the $y$ coordinates of the initial and final points of the trajectory. The SMSW trajectories $z(y)$ and the dependences of the wave number $k(y)$ and the angles of inclination of the vectors of the phase $\varphi(y)$ and group $\psi(y)$ velocities were calculated using a method described in Refs. 7–9.

We recall[8,9] that for angles $\varphi_0 > 0$, the SMSW trajectories are parabolic: the SMSW initially propagates in the direction of decreasing field $H_g$ (decreasing $z$) and then turns toward increasing $H_g$ (increasing $z$). An SMSW with constant frequency $\Omega_i = \omega_i(4\pi\gamma M_0)^{-1}$ ($\gamma$ is the magnitude of the electron gyromagnetic ratio) and angle $\varphi_0$ in the field $H_g$ can only propagate in the range of variation of the field $\delta H = H_{gu} - H_{gi}$. The limits of the range $\delta H$ are determined from the dispersion relation for an SMSW in ferrite film and ferrite–metal structures for $\Omega_i = $ const.

The upper limit $\Omega_{gu} = H_{gu}(4\pi M_0)^{-1}$ is given by:[8,9]

$$\Omega_{gu} = 0.5(\sqrt{4\Omega_i^2 + 1} - 1). \tag{3}$$

The lower limit $\Omega_{gl} = H_{gl}(4\pi M_0)^{-1}$ is given by for a ferrite film[8]

$$\Omega_{gl} = 0.5(\sqrt{4\Omega_i^2 + \exp(-2k_{y,i}d)} - 1), \tag{4}$$

for a ferrite–metal structure[9]

$$\Omega_{gl} = \frac{-(1 + \varkappa_{+1}) + \sqrt{(2\varkappa_{+1}\Omega_i - 1)^2 + \varkappa_{+1}\varkappa_{-1}}}{2\varkappa_{+1}}, \tag{5}$$

where $\varkappa_{-1} = \coth k_{y,i}d - 1$ and $\varkappa_{+1} = \coth k_{y,i}d + 1$, $k_{y,i}$ is the projection of the wave vector on the $y$ axis, and $d$ is the thickness of the ferrite film.

When the field in the ferrite film and the ferrite–metal structures reaches $\Omega_{gl}$ the direction of propagation of the SMSW rotates, and when the field in the ferrite film reaches
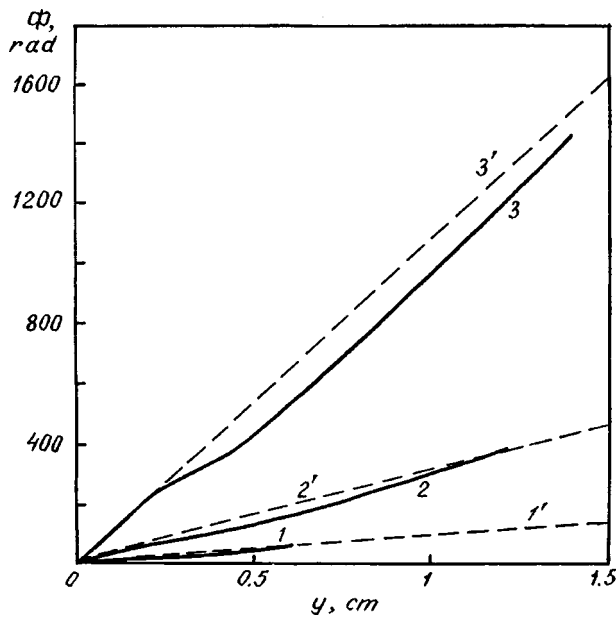
FIG. 1. Phase shift of SMSWs at various frequencies in a ferrite film. The solid curves are plotted for SMSWs in the field $H_g$ and the dashed curves in the field $H_0$. Curves: $1 — f = 2.9$ GHz, $2 — f = 3.1$ GHz, and $3 — f = 3.3$ GHz.

$\Omega_{gu}$ the SMSW undergoes specular reflection.[7–9] This is responsible for the parabolic form of the SMSW trajectories $z(y)$ and the functions $k(y)$.

The calculations were made for the following values of the parameters: $\Omega_H = 0.25$, $a = 8$ cm$^{-1}$, $4\pi M_0 = 1750$ Gs (yttrium iron garnet film), $d = 15\,\mu$m, and the angle $\varphi_0 = 30°$. The results are plotted in Figs. 1 and 2.

Figure 1 gives the phase shift $\Phi$ as a function of the distance $y$ for SMSWs with various frequencies in a ferrite film. It can be seen that the slope of the phase shift curves increases as the SMSW frequency $f$ increases. The curves of the phase shift $\Phi$ for an SMSW propagating in the field $H_g$ are truncated when the wave leaves the region of permissible values of the field $H_g$ determined using Eqs. (3) and (4). The curves for the field $H_g$ differ little from those for $H_0$ (the difference is $\approx 10\%$). For most of the trajectory the curves of the phase shift $\Phi$ for an SMSW in the field $H_g$ are lower than those for an SMSW in the field $H_0$. In the lower part of the frequency range for the existence of SMSWs at the end of the trajectory where the wave approaches the upper limit of the field $H_{gu}$, the curve for the SMSW in the field $H_g$ intersects that for the wave in the field $H_0$ and then continues slightly above this curve.

Figure 2 gives the phase shift $\Phi$ as a function of $y$ for SMSWs of various frequencies in ferrite–metal structures. As in a ferrite film, the SMSW trajectories are parabolic.[9] However, it follows from a comparison of Eqs. (4) and (5) that the range of permissible values of the field $H_g$ for SMSWs of constant frequency is considerably larger and the trajectory is 5–10 times longer. The higher the SMSW frequency $f$, the greater the slope of the phase shift curves $\Phi$. Unlike the SMSWs in a ferrite film, in ferrite–metal structures the SMSW does not reach the upper limit of the field $\Omega_{gu}$; in the plane of the ferrite film its trajectory asymptotically approaches the boundary corresponding to the field $\Omega_{gu}$ and parallel to the $y$ axis, and goes to infinity without terminating. The group velocity vector tends asymptotically in the direction of the $y$ axis, the phase velocity vector tends in the direction of the $z$ axis, and the angle $\varphi$ between them tends toward 90°. At $\vartheta = 90°$ the SMSW ceases to carry energy and its analysis becomes physically meaningless. Thus, in the calculations the trajectory $z(y)$ is bounded by the value of $z^*$ at which the angle is $\varphi = 89°$. On the sections of the trajectory approaching the upper limit of the field $\Omega_{gu}$ the curves of the phase shift $\Phi$ for an SMSW in the field $H_g$ differ substantially from those in the field $H_0$ (Fig. 2 and Ref. 4). In this case, the curves for an SMSW in the field $H_g$ are considerably higher than those in the field $H_0$ and would go to infinity if the trajectories were not bounded by the value of $z^*$. The higher the SMSW frequency, the greater the upward slope of these curves. The phase shift reaches tens of thousands of radians and for the same values of the coordinate $y$ is hundreds of times greater than the phase shift in a uniform field (see Refs. 4 and 10).

It has thus been shown that when SMSWs propagate in a ferrite–metal structure magnetized by a linearly nonuniform field the phase shift of the SMSW is many times greater than that in a ferrite film and also that in a ferrite–metal structure with a uniform field, and may reach extremely high values of tens of thousands of radians. This indicates that the development of microwave phase shifters using ferrite–metal structures magnetized by nonuniform fields holds great promise. By selecting the nonuniform field, it is possible to produce any type of curve $\Phi(y)$ that determines the desired tuning slope of the phase shifters.
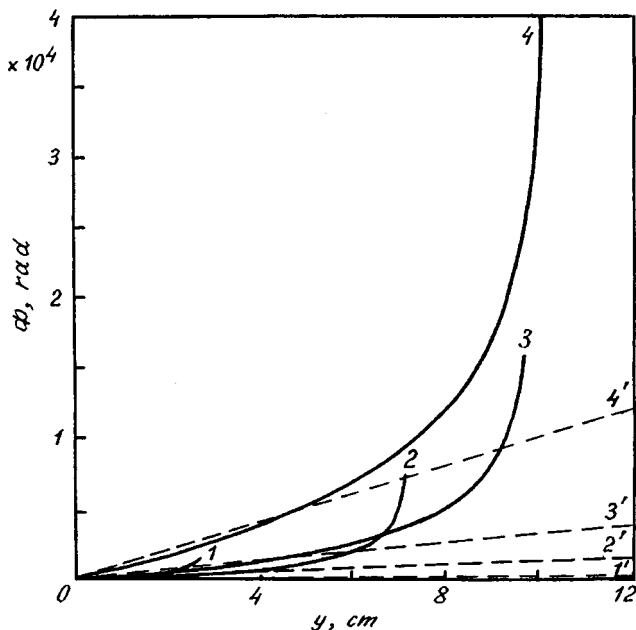


FIG. 2. Phase shift of SMSWs at various frequencies in a ferrite–metal structure. The solid curves are plotted for SMSWs in the field $H_g$ and the dashed curves in the field $H_0$. Curves: $1 — f = 2.8$ GHz, $2 — f = 3.6$ GHz, $3 — f = 4.4$ GHz, and $4 — f = 5.2$ GHz.

[1] W. S. Ishak, Proc. IEEE **76**, 171 (1988).

[2] A. V. Vashkovskiĭ, V. S. Stal'makhov, and Yu. P. Sharaevskiĭ, *Magnetostatic Waves in Microwave Electronics* [in Russian], Saratov State University Press, Saratov (1993), 312 pp.

[3] G. A. Vugal'ter and I. A. Gilinskiĭ, Izv. Vyssh. Uchebn. Zaved. Radiofiz. **32**, 1187 (1989).

[4] A. S. Bondarev and V. A. Khitrovskiĭ, Vestn. Kiev Politekhn. Univ. Radioélektron. No. 17, 26 (1980).

[5] F. R. Morgenthaler, Microwave J. **25**(2), 83 (1982).

[6] M. Tsutsumi, Y. Masaoka, F. Ohira, and N. Kumagai, IEEE Trans. Microwave Theory Tech. **29**, 583 (1981).

[7] A. V. Vashkovsky, V. I. Zubkov, E. H. Lock, and V. I. Shcheglov, IEEE Trans. Magn. **26**, 1480 (1990).

[8] A. V. Vashkovskiĭ, V. I. Zubkov, É. G. Lokk, and V. I. Shcheglov, Radiotekh. Elektron. **36**, 18 (1991).

[9] A. V. Vashkovskiĭ, V. I. Zubkov, É. G. Lokk, and V. I. Shcheglov, Zh. Tekh. Fiz. **65**(8), 78 (1995) [Tech. Phys. **40**, 790 (1995)].

[10] B. E. R. Hansson, S. Aditya, and M. A. Larsson, IEEE Trans. Microwave Theory Tech. **29**(3), 209 (1981).

Translated by R. M. Durham

# Influence of the electron density in a gallium arsenide film on the cutoff frequency for the amplification of space-charge waves in thin-film semiconductor structures

A. I. Mikhaĭlov and S. A. Sergeev

*N. G. Chernyshevskiĭ State University, Saratov*
(Submitted June 16, 1998)
Pis'ma Zh. Tekh. Fiz. **25**, 85–90 (February 26, 1999)

A theoretical analysis is made of the cutoff frequency for the amplification of space-charge waves in an $n$-GaAs thin-film semiconductor structure, taking into account the dependence of the drift velocity and the differential electron mobility on the electron density. It is shown that the dependence of the cutoff frequency on the electron density in the film has a maximum, which indicates that there is an optimum level of doping of the film for the fabrication of higher-frequency functional devices utilizing space-charge waves in $n$-GaAs. © *1999 American Institute of Physics.* [S1063-7850(99)03102-X]

Thin-film semiconductor structures with negative differential conductivity caused by interline electronic transitions in strong electric fields in semiconductors such as $n$-GaAs and $n$-InP are of major practical interest because they form of the basis of devices utilizing space-charge waves in semiconductors. These devices have extensive functional capabilities,[1] similar to those of acoustoelectronic devices, but unlike the latter they can operate effectively down to the millimeter range.

The choice of optimum electrophysical parameters and characteristics of the active layer of $n$-GaAs or $n$-InP semiconducting film is of particular importance for the practical design of functional devices using space-charge waves in semiconductors operating at frequencies close to the cutoff $f_c$ for the amplified waves. The most important of these electrophysical parameters is the electron density $n_0$, which is determined by the semiconductor doping level. It was established theoretically[2] that the cutoff frequency $f_c$ increases with increasing $n_0$ and for $n$-GaAs thin-film semiconductor structures reaches a maximum at $n_0 = (2-5) \times 10^{15}\,\text{cm}^{-3}$ before saturating. Quite clearly, as $n_0$ increases the drift velocity $v_0$ and the magnitude of the differential electron mobility $\mu_d$ should decrease as a result of intensified electron scattering at ionized impurities and interelectron scattering. Existing experimental and theoretical data confirm this.[4–7] However, the dependence of $v_0$ and $\mu_d$ on the electron density $n_0$ was neglected when determining $f_c$ in Ref. 2, although it was noted when analyzing the results that allowance for these could give rise to a maximum on the dependence of $f_c$ on $n_0$ instead of the saturation section obtained.

Here we report results of a theoretical analysis of the influence of the electron density $n_0$ in an $n$-GaAs film on the cutoff frequency for the amplification of space-charge waves in thin-film semiconductor structures with negative differential conductivity, allowing for the dependence of the electron drift velocity $v_0$ and the differential mobility $\mu_d$ on $n_0$.

For the theoretical analysis we shall use the model described in detail in Ref. 2, so we shall only briefly recall its main features. A highly asymmetric thin-film semiconduct-

ing structure is considered:[3] the permittivity of the insulator layer on which the $n$-GaAs film is grown (in real structures the substrate is a semiinsulating $n$-GaAs layer) is appreciably higher than that of the insulator bounding the other surface of the film (in practice this is air). We also adopt the most widely used model of a rigid carrier flux boundary which coincides with the real physical boundary of the semiconductor film.

If a strong static electric field, whose strength $E_0$ corresponds to the descending section on the $E_0$ dependence of $v_0$ for $n$-GaAs, is created in the film parallel to its plane, quasistatic space-charge waves may be excited in the film. These will be amplified or damped as they propagate, depending on the frequency. The propagation constant of the space-charge waves and the cutoff frequency for their amplification were determined by solving the dispersion equation for the thin-film semiconductor structure described. The method of solution and the algorithm are described in detail in Refs. 2 and 3. Unlike in Ref. 2, the calculations allowed for the dependence of $v_0$ and $\mu_d$ on $n_0$ in the form of analytic approximations obtained using experimental and theoretical data from Refs. 4 and 5, as well as from books.[6,7] The values of $\mu_d$ were determined using the static dependence of $v_0$ on $E_0$ given in Refs. 4–7 for $E_0 = 5.5\,\text{kV/cm}$, and thus the low-frequency differential mobility is taken as $\mu_d$. That is, unlike Ref. 2, we neglected the frequency dispersion of $\mu_d$ in order to study the influence of the electron density on $f_c$. We also note that the values of $\mu_d$ and $v_0$ for the low densities $n_0$ used here differ negligibly from those used in Ref. 2, since the specific characteristics of $n$-GaAs were taken from data obtained in other studies which contain the dependence on $n_0$ required for the investigation. All the other parameters of $n$-GaAs were the same as those in Ref. 2.

In Fig. 1 the data from Refs. 4–7 are shown by the symbols (*1*—Refs. 4 and 6 and *2*—Refs. 5 and 7) and the approximating dependences are given by the curves. The analytic expressions corresponding to the dependence of $v_0$ and $\mu_d$ on $n_0$ plotted in Fig. 1 have the form

$$v_0 = a_0 + a_1(\log n_0) + a_2(\log n_0)^2 + a_3(\log n_0)^3, \qquad (1)$$
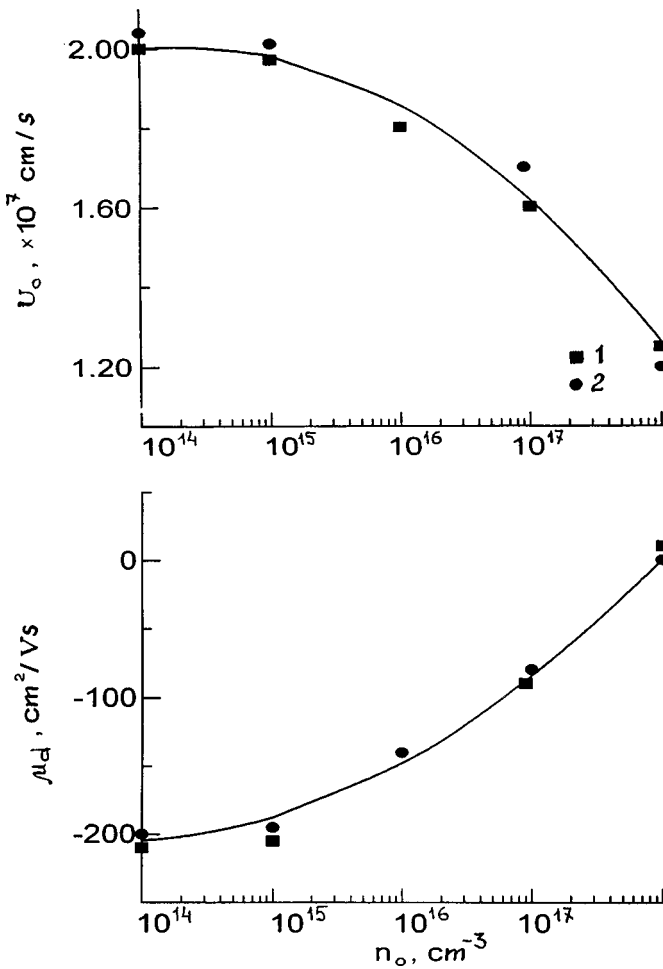
FIG. 1.



FIG. 2.

$$\mu_d = b_0 + b_1(\log n_0) + b_2(\log n_0)^2, \qquad (2)$$

where $v_0$ is in meters per second, $\mu_d$ is meters squared per volt-second, $n_0$ is in reciprocal cubic meters, and $a_0$, $a_1$, $a_2$, $a_3$, $b_0$, $b_1$, and $b_2$ are the parameters of the corresponding approximations: $a_0 = -1.9328 \times 10^{-6}$, $a_1 = 1.9946 \times 10^5$, $a_2 = -4164$, $a_3 = -23.872$, $b_0 = 5.4971$, $b_1 = -0.5662$, and $b_2 = 0.01406$.

During the calculations we checked that the following condition was satisfied

$$n_0 d = \frac{v_0}{v_{00}} \frac{\mu_{d0}}{\mu_d} 2 \times 10^{14} \, \mathrm{m}^{-2}, \qquad (3)$$

where $d$ is the thickness of the $n$-GaAs film, and $v_{00} = 2 \times 10^5$ m/s and $\mu_{d0} = -0.2 \, \mathrm{m}^2/\mathrm{V} \cdot \mathrm{s}$ are the drift velocity and the differential electron mobility in the field $E_0 = 5.5$ kV/cm for the electron density in the film $n_0 = 10^{14} \, \mathrm{cm}^{-3}$. It is acknowledged that condition (3) ensures the electrical stability of thin-film semiconducting structures, dictated by the need to prevent the onset of absolute instability, which is not permissible for space-charge wave devices and is observed as the formation of traveling Gunn domains. The stability criterion (3) used here differs from that used in Ref. 2, since it contains the factor $(v_0/v_{00}) \times (\mu_{d0}/\mu_d)$ which is introduced to allow for the variation of $v_0$ and $\mu_d$ with varying $n_0$.
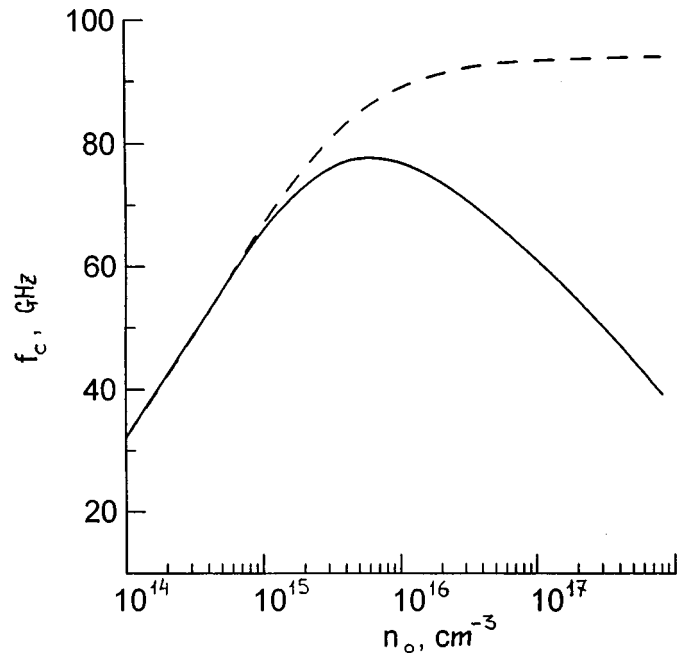
The results of calculations of the cutoff frequency $f_c$ for the dominant trigonometric space-charge wave mode are plotted in Fig. 2. The dashed curve gives the dependence of $f_c$ on $n_0$ obtained neglecting the dependence of $v_0$ and $\mu_d$ on $n_0$, and the solid curve gives the same dependence allowing for these. It can be seen that the dashed curve is the same as that from Ref. 2, whereas the solid curve has a maximum when $n_0$ is approximately $(5-6) \times 10^{15} \, \mathrm{cm}^{-3}$, which confirms the assumption made in Ref. 2. A comparison between these results and the data given in Ref. 2 suggests that when allowance is made for the frequency dispersion of the differential electron mobility, the maximum cutoff frequency of the amplified space-charge waves will be achieved when the electron density in the $n$-GaAs film is approximately $(1-2) \times 10^{15} \, \mathrm{cm}^{-3}$. This value may be considered to be the maximum dopant concentration in the semiconductor film for the fabrication of thin-film superconducting structures for higher-frequency devices using space-charge waves in $n$-GaAs. An analysis of the results of Ref. 2 also indicates that for $n$-InP the maximum concentration should be approximately the same as for $n$-GaAs.

[1] A. A. Barybin, I. B. Vendik, O. G. Vendik *et al.*, Mikroélektronika **8**(1), 3 (1979).
[2] A. I. Mikhaĭlov, Pis'ma Zh. Tekh. Fiz. **21**(21), 89 (1995) [Tech. Phys. Lett. **21**, 902 (1995)].
[3] A. A. Barybin, *Waves in Thin-Film Semiconductor Structures with Hot Electrons* [in Russian], Nauka, Moscow (1986), 288 pp.
[4] W. T. Masselink and T. F. Kuech, J. Electron. Mater. **18**, 579 (1989).
[5] K. Kliefoth and B. Petzel, Phys. Status Solidi A **42**, K133 (1977).
[6] M. E. Levinshteĭn, I. K. Pozhela, and M. S. Shur, *The Gunn Effect* [in Russian], Sovet-skoe Radio, Moscow (1975), 288 pp.
[7] M. S. Shur, *Gallium Arsenide Devices and Circuits* (Plenum Press, New York, 1987; Mir, Moscow, 1991, 632 pp.).

Translated by R. M. Durham

# Nonequilibrium phase transitions induced by external noise in distributed systems

Yu. V. Gudyma

*Chernovtsy State University*
(Submitted August 8, 1998)
Pis'ma Zh. Tekh. Fiz. **25**, 91–95 (February 26, 1999)

A formalism is proposed to describe nonequilibrium phase transitions induced by external multiplicative noise in distributed systems. This approach can reduce the problem to an investigation of a regular differential equation whose roots correspond to possible phase states in the system. By means of this theory the relative probability of the existence of one state can be compared with another and the number of possible states identified, and the genesis of the system under the action of fluctuations of the external medium can be traced. © *1999 American Institute of Physics.* [S1063-7850(99)03202-4]

The theory of self-organizing systems is successful mainly because thermodynamically nonequilibrium systems in a steady state with detailed equilibrium differ formally from equilibrium systems for which mathematical tools of analysis are well-developed.[1,2] The kinetics of the phase transitions of these systems is described by the Landau–Khalatnikov equation with additive noise, which describes the relaxation of the phase variable to a new, energetically more favorable state:

$$\frac{\partial U}{\partial t} = -\hat{\Gamma}\frac{\delta S[U]}{\delta U} + \xi(\mathbf{r},t), \tag{1}$$

where $\hat{\Gamma}$ is generally an operator and the term $\xi(\mathbf{r},t)$ is stochastic (fluctuational). The deterministic term implies a thermodynamic force defined in accordance with the general approach as a functional derivative of the functional of the generalized thermodynamic potential with respect to the local value of the variable being studied. It is easy to show that the probability density of the distribution of this quantity for the steady state has the form of an exponential function of the generalized thermodynamic potential (i.e., it is irrotational).[3,4]

However, additive external and internal noise does not lead to induced transitions. At the same time, it is known that in highly nonequilibrium open systems, external multiplicative noise can not only induce a relaxation process between two existing phase states but can also result in the appearance of new steady states, as well as nonequilibrium phase transitions induced by the external noise.[5] These problems cannot be investigated within the limits of Eq. (1).

The theory of nonequilibrium phase transitions induced by external noise has only been developed fairly comprehensively for point phenomenological equations of the evolution type,[6]

$$\frac{\partial U}{\partial t} = f(\beta_t, U), \tag{2}$$

where $\beta_t$ is an external parameter which depends on the state of the medium. For systems of the form (2) where the function $f(\beta_t, U)$ is linear with respect to the external parameter (a case covering a wide range of applications), i.e.,

$$f(\beta_t, U) = h(U) + \beta_t g(U), \tag{3}$$

where $\beta_t$ is a steady-state random process $\beta_t = \beta + \sigma\xi(t)$ and $\xi(t)$ is a steady-state centered normal white-noise process, Eq. (3) can be compared with the Fokker–Planck equation having a steady-state potential solution.

We shall analyze a generalization of Eqs. (2) and (3) of the form

$$\frac{\partial U}{\partial t} = \hat{N}U + \sigma g(U)\xi(t), \tag{4}$$

where $\hat{N}$ is an operator which includes a distributed component. The probability density of achieving $U$ is

$$P(U,t) = \langle \delta(\hat{N}U + \sigma g(U)\xi(t)) \rangle. \tag{5}$$

For a nonsteady-state problem, averaging implies averaging over the external forces $\xi(t)$ and the initial field $U(t=0)$. In fact, we are studying that steady-state regime which is established under the action of temporally steady-state external forces if for $t \to -\infty$ we have $U(t \to -\infty) = 0$.

Using an integral representation of the $\delta$-function and assuming that $\xi(t)$ has a Gaussian white noise distribution, we transform Eq. (5) to give

$$P(U,t) = \int_{-i\infty}^{+i\infty} \frac{dV}{2\pi i}$$
$$\times \exp\left(-\int\left(V\hat{N}U - \frac{1}{2}[V\sigma g(U)]^2\right)dt\right). \tag{6}$$

The probability density of $\tilde{U}(t=0)$ being transferred to the state $\bar{U}(t=\tau)$ is

$$P(\bar{U},\tau,\tilde{U},0) = \int_{\tilde{U}}^{\bar{U}} D[U] \int_{-i\infty}^{+i\infty} \frac{dV}{2\pi i}$$
$$\times \exp\left(-\int_0^\tau\left(V\hat{N}U - \frac{1}{2}[V\sigma g(U)]^2\right)dt\right). \tag{7}$$

The continuous integral (7) is taken over all paths $[U]$ $=\{U(t)\}$ leading from the initial point to the final one. It also follows from expression (7) that the maxima and minima of the transition probability are completely determined by the variational principle

$$\delta S = \delta \int_0^\tau \left( V\hat{N}U - \frac{1}{2}[V\sigma g(U)]^2 \right) dt$$

$$= \delta \int_0^\tau L(V,U)dt = 0. \tag{8}$$

Thus, each system of functions $(V,U)$ realizing a maximum or minimum (7) should satisfy a system of Euler equations. If we are not interested in changes in the additional field $V$ introduced by us, the problem is simplified substantially and reduces to the single equation

$$\frac{\partial}{\partial U}(\hat{N}U) - \sigma^2 g^2(U)\frac{\partial}{\partial U}(\ln g(U)) = 0, \tag{9}$$

which may be given a slightly different (potential) form

$$\frac{\partial}{\partial U}\left\{ \int^U \frac{\hat{N}U}{g^2(U)}dU - \sigma^2 \ln g(U) \right\} = \frac{\partial}{\partial U}\Phi(U) = 0. \tag{10}$$

The potential maxima $\Phi(U)$ correspond to stable steady states and the minima correspond to unstable steady states. This implies that if the steady-state probability density has only one maximum, the system fluctuates around a single macroscopic state, i.e., exists in one phase. If the steady-state probability density has two or more maxima, the system may exist in two phases for the same external conditions. The investigation of the potential $\Phi(U)$ is reduced to the phase transition problem, described by a partial differential equation for which methods of analysis are well-developed.[7,8]

As an example, we shall analyze the behavior of a system described by the so-called reaction–diffusion equation

$$\frac{\partial U}{\partial t} = \Delta U + h(U) + \beta g(U) + \sigma g(U)\xi(t), \tag{11}$$

typical of self-organization phenomena.[1,2] The scheme put forward above yields an equation to analyze the action of high-speed external noise on the steady-state behavior of systems of the form (11):

$$\Delta U + h(U) + \beta g(U) - \sigma g(U)g'(U) = 0. \tag{12}$$

The last term in this expression maps the action of the external noise and may give rise to additional phase transition points not found in the completely deterministic case. However, the observation of these transitions is by no means trivial. First, the probability peaks of these states are fairly broadened because of noise. Second, they are masked by diffusion terms.

This theory cannot be used to calculate the probability density of a particular phase state because the integral (7) is only determined formally. However, this formalism can identify the relative probability of the existence of one state compared with another, the number of possible states, and can also trace the genesis of the system under the action of external multiplicative noise.

A different approach to going outside the limits of Eq. (1) in the theory of nonequilibrium phase transitions is described in Ref. 9. In this study perturbation theory is applied systematically, which imposes well known constraints on the results.

[1] G. Nicolis and I. Prigogine, *Self-Organization in Nonequilibrium Systems* (Wiley, New York, 1977; Mir, Moscow, 1979, 512 pp.).

[2] H. Haken, *Advanced Synergetics* (Springer Verlag, Berlin, 1983; Mir, Moscow, 1985, 423 pp.).

[3] U. C. Tauber and F. Schwabl, Phys. Rev. B **48**, 186 (1993).

[4] A. I. Olemskoĭ, Usp. Fiz. Nauk **168**(3), 287 (1998).

[5] W. Horsthemke and R. Lefever, *Noise-Induced Transitions* (Springer Verlag, Berlin, 1984; Mir, Moscow, 1987, 400 pp.).

[6] P. S. Landa and A. A. Zaikin, Zh. Éksp. Teor. Fiz. **111**, 358 (1997) [JETP **84**, 197 (1997)].

[7] Yu. E. Kuzovlev, T. K. Soboleva, and A. É. Fillipov, Zh. Éksp. Teor. Fiz. **103**, 1742 (1993) [JETP **76**, 858 (1993)].

[8] L. A. Maksimov, A. I. Ryazanov, and V. L. Tsymbalenko, Zh. Éksp. Teor. Fiz. **110**, 371 (1996) [JETP **83**, 199 (1996)].

[9] G. F. Mazenko, Cond.-mat. N 9803029 (1998).

Translated by R. M. Durham

# Inverse problem in the x-ray phase contrast method

V. A. Bushuev and A. A. Sergeev

*M. V. Lomonosov State University, Moscow*
(Submitted July 6, 1998)
Pis'ma Zh. Tekh. Fiz. **25**, 1–7 (February 12, 1999)

An analysis is made of the possibility of solving the inverse problem of reconstructing the internal structure of an object using a set of experimental distributions measured in an x-ray beam for various orientations of the object. © *1999 American Institute of Physics.*
[S1063-7850(99)00102-0]

The x-ray phase contrast method, based on the refraction of x-rays, is intended to obtain the image of weakly absorbing noncrystalline objects.[1–3] Radiation passing through an object is deflected from its initial direction through various angles $\beta(x)$ and is then incident on a single-crystal analyzer mounted near the Bragg reflection region. Since the refractive index $n(x,z) = 1 - \delta(x,z)$ is very close to unity ($\delta \sim 10^{-6}$) for radiation of wavelength $\lambda \leq 1$Å, the angles of refraction $\beta \sim \delta$ are between fractions and a few seconds of arc. Nevertheless, such small deflections may produce an image of fairly high contrast on photographic film inserted in the beam reflected from the analyzer. This is because the angular width of the diffraction reflection curves is comparable with $\beta(x)$.

The phase contrast method can improve the contrast of an image by several orders of magnitude compared with the adsorption methods normally used. This is particularly important for studying the internal structure of medical and biological objects[3–6] in which the absorption coefficient $\mu(x,z)$ in different parts of the object changes by only a few percent.

So far, only the direct problem has been analyzed in the theory of the phase contrast method, i.e., the image [the diffraction reflection intensity $I(x)$] has been calculated using given distributions $\delta(x,z)$ and $\mu(x,z)$ (Refs. 7–10). Here for the first time we consider the possibility of solving the inverse problem of reconstructing the internal structure of an object using a set of experimental distributions $I(x)$ measured for various orientations of the object in the x-ray beam. We show that for fairly large objects for which the geometric-optics approximation is valid, a two-dimensional distribution $\delta(x,z)$ can be uniquely reconstructed using a complete set of $I(x)$ data.

The intensity distribution in the diffracted beam is given by the following integral relation:[9,11,12]

$$I(x) = \left| \int_0^\infty G(\xi) A(x/\gamma_0 - \xi) \exp(ik\gamma_0 \Delta\theta\xi) d\xi \right|^2, \qquad (1)$$

where $A(x) = \exp(-\sigma + i\Phi)$ is the amplitude of the wave passing through the object,

$$\sigma(x) = 0.5 \int_{-\infty}^\infty \mu(x,z) dz, \quad \Phi(x) = -k \int_{-\infty}^\infty \delta(x,z) dz,$$

$$G(\xi) = (k\gamma_0/2\pi) \int_{-\infty}^\infty R(\alpha) \exp(-ik\gamma_0\alpha\xi) d\alpha.$$

Here $\Phi(x)$ is the change in the phase of a wave propagating along the $z$ axis, $k = 2\pi/\lambda$, $G(\xi)$ is the Green's function of the Bragg diffraction problem for bounded wave packets,[11] $R(\alpha)$ is the amplitude reflection coefficient of a plane wave incident on a single crystal with angular deviation $\alpha$ from the Bragg angle $\theta_B$, $\Delta\theta$ is the fixed angle of rotation of the analyzer, $\gamma_0 = \sin(\theta_B + \psi)$, and $\psi$ is the angle of inclination of the reflecting planes to the surface of the analyzer. The dependence of the phase $\Phi(x)$ on the transverse coordinate leads to refraction at the angles $\beta(x) = (1/k) d\Phi(x)/dx$.

The characteristics $\mu$ and $\delta$ of the object enter in a fairly complicated way in the integral (1) and thus are generally difficult to reconstruct using the measured intensity $I(x)$. The situation is simplified appreciably if the geometric-optics approximation of the Bragg diffraction problem is satisfied. In this case, we can show[9,12] that

$$I(x) = I_a(x) P(\Delta\theta - \beta), \qquad (2)$$

where $I_a(x) = \exp[-2\sigma(x)]$ is the intensity of the absorption image and $P(\alpha) = |R(\alpha)|^2$ is the diffraction reflection curve from the analyzer. Equation (2) holds if the transverse dimension of the object is $r \gg \Delta\xi = \lambda/\pi\gamma_0\Delta\theta_B$ and the refraction angle gradient is $d\beta/dx \ll \Delta\theta_B/\Delta\xi$, where $\Delta\theta_B = 2C|\chi_h|/b^{1/2}\sin 2\theta_B$ is the width of the diffraction reflection curve, $C$ is the polarization factor, $\chi_h$ is the Fourier component of the crystal polarizability, $b = \gamma_0/\gamma_h$, and $\gamma_h = \sin(\theta_B - \psi)$. Typical values of $\Delta\xi$ are 5–30 $\mu$m. In this approximation the image (2) is determined by the intensity of the local (at the point $x$) reflection of an x-ray incident on the analyzer with the angular deviation $\Delta\theta - \beta(x)$.

The solution of the inverse problem can be divided into three stages: 1) determining the refraction angles $\beta(x)$ using the measured intensity $I(x)$; 2) calculating the function $F(x,z) = -\partial\delta(x,z)/\partial x$ in the linear integral

$$\beta(x) = \int_{-\infty}^\infty F(x,z) dz; \qquad (3)$$

and 3) reconstructing the required distribution $\delta(x,z)$ from the function $F(x,z)$.

In the first stage we utilize the fact that silicon crystals with a known structure are used as the analyzer. Thus, we
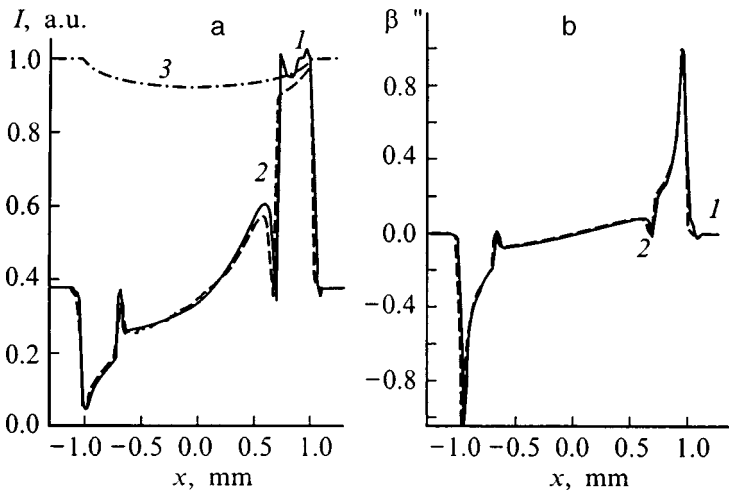
FIG. 1. Comparison between the results of solving the inverse problem of reconstructing the refraction angles $\beta(x)$ and the direct calculations. Image intensities (a): $1$ — accurate solution, $2$ — geometric optics approximation, $3$ — absorption image; distributions $\beta(x)$ (b): $1$ — solution of the inverse problem, $2$ — direct calculations. Parameters used: $AgK_\alpha$ radiation, $Si(220)$ symmetric reflection, $\Delta\theta_B = 1.7''$, $\Delta\theta = 0.95''$.

can assume that both the amplitude and the phase of the reflection $R = |R|\exp(i\eta)$ are known. Finally, we find that the refraction angles $\beta(x)$ are related as follows to the experimentally measured function $J(x) = I(x)/I_a(x)$:

$$\beta(x) = \Delta\theta - [2Y(x)C\chi_h b^{1/2} - i\chi_{0i}(1+b)]/2b \sin 2\theta_B, \quad (4)$$

where

$$Y(x) = [1 + J(x)\exp(i2\eta)]/[2J^{1/2}(x)\exp(i\eta)].$$

To illustrate the validity of this reconstruction, Fig. 1 gives the results of a numerical experiment to solve the direct and inverse problems of finding the refraction angles $\beta(x)$. The object was a $(C_8H_8)_n$ polystyrene capillary of radius 1 mm and wall thickness 0.3 mm, filled with ethyl alcohol $C_2H_6O$. The coefficients $\delta$ and $\mu$ at $\lambda = 0.559$ Å are $0.477 \times 10^{-6}$ and $0.38 \, cm^{-1}$ for polystyrene and $0.376 \times 10^{-6}$ and $0.37 \, cm^{-1}$ for alcohol (Ref. 7). The thickness of the transition layer at both interfaces is taken to be $10 \, \mu m$. Figure 1a gives the results of direct calculations of the phase contrast intensity $I(x)$ using the rigorous wave theory (1) (curve $1$) and the geometric-optics approximation (2) (curve $2$). Also plotted for comparison is the absorption image curve $3$. It can be seen that the absorption contrast is only 5%, which is much lower than the contrast for curves $1$ and $2$. Moreover, unlike the phase contrast images $1$ and $2$, the alcohol–polyethylene interface cannot be identified on curve $3$. The result of the accurate calculations (curve $1$) was then used as the experimentally measured distribution $I(x)$ from which the function $\beta(x)$ given by Eq. (4) was determined. It can be seen from Fig. 1b that the results of this reconstruction of the refraction angles $\beta(x)$ (curve $1$) differ negligibly from the function $\beta(x)$ calculated directly from the given distributions $\delta(x,z)$ and $\mu(x,z)$ (curve $2$). It should be noted that the results of solving the inverse problem for $\beta(x)$ do not depend on the deviation angle $\Delta\theta$ of the analyzer.

In the second stage we first calculate the Fourier transform $\beta(k)$ of $\beta(x)$ determined above:

$$\beta(k) = \int_{-\infty}^{\infty} \beta(x)\exp(-ikx)dx. \quad (5)$$

Note that in general the functions $\Phi(x)$ and $\beta(x)$ also depend on the angle of rotation $\varphi$ of the coordinate system $(x', z')$ rigidly bound to the object relative to the laboratory system $(x,z)$. The equation for the path along which integration is performed when calculating $\Phi$ in Eq. (1) then has the form $x = x'\cos\varphi + z'\sin\varphi$. The function $\beta(k,\varphi)$ is the two-dimensional Fourier transform of the function $F(x,z)$ in Eq. (3). The function $S(x,\varphi)$ is then calculated according to the following rule:

$$S(x,\varphi) = (1/4\pi^2)\int_{-\infty}^{\infty} \beta(k,\varphi)|k|\exp(ikx)\cos\varphi dk. \quad (6)$$

We can easily show that the function $F(x,z)$ in the integral (3) can be determined by integrating $S(x,\varphi)$ (6) over all angles $\varphi$ between 0 and $\pi$:

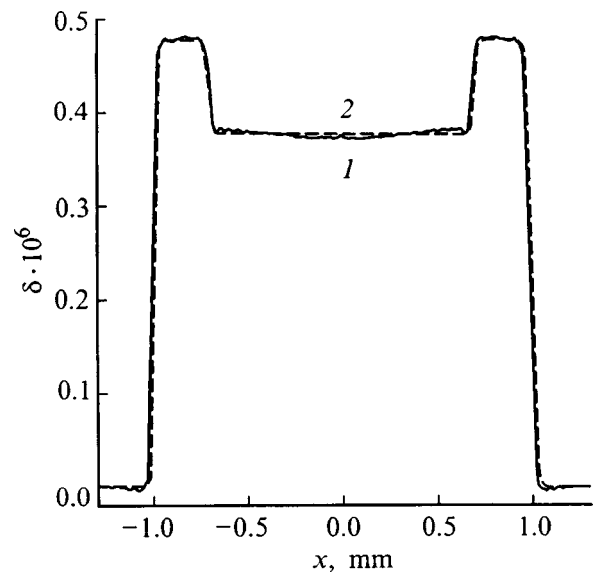$$F(x',z') = \int_0^\pi S(x'\cos\varphi + z'\sin\varphi, \varphi)d\varphi.$$



FIG. 2. Distributions of the capillary refraction decrement $\delta(x,0)$: $1$ — result of solving the inverse problem, $2$ — initial model distribution.

The third final stage involves accurately reconstructing the required two-dimensional distribution:

$$\delta(x,z) = -\int_{-\infty}^{x} F(x',z)dx'. \tag{7}$$

In Fig. 2 the solid curve *1* shows the distribution $\delta(x,0)$ reconstructed using Eqs. (5)–(7), where curve *1* in Fig. 1b was taken as $\beta(x)$. The dashed curve *2* gives the initial model distribution in the capillary cross section $z=0$. It can be seen that the agreement is fairly good. Small discrepancies arise because in the immediate vicinity of the capillary boundaries the geometric-optics approximation (2) for $I(x)$ differs from the accurate result (1).

Thus, we have found that the internal structure of an object $\delta(x,z)$ can be accurately reconstructed for a complete set of data $I(x,\varphi)$. In practice, the function $I(x,\varphi)$ is only known for a finite number of points $x$ and $\varphi$, so that more complicated algorithms[13] developed in computer tomography are required to reconstruct images using bounded data.

[1] V. N. Ingal and E. A. Beliaevskaya, J. Phys. D **28**, 2314 (1995).

[2] T. J. Davis, T. E. Gureyev, D. Gao *et al.*, Phys. Rev. Lett. **74**, 3173 (1995).

[3] V. N. Ingal and E. A. Belyaevskaya, Zh. Tekh. Fiz. **67**(1), 68 (1997) [Tech. Phys. **42**, 59 (1997)].

[4] V. N. Ingal and E. A. Beliaevskaya, Physica Medica **12**(2), 75 (1996).

[5] V. N. Ingal and E. A. Beliaevskaya, Surface Invest. **12**, 441 (1997).

[6] V. N. Ingal and E. A. Beliaevskaya, Nuovo Cimento D **19**, 553 (1997).

[7] V. A. Bushuev, V. N. Ingal, and E. A. Belyaevskaya, Kristallografiya **41**, 808 (1996) [Crystallogr. Rep. **41**, 766 (1996)].

[8] V. A. Bushuev, E. A. Beliaevskaya, and V. N. Ingal, Nuovo Cimento D **19**, 513 (1997).

[9] V. A. Bushuev, V. N. Ingal, and E. A. Belyaevskaya, Kristallografiya **43**(4), 630 (1998) [*sic*].

[10] V. A. Bushuev and A. Kone, Surface Invest. **13**, No. 10 (1998).

[11] A. M. Afanas'ev and V. G. Kohn, Acta Crystallogr., Sect. A: Cryst. Phys., Diffr., Theor. Gen. Crystallogr. **27**, 421 (1971).

[12] T. E. Gureyev and S. W. Wilkins, Nuovo Cimento D **19**, 545 (1997).

[13] B. Swindel and S. Webb, in: *The Physics of Medical Imaging*, Vol. 1, edited by S. Webb (Adam Hilger, Philadelphia, 1988), p. 138.

Translated by R. M. Durham

# Angular dependence of the current–voltage characteristics and voltage fluctuation spectrum in ceramic superconductors

O. V. Gerashchenko

*B. P. Konstantinov Institute of Nuclear Physics, Russian Academy of Sciences, St. Petersburg*
(Submitted April 24, 1998; resubmitted September 12, 1998)
Pis'ma Zh. Tekh. Fiz. **25**, 8–13 (February 12, 1999)

Measurements were made of the current–voltage characteristics and voltage fluctuation spectrum as functions of the angle between the magnetic field applied in the plane of the sample and the direction of the transport current in a $YBa_2Cu_3O_{7-\delta}$ ceramic superconductor. The angular dependence of the fluctuation spectrum was measured first. It is shown that the current–voltage characteristics are not described using the vortex line cutting model and the voltage fluctuations are not caused by independent motion of vortices in the bulk of the sample. The results are consistent with the model of a self-organized critical state. © *1999 American Institute of Physics.* [S1063-7850(99)00202-5]

It is known that in low-field electrodynamics (when the magnetic field does not penetrate into the granules) granular high-temperature superconductors are rigid type-II superconductors, provided that the effective Josephson penetration depth satisfies the condition $\lambda_{eff} = (\Phi_0/2\pi\mu_0\mu_{eff}j_c a)^{1/2} \gg a$, where $a$ is the characteristic size of the granules and pores in the ceramic, $\Phi_0$ is the magnetic flux quantum, and $j_c$ is the critical current density. The current–voltage characteristic is then formulated as the double critical-state model (see, for example, Ref. 1) in which four phenomenological parameters are introduced: the transverse critical current density $j_{c\perp}$ which determines the depinning threshold, the longitudinal critical current density $j_{c\parallel}$, which gives the threshold for vortex line cutting, and also the longitudinal and transverse resistivities $\rho_\parallel$ and $\rho_\perp$. The current–voltage characteristic is highly anisotropic relative to the direction of the magnetic field.

We assume

$$\mathbf{j} = j\mathbf{e_z} = j_\parallel\mathbf{n} + j_\perp\mathbf{m}, \quad \mathbf{B} = B\mathbf{n}, \quad \mathbf{E} = E_\parallel\mathbf{n} + E_\perp\mathbf{m},$$

$$\mathbf{n} = \mathbf{e_z}\cos\alpha + \mathbf{e_y}\sin\alpha, \quad \mathbf{m} = \mathbf{n}\times\mathbf{e_x} = \mathbf{e_y}\cos\alpha - \mathbf{e_z}\sin\alpha. \tag{1}$$

Then for the electric field component $E_z(\alpha)$ we find

$$E_z = E_\parallel\cos\alpha - E_\perp\sin\alpha, \tag{2}$$

$$E_\parallel = \begin{cases} 0, & |j\cos\alpha| < j_{c\parallel} \\ \rho_\parallel(j\cos\alpha - j_{c\parallel}\,\text{sign}(j\cos\alpha)), & |j\cos\alpha| > j_{c\parallel} \end{cases}$$

$$E_\perp = \begin{cases} 0, & |j\sin\alpha| < j_{c\perp} \\ -\rho_\perp(j\sin\alpha - j_{c\perp}\,\text{sign}(j\sin\alpha)), & |j\sin\alpha| > j_{c\perp}. \end{cases}$$

It was shown in Ref. 2 that the condition for validity of the continuum approximation $\lambda_{eff} \gg a$ is equivalent to the condition

$$\beta = a^2/\lambda_{eff}^2 \ll 1. \tag{3}$$

The parameter $\beta$ is proportional to the number of flux quanta $\Phi_0$ pinned by the elementary circuit. For typical values in high-temperature superconductors $j_c = 10^6$ A/m², $a = 10^{-5}$ m, and $\mu_{eff} = 0.5$ we obtain $\beta \approx 2$, i.e., criterion (3) cannot be satisfied.

In the limit $\beta \gg 1$ the Josephson medium is described by equations in which discreteness is very important.[2] These equations are equivalent to those for a system with self-organized criticality.[3] This case corresponds to the model of an isotropic current–voltage characteristic proposed by Bean[4] and the model of a self-organized critical state developed for ceramic superconductors in Refs. 2, 5, and 6. In this model, the local current–voltage characteristic is isotropic:

$$\mathbf{E} = E_0\mathbf{j}/|\mathbf{j}|,$$

$$E_0(j) = \begin{cases} 0, & |j| < j_c \\ \rho(j - j_c\,\text{sign}\,j), & |j| > j_c. \end{cases} \tag{4}$$

These two cases ($\beta \ll 1$ and $\beta \gg 1$) can be distinguished by measuring the current–voltage characteristic versus the angle $\alpha$ between the current and the magnetic field,[5] or by studying the fluctuation spectra, since self-organized systems are strongly fluctuating.

Unfortunately, no detailed noise theory has yet been developed, although it may be predicted that the noise correlation functions should differ substantially for the anisotropic ($\beta \ll 1$) and isotropic ($\beta \gg 1$) current–voltage characteristic. Nevertheless, it is interesting to compare our results with those predicted by a simple model corresponding to $\beta \ll 1$ in which the voltage fluctuations occur in a superconductor as a result of the independent motion of vortices under the action of the Lorentz force through the sample (see Ref. 7, for example). Then, in the low-frequency limit we obtain an expression for the fluctuation spectrum similar to the shot noise spectrum:

$$S_V(f \ll f_c) = 2\Phi_0 V_z = 2\Phi_0 E_z d, \tag{5}$$

where $f_c = 1/(2\pi\tau)$, $\tau = wdB/V_z$ is the time a vortex takes to pass through the sample, $w$ is the sample thickness, $d$ is the
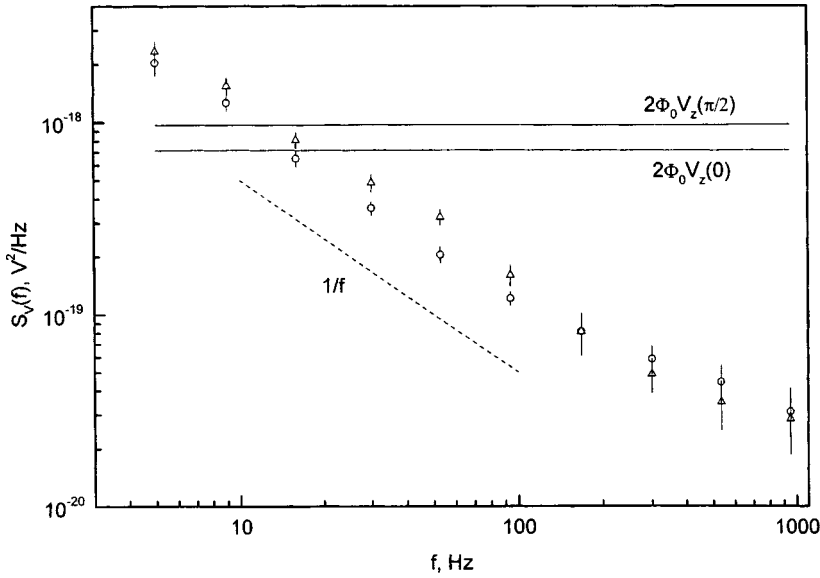
FIG. 1. Spectral density of voltage fluctuations for $|\mathbf{B}_0| = 3.6$ mT and $j = 1.13$ A/cm$^2$, $\alpha = 0 (\bigcirc)$, and $\alpha = \pi/2 (\triangle)$.

distance between the potential contacts, $B$ is the magnetic induction, and $V_z$ is the average voltage at the potential contacts.

Measurements were made of the current–voltage characteristic $E_z(j)$ and the voltage fluctuation spectrum $S_V(f)$ for samples of YBa$_2$Cu$_3$O$_{7-\delta}$ high-temperature superconducting ceramic ($T_c = 91.5$ K) fabricated in the form of thin platelets having dimensions of $15 \times 4 \times 0.3$ mm along the $z$, $y$, and $x$ axes, respectively. The measurements were made at liquid-nitrogen temperature using a four-contact method. The sample was placed in an electromagnetic shield and cooled at $B_0 = 0$. The magnetic field $\mathbf{B}_0$ was generated parallel to the broad plane of the sample ($y,z$) by means of permanent magnets which could be rotated about the $x$ axis perpendicular to this plane. The electric current, obtained from batteries via a limiting resistor, was directed along the $z$ axis. The magnitude of this current was such that the corresponding voltage drop $V_z$ was in the linear region of the current–voltage characteristic (flux flow regime).

The voltage $V_z(t)$ from the potential contacts was passed through a matching step-up transformer to a low-noise amplifier, a low-pass filter with a cutoff frequency of 3 kHz, and an L-1230 data acquisition array. The voltage fluctuation spectrum was calculated numerically using a fast Fourier transformation. The value of $S_V(f)$ was obtained by averaging the measured spectrum over 50 realizations and subtracting the noise of the device in the absence of current through the sample. The measurement error for $S_V(f)$ was approximately $10^{-20}$ V$^2$/Hz and increased slightly at low $f$.

Since in this experimental setup, possible fluctuations in the resistance of the limiting resistor and the current contacts may cause current fluctuations which are converted into voltage fluctuations at the sample resistance, the effect of this was estimated by making measurements of the voltage fluctuations at a 1 $\Omega$ wire-wound resistance connected in series with the sample. It was found that the current fluctuations were negligible.

Figure 1 shows the voltage fluctuation spectrum. It can be seen that $S_V(f) \sim f^{-\gamma}$, where $\gamma \approx 1$ which differs from the

"white-noise" spectrum (5). For comparison we plotted the intensity of the spectrum calculated from expression (5). In our experiment we have $\omega = 0.3$ mm, $d = 3.5$ mm, $V_z \approx 0.2$ mV, and $B = 1.8$ mT ($\mu_{\text{eff}} \approx 0.5$), which gives $f_c \approx 17$ kHz. It can be seen that in the range of validity of expression (5), the intensity of the spectrum is many times lower than the spectrum (5). Thus, our results indicate that the voltage fluctuations in our high-temperature superconducting ceramic are not caused by independent motion of flux quanta through the sample.

Figure 2 shows typical angular dependences of the current–voltage characteristic $E_z(\alpha)$ and the spectrum $S_V(\alpha)$. It can be seen that

$$E_z(\alpha) = E_0 + E_1 \sin^2(\alpha), \quad E_0 = E_z(0),$$

$$E_1 = E_z(\pi/2) - E_z(0), \tag{6}$$

which follows from Eq. (2) for large currents. However, the electric field satisfies $E_1/E_0 < 0.3$, and it was also found that $j_c(\alpha = 0) \approx j_c(\alpha = \pi/2)$ holds, whereas in the double critical-state model these quantities differ parametrically. We assume that the experimental current–voltage characteristic is closer to the isotropic model (4), which agrees with the results reported by Bean,[4] and the deviations from isotropy arise because the current–voltage characteristic in the equations is local, whereas that measured experimentally is an integrated characteristic. In addition, some of the vortices which penetrated into the granules for an external field $B_0 > 1$ mT give the current–voltage characteristic of vortex line cutting, in accordance with the results presented by Pérez-Rodríguez et al.[1]

The observed angular dependence $S_V(\alpha)$ is also fairly weak.

Thus, it has been shown experimentally that first, the current–voltage characteristic depends weakly on the angle $\alpha$ between the current and the magnetic field; second, the voltage fluctuation spectrum also depends weakly on $\alpha$; and third, the fluctuation spectrum behaves as $1/f$, i.e., the system is strongly fluctuating. All these factors indicate that $\beta \gg 1$
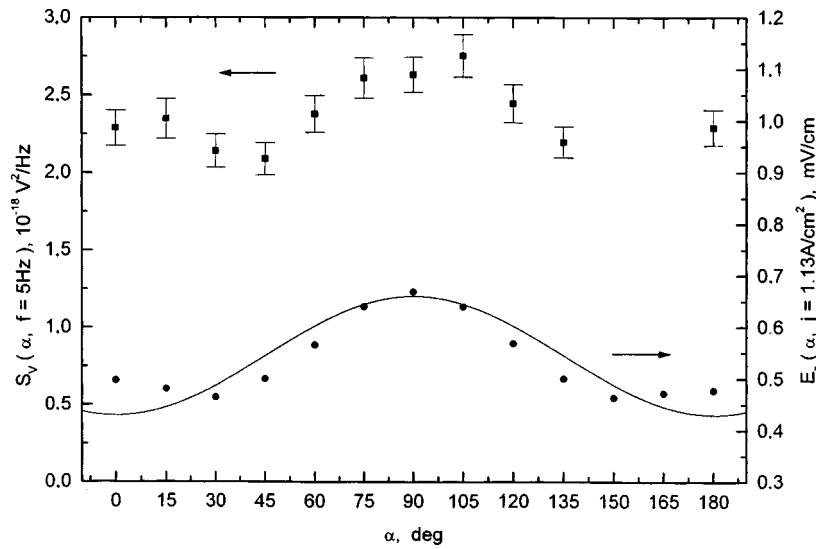
FIG. 2. Angular dependences of the current–voltage characteristic $E_z(\alpha)$ and the spectrum of voltage fluctuations $S_V(\alpha)$ for $|\mathbf{B}_0| = 3.6$ mT and $j = 1.13$ A/cm$^2$. Solid curve — $E_z(\alpha) = 0.23 \sin^2(\alpha) + 0.43$.

holds in our system and suggest that the model of a self-organized critical state in granular superconductors is the most accurate.

The author is grateful to S. L. Ginzburg, A. I. Okorokov, I. D. Luzyanin, V. P. Khavronin, and M. A. Pustovoĭt for useful discussions and assistance with the work.

[1] F. Pérez-Rodríguez, A. Pérez-Gonzalez, J. R. Clem *et al.*, Phys. Rev. B **56**, 3473 (1997).

[2] S. L. Ginzburg, Zh. Éksp. Teor. Fiz. **106**, 607 (1994) [JETP **79**, 334 (1994)].

[3] P. Bak, C. Tang, and K. Wiesenfeld, Phys. Rev. A **38**, 364 (1988).

[4] C. P. Bean, J. Appl. Phys. **41**, 2482 (1970).

[5] S. L. Ginzburg, O. V. Gerashchenko, and A. I. Sibilev, Supercond. Sci. Technol. **10**, 395 (1997).

[6] S. L. Ginzburg, I. D. Luzyanin, and V. P. Khavronin, Supercond. Sci. Technol. **11**, 255 (1998).

[7] R. P. Huebener, Phys. Rep. C **13**, 145 (1974).

Translated by R. M. Durham

# Charge coupling based on resonant surface photoionization

V. V. Antsiferov, B. P. Kashnikov, and G. I. Smirnov

*Institute of Nuclear Physics, Siberian Branch of the Russian Academy of Sciences, Novosibirsk*
(Submitted July 2, 1998)
Pis'ma Zh. Tekh. Fiz. **25**, 14–18 (February 12, 1999)

A method is proposed for charge coupling based on resonant surface photoionization. Possibilities for using resonant surface photoionization to convert optical signals into charge packets and also for the storage and transfer of information are noted. © *1999 American Institute of Physics.* [S1063-7850(99)00302-X]

Here we propose a method of using resonant surface photoionization to convert optical signals into charge packets and also for the storage and directional transfer of the information represented by the charge packets.

Charge-coupled devices are usually controlled by means of a series of synchronized timing voltage pulses.[1,2] These devices mainly operate on the principle of transferring a localized charge by varying the electric potentials at the control electrodes of an array of photosensitive elements.[1,2] In the method of controlling charge coupling described in Ref. 3, the discrete photodetectors in an array have many metal electrodes, which are used to convert optical information into electrical signals proportional to the intensity of the recorded infrared radiation. The base semiconductor crystal used to fabricate the photosensitive array is affected by the fabrication processes, so that attachment of the electrode system gives rise to numerous periodic static irregularities in the array, which lead to inhomogeneities in the photogeneration and thermal generation processes and also in the carrier transfer characteristics. These factors severely limit the efficiency of recording images by charge coupling at low signals and low levels of illuminance.[2] A simpler method of achieving charge coupling using planar technology proposed in Ref. 4 has the same shortcoming because of the presence of periodic static inhomogeneities at the surface of the semiconductor wafer.

These inhomogeneities may be eliminated by a method based on the principle of using dynamic inhomogeneities.[5] In this method of controlling charge coupling, surface acoustic waves generated as a result of the piezoelectric effect are used to create potential wells. The rate of displacement of the potential wells in the semiconductor is the same as the wave propagation velocity. This method of controlling charge coupling by surface acoustic waves is very fast and the product of the delay time and the frequency band is large (up to a few thousand). The main disadvantage of this method is that charge-coupled devices combined with surface acoustic waves can only operate at a fixed frequency band and delays. Recent studies[6,7] have examined photothermal effects caused by the action of pulsed laser radiation on germanium surface states[6] and displacement of the boundary of the $p-n$ junction in direct-gap GaAsP structures.[7]

A possible method of achieving electrodeless control of charge coupling without fixing the frequency band and de-lays may involve using electromagnetic radiation to create a dipole layer at the surface of the semiconductor as a result of the resonant photoionization of particles (atoms or molecules) adsorbed on the surface of the sample.

New technical properties of resonant surface photoionization[8–12] appear in this method of controlling charge coupling in which, instead of electrodes, a monolayer of adsorbed particles must be deposited on the surface of the semiconductor used to fabricate normal charge-coupled devices (Fig. 1). If necessary, this monolayer of adparticles may be separated from the surface of the semiconductor by a thin layer of dielectric whose thickness allows electrons to tunnel from the adsorbed monolayer to the semiconductor. The particles adsorbed on the surface are selected with electronic levels such that the ground state lies within the band gap and the excited state falls within the conduction band of the semiconductor. When radiation in resonance with the transition between these states is incident on the monolayer, the adsorbed particles are excited and electrons tunnel from them into the semiconductor, resulting in the formation of a dipole layer on the irradiated section. When carriers are injected into the charge-coupled device either by photogeneration or electrically, charge packets build up beneath the dipole layer as a result of charge–dipole interaction. Charge transfer can be achieved by moving the irradiated section over the surface (Fig. 1).

Depending on the purpose for which the charge-coupled devices are designed, one or several resonant emitters (light-emitting diodes, microlasers) may be used to illuminate the adparticle monolayer. In this method of controlling charge coupling, the frequency band and delays are not rigidly fixed, since these parameters are determined by the resonant surface irradiation regimes, which can be measured easily and rapidly. The topology of the irradiated region can be almost arbitrary.

If the charge transfer channel is located in the wide-gap semiconductor and the carrier photogeneration region is located in the adsorbed monolayer, we can obtain a high-speed photosensitive charge-coupled device with the desired spectral characteristic, which is determined by the width of the adparticle excited state and the low dark currents in the transfer channel. The semiconductor and the monolayer of resonant particles adsorbed on its surface, forming a particular type of heterostructure, can also give additional advantages
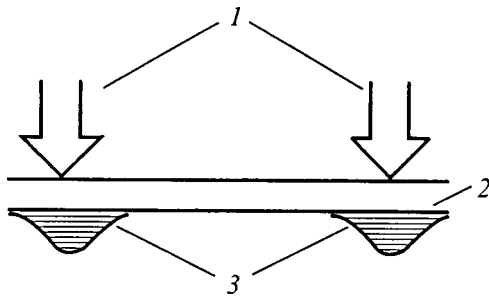
FIG. 1. Charge distribution at various times during transfer based on resonant surface photoionization: *1* — resonant laser irradiation, *2* — adparticle monolayer, *3* — charge packets in semiconductor sample.

from the point of view of optimizing the charge-coupled device (high speed and low noise level).

This method of controlling charge coupling can be implemented by using silicon as the semiconductor and sodium atoms as the adsorbed particles. Figure 2 shows the configuration of the energy levels $E$ of the ground and excited states of sodium atoms relative to the energy bands of silicon. Here $E_g = E_c - E_v$ is the band gap, $E_v$ is the top of the valence band, and $E_c$ is the bottom of the conduction band. The $3S$ ground state of the sodium atom falls within the band gap and its excited state within the conduction band. Sodium atoms are excited to the $3P$ state by $\lambda = 589$ nm resonant laser radiation. Electrons tunnel from excited sodium atoms to the silicon conduction band, resulting in the formation of a dipole layer near the surface and the
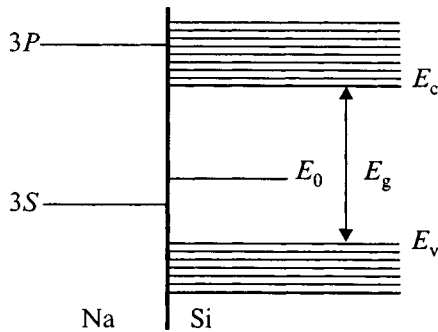
buildup of carriers. Moving the region of resonant irradiation over the monolayer of adsorbed sodium atoms causes charge to be transferred near the surface of the silicon sample along the required trajectory and in the required sequence, both controlled by the resonant emitters.

We note that for simplicity, the energy level diagram does not show any shifts and broadening of the sodium atomic levels or bending of the silicon bands, since these do not alter the fundamental effect. In addition, the perturbations of the adparticle levels are usually large when these are deposited on metal surfaces, whereas when they are deposited on semiconductors, the level perturbations are comparatively small because of the reduced concentration of free electrons.

An infrared radiation detector may be fabricated by injecting impurities into the silicon for which the $E_0$ level is the same as the adparticle ground state. The infrared radiation transfers the electrons from the valence band to the impurity level from which they tunnel to the $3S$ ground state of the adatom which is then released by resonant radiation. A two-stage transition via $3S$–$3P$ takes place to the conduction band. This transition can take place in the semiconductor itself. However, the use of an adsorbed monolayer allows the buildup and transfer of charge (i.e., the charge coupling to be controlled) using resonant radiation.

[1] W. S. Boyle and G. E. Smith, Bell Syst. Tech. J. **49**, 587 (1970).
[2] Yu. R. Nosov and V. A. Shilin, *Principles of the Physics of Charge-Coupled Devices* [in Russian], Nauka, Moscow (1986).
[3] U.S. Patent No. 4064533 (1981).
[4] U.S. Patent No. 4689246 (1987).
[5] S. D. Gaalenua, R. J. Shwartz, and R. L. Gunskor, Appl. Phys. Lett. **29**, 82 (1976).
[6] S. V. Viktsents, S. G. Dmitriev, and G. S. Plotnikov, Fiz. Tekh. Poluprovodn. **31**, 513 (1997) [Semiconductors **31**, 433 (1997)].
[7] G. A. Sukach, Fiz. Tekh. Poluprovodn. **31**(6), 753 (1997) [Semiconductors **31**, 645 (1997)].
[8] B. Auschwitz and K. Lacmann, Chin. Phys. Lasers **113**, 230 (1985).
[9] G. F. Malyshev and G. G. Telegin, Zh. Tekh. Fiz. **56**, 1195 (1986) [Sov. Phys. Tech. Phys. **31**, 700 (1986)].
[10] A. V. Zinov'ev, A. Yu. Lugovskoĭ, and T. Usmanov, Zh. Éksp. Teor. Fiz. **98**, 1364 (1990) [Sov. Phys. JETP **71**, 762 (1990)].
[11] I. Yu. Zakurdaev and D. E. Milovzorov, JETP Lett. **55**, 262 (1992).
[12] V. V. Antsiferov, G. I. Smirnov, and G. G. Telegin, Opt. Commun. **118**, 35 (1995).

Translated by R. M. Durham



FIG. 2. Configuration of ground and excited electronic states of sodium atoms relative to silicon energy bands.

# Modeling of positive streamers in liquid argon

N. Yu. Babaeva and G. V. Naĭdis

*Joint Institute of High Temperatures, Russian Academy of Sciences, Moscow*
(Submitted November 26, 1997; resubmitted June 18, 1998)
Pis'ma Zh. Tekh. Fiz. **25**, 19–27 (February 12, 1999)

A numerical simulation is used to investigate the dynamics of positive streamers in liquid argon. It is shown that as in gases, the nature of the streamer propagation depends on the field strength in the discharge gap. It is established that electron–ion recombination in the streamer channel plays a significant role compared with streamers in gases. © *1999 American Institute of Physics.* [S1063-7850(99)00402-4]

Studies of prebreakdown effects in dielectric liquids are of considerable interest in connection with applications in high-voltage insulation, charged particle detection, and other fields. The range of prebreakdown effects in liquids is extremely extensive and depends on the type of liquid, the pulse length, and the applied field (see, for example, Ref. 1). A distinction is also made between the so-called ''bubble'' and ''electron'' breakdown mechanisms. The first is caused by a phase transition, i.e., the formation of gas–vapor bubbles which form a conducting channel. The second is similar to the breakdown mechanism of gases which is caused by the electron impact ionization of particles. The electron mechanism is typical of liquids with highly mobile charged particles (such as liquefied argon, xenon, and methane) and takes place on a nanosecond time scale. It is natural to assume that the formation of thin plasma channels or streamers observed in liquids in this case is the same as in gases.

Unlike the situation in gases, for which the dynamics of streamers have been described fairly comprehensively, only qualitative models have been proposed for streamers in liquids.[2,3] In this context, it is interesting to use a quantitative approach similar to that used for gases to describe streamers in liquids. Here we present results of calculations of a positive streamer in liquid argon using a two-dimensional (axisymmetric) model.

We analyze the propagation of a streamer from a positive charged metal sphere of diameter $40\,\mu$m inserted in a gap between planar parallel electrodes which generate an additional uniform field $E_0$. This geometry[4] is convenient for studying how the propagation is influenced by a uniform field (which is weak compared with the field near the sphere where the streamer forms). The model of a streamer propagating along the axis of symmetry (passing through the center of the sphere perpendicular to the planes of the parallel electrodes) is similar to that used in Refs. 4 and 5. This model includes the Poisson equation for the electric field potential

$$\mathbf{E}=-\nabla\Phi, \quad \nabla^2\Phi=-4\pi e(n_i-n_e)/\varepsilon, \tag{1}$$

where $n_i$ and $n_e$ are the densities of positive ions and electrons, and $\varepsilon$ is the permittivity of the medium, and the transport equations for the charged particle densities

$$\partial n_e/\partial t+\nabla(n_e\mathbf{V}_e)=\alpha V_e n_e-\beta n_e n_i, \tag{2}$$

$$\partial n_i/\partial t+\nabla(n_i,\mathbf{V}_i)=\alpha V_e n_e-\beta n_e n_i. \tag{3}$$

Here $V_e$ and $V_i$ are the drift velocities of the electrons and ions, and $\alpha$ and $\beta$ are the coefficients of ionization and recombination. It is assumed that the values of $V_{ei}$, $V_i$, $\alpha$, and $\beta$ are determined by the local electric field strength. Unlike the model of a streamer in a gas in which the density of seed electrons ahead of the streamer front was calculated by including a term responsible for volume photoionization in the transport equations, in this case the background value of $n_e$ is assumed to be given (many orders of magnitude lower than the value of $n_e$ in the streamer channel).

Information on the drift velocities and kinetic coefficients in liquids is very incomplete. The electron drift velocity in liquid argon (particle density $n=2.1\times10^{22}\,\mathrm{cm}^{-3}$) has been measured in fields $E<100\,\mathrm{kV/cm}$ (Ref. 6) and values of the recombination coefficient are known in an even narrower range $E<1\,\mathrm{kV/cm}$ (Ref. 7). No direct measurements have been made of the ionization coefficient in liquid argon and only indirect data are available, obtained by analyzing the ignition voltage of a corona discharge[8] and also the results of calculations.[9–11] Here the electron drift velocity was calculated using the expression

$$V_e=\frac{(4\times10^5E^{0.04}+0.4E)\times500E}{4\times10^5E^{0.04}+500E} \quad \mathrm{cm/s} \tag{4}$$

(where $E$ is volts per second), which approximates the experimental data in relatively weak fields and agrees with the calculated results[10] in strong fields (note that in strong fields $V_e$ increases linearly[12] with increasing $E$ and its dependence on $E/n$ is close to that for gaseous argon). Data from Ref. 13 were used for the ion drift velocity:

$$V_i=10^{-3}E \quad \mathrm{cm/s} \tag{5}$$

assuming that the ion mobility does not depend on the field. The ionization coefficient was given by the standard expression

$$\alpha=2.3\times10^5\exp\left(-\frac{3.38\times10^6}{E}\right) \mathrm{cm}^{-1}. \tag{6}$$
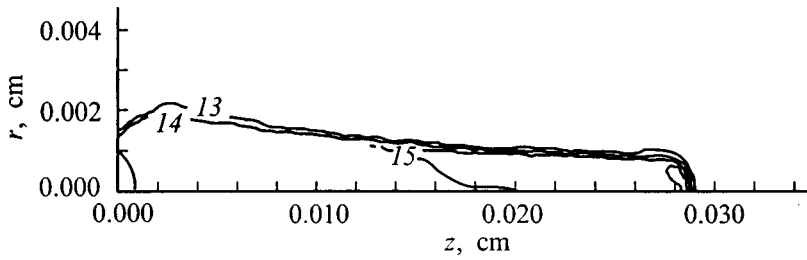
FIG. 1. Electron density contours on the streamer axis. The numbers on the curves denote $\log_{10} n_e$, $cm^{-3}$.

The parameters in this expression were selected to obtain values of $\alpha$ similar to the results given in Refs. 8 and 11. The recombination coefficient $\beta$ was taken to be proportional to the value of $\beta_D$ given by the Debye formula[7]

$$\beta = \xi \beta_D = \xi \frac{4 \pi e V_e}{\varepsilon E}. \tag{7}$$

The value of the numerical coefficient $\xi$ varied (under experimental conditions[7] in weak fields the value of $\xi$ varied between 0.1 and 0.4 as a function of $E$).

Figure 1 give the electron density contours (in the $rz$ plane, where $z$ is the streamer axis) 10 ns after the start of a streamer from a sphere charged to the potential $U = 3$ kV for an applied field $E_0 = 400$ kV/cm (the value of $\xi$ is taken to be 0.1). It can be seen that under these conditions, the streamer becomes thinner (and slower, see below) as it propagates. The characteristic streamer radius is $\sim 10 \, \mu$m. Figure 2 shows the distributions of the electric field and the electron

density on the streamer axis 8 and 10 ns after starting. It can be seen that the electron density reaches a maximum $n_{eh} \sim 10^{17} \, cm^{-3}$ in the streamer head and decays rapidly behind the head to $\sim 10^{15} \, cm^{-3}$ as a result of electron–ion recombination. The maximum field at the streamer head $E_h$ is $\sim 3$ MW/cm. This field satisfies the known condition[14] for saturation of the ionization coefficient $\alpha$ as a function of $E$. Thus, the maximum electron density in the head agrees with the estimate[14]

$$n_{eh} = \frac{\varepsilon}{4 \pi e} \int_0^{E_h} \alpha \, dE, \tag{8}$$

generalized to the case of a medium having a permittivity differing from unity.

The structure of the $E$ and $n_e$ distributions (relative to the maxima) on the streamer axis near the head is shown in greater detail in Fig. 3. The electron density at the field maximum $z = z_h$ is approximately an order of magnitude lower than $n_{eh}$ and the recombination velocity is negligible at this point compared with the ionization rate. In the region beyond the field maximum, where $z < z_h$ holds, the value of $E$ and thus the ionization frequency $\alpha V_e$ decay rapidly. However, the recombination frequency $\beta n_i$ which is proportional to the positive ion density, increases in the region behind the head and becomes equal to the ionization frequency a short distance from the field maximum substantially smaller than the streamer radius. This result can be understood if we bear in
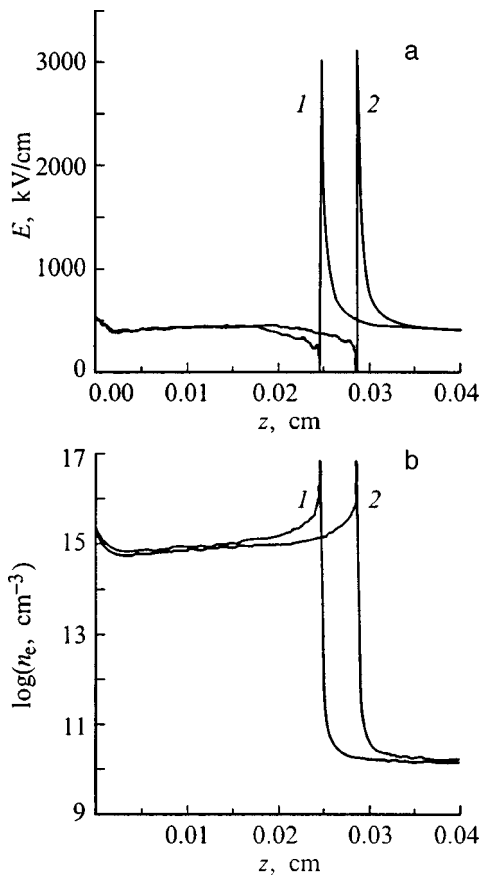


FIG. 2. Distributions of the electric field strength (a) and electron density (b) on the streamer axis at 8 and 10 ns, respectively (curves *1* and *2*).
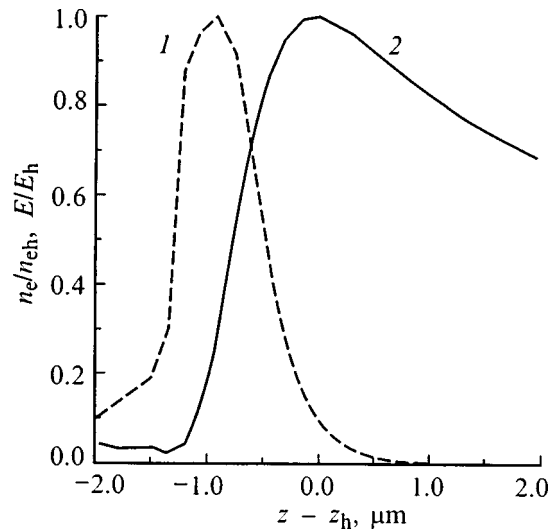


FIG. 3. Distributions of the relative electron density (*1*) and electric field strength (*2*) on the streamer axis near the head.
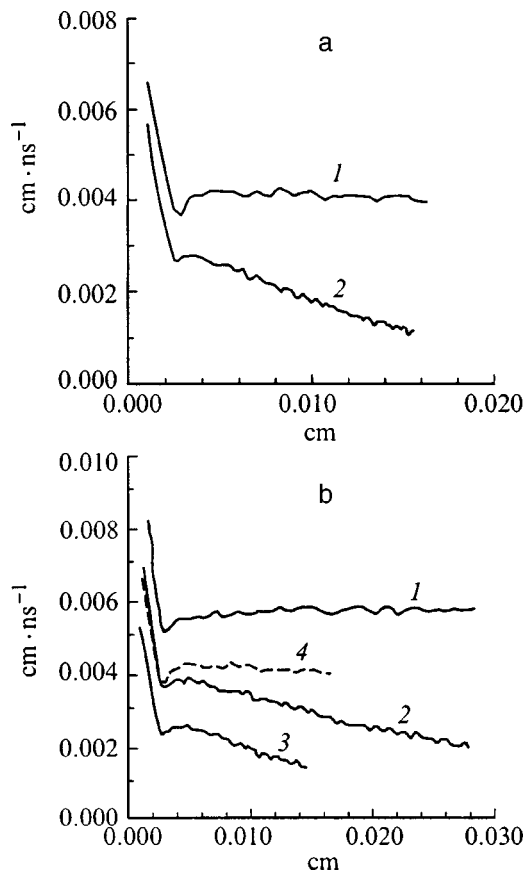
FIG. 4. Streamer velocity versus length: a — $U = 2$ kV, $E_0 = 500$ kV/cm, $\xi = 0.1$ (*1*), and 0.3 (*2*); b — $U = 3$ (*1–3*) and 2 (*4*) kV; $E_0 = 500$ (*1, 4*), 400 (*2*) and 300 (*3*) kV/cm.

mind the approximate relation between the maximum recombination $(\beta n_i)_h$ and ionization $(\alpha V_e)_h$ frequencies derived from expressions (7) and (8):

$$(\beta n_i)_h \approx \xi (\alpha V_e)_h. \qquad (9)$$

From this it can be seen that these values are of the same order of magnitude, i.e., the recombination process is important even in the streamer head.

Note that the conclusion that electron–ion recombination plays an important role in the dynamics of streamers in dense media is not unexpected. It was noted in Ref. 5 that the ionization frequency in the head is proportional to the gas pressure $P$, whereas the charged particle density in the streamer channel and thus the recombination frequency are proportional to $P^2$. Thus, at some fairly high pressure $P$ the recombination process becomes important even in the streamer head.

The nonmonotonic distributions of the plasma parameters in the streamer channel in liquid argon are reminiscent of the corresponding distributions in a strongly electronegative gas.[15,16] Another common factor is that a balance of the electron formation and loss processes in the streamer channel must be maintained for the steady-state propagation (without any reduction in velocity) of even comparatively short streamers.

The influence of recombination on the streamer parameters is shown in Fig. 4a which gives the streamer velocity as

a function of its length calculated for the same external conditions ($U = 2$ kV, $E_0 = 500$ kV/cm) and various values of the coefficient $\xi$. It can be seen that any change in $\xi$ substantially alters the nature of the streamer propagation. Figure 4b gives the velocity ($\xi = 0.1$) for various external conditions. Depending on the field $E_0$ the streamer can either be accelerated or slowed. For the given choice of $\xi$ propagation of the streamer at a constant velocity corresponds to $E_0 = 500$ kV/cm. Under these conditions, the field in the streamer channel, which is approximately equal to $E_0$, ensures that the ionization and recombination frequencies are the same.

Note that as in gases,[4] the nature of the streamer propagation does not depend on its formation conditions (on the potential of the sphere $U$). As $U$ increases only the average velocity and thus the streamer radius increase. Typical values of the streamer velocity are of the same order of magnitude as the measured propagation velocities of the breakdown wave in liquid argon in uniform fields of 300–400 kV/cm (Ref. 17).

To conclude, we stress that these results were obtained without complete information on the values of the kinetic coefficients. As new data appear, these results will be refined. In particular, using dependences of the ionization coefficient $\alpha$ on $E$ which saturate in stronger fields (as calculated in Ref. 10) will increase $E_h$ and $n_{eh}$ and will also increase the field $E_0$ corresponding to steady-state propagation. However, there is reason to predict that these refinements will not substantially alter the distributions of the streamer plasma parameters and will not affect the conclusion that electron–ion recombination plays an important role in the dynamics of streamers in liquids.

[1] H. M. Jones and E. E. Kunhardt, J. Phys. D: Appl. Phys. **28**, 178 (1995).
[2] W. G. Chadband, IEEE Trans. Electr. Insul. **23**, 697 (1988).
[3] V. M. Atrazhev, in *Proceedings of the 11th International Conference on Conduction and Breakdown in Dielectric Liquids*, Baden, Switzerland, 1993, pp. 264–267.
[4] N. Yu. Babaeva and G. V. Naidis, IEEE Trans. Plasma Sci. **25**, 375 (1997).
[5] N. Yu. Babaeva and G. V. Naidis, J. Phys. D: Appl. Phys. **29**, 2423 (1996).
[6] W. G. Schmidt, IEEE Trans. Electr. Insul. **19**, 389 (1984).
[7] K. Shinsaka, M. Codama, T. Srithanratana *et al.*, J. Chem. Phys. **88**, 7529 (1988).
[8] J. L. Hernandes-Avila, N. Bonifaci, and A. Denat, IEEE Trans. Dielectr. Electr. Insul. **1**, 412 (1994).
[9] V. M. Atrazhev, E. G. Dmitriev, and I. T. Iakubov, IEEE Trans. Electr. Insul. **26**, 586 (1991).
[10] E. E. Kunhardt, Phys. Rev. B **44**, 4235 (1991).
[11] N. Bonifaci, A. Denat, and V. M. Atrazhev, IEEE Trans. Dielectr. Electr. Insul. **2**, 137 (1995).
[12] A. A. Belevtsev, in *Proceedings of the 11th International Conference on Conduction and Breakdown in Dielectric Liquids*, Baden, Switzerland, 1993, pp. 135–139.
[13] N. Bonifaci and A. Denat, in *Proceedings of the 12th International Con-*

*ference on Conduction and Breakdown in Dielectric Liquids*, Rome, Italy, 1996, pp. 37–40.

[14] M. I. D'yakonov and V. Yu. Kachorovskiĭ, Zh. Éksp. Teor. Fiz. **94**(5), 321 (1988) [Sov. Phys. JETP **67**, 1049 (1988)].

[15] S. K. Dhali and A. K. Pal, J. Appl. Phys. **63**, 1355 (1988).

[16] M. I. D'yakonov and V. Yu. Kachorovskiĭ, Zh. Éksp. Teor. Fiz. **98**, 895 (1990) [Sov. Phys. JETP **71**, 498 (1990)].

[17] K. Yoshino, IEEE Trans. Electr. Insul. **15**, 186 (1980).

Translated by R. M. Durham

# Acoustic emission in dislocation-containing silicon exposed to current and thermal influences

A. M. Orlov, A. A. Skvortsov, and V. A. Frolov

*Ulyanovsk State University*
(Submitted July 3, 1998)
Pis'ma Zh. Tekh. Fiz. **25**, 28–32 (February 12, 1999)

An investigation was made of acoustic emission in silicon single crystals during passage of an electric current. It was observed that in the temperature range studied ($T=300$–$450$ K) acoustic emission signals whose intensity increases with increasing dislocation density are excited in a static electric field. The acoustic emission of silicon single crystals with and without dislocations is compared. It is assumed that the acoustic emission in silicon is caused by the unpinning and migration of dislocations under the influence of the direct electric current and thermoelastic stresses. The activation energy of this process is estimated as $E=0.53\pm0.05$ eV during passage of a direct current of density $j=2.8\times10^5$ A/m$^2$. © *1999 American Institute of Physics.* [S1063-7850(99)00502-9]

It is known that various external influences on crystals containing linear defects are accompanied by the formation of acoustic pulses (acoustic emission) in their bulk caused by the migration of dislocations, crack formation, and material damage.[1] This situation is typical of semiconductor crystals operated under elevated current and thermal loads,[1] as in semiconductor devices. Despite this, the acoustic emission of semiconductors under constant external influences has clearly not been sufficiently well studied. For example, almost no data are available on the acoustic emission of semiconductors with dislocations in steady-state thermal and electric fields. Thus, the present paper is devoted to the acoustic emission observed in dislocation-containing silicon wafers under current and thermal loads.

The samples were [111]-oriented, phosphorus-doped silicon wafers, with or without dislocations, of length $l=40$ mm, thickness $d=0.35$ mm, and width $h=10$ mm having the resistivity $\rho=0.01$ $\Omega\cdot$cm. The dislocations were introduced by annealing the wafers under load using a three-point system at a temperature of 1000 °C for 10–30 min. The dislocation density was $10^3$ cm$^2$.

Acoustic emission was excited by passing a current of density $j=(1.4$–$5.7)\times10^5$ A/m$^2$ and by external thermal heating. The temperature (300–450 K) was monitored to within $\pm1$ K by using a chromel–alumel thermocouple positioned near the wafer. A liquid In–Ga eutectic was used to reduce the influence of acoustic emission from the current-supply contacts. The ohmic character of the contacts was checked using the current–voltage characteristics.

The acoustic emission signals were recorded by a piezoelectric detector positioned on the surface of the wafer, with VM-6 vacuum oil being used to improve the acoustic contact. The detector was a TsTS-19 piezoceramic wafer of thickness 0.3 mm and diameter 10 mm whose natural frequencies ($f_i\geqslant4$ MHz) were above the spectral composition of the response signal. The electrical response from the detector $U(t)$ was fed to an S9-8 storage oscilloscope connected to a computer to record and store the information. The spectral composition of the response signal $U(\omega)$ was obtained using a standard fast Fourier transform algorithm.

The silicon wafer together with the detector were heated by placing in an electrical furnace. A steady-state temperature was established in the furnace 3.5–4 h after switching on the heating. The spectra obtained during the heating process were used to estimate the vibration energy $W$. In our case, we find $W\sim\Sigma_n U_n^2$, where $U_n$ are the amplitudes of the harmonics of the experimental spectrum. This follows from the directly proportional relationship between $U(t)$ and the vibrational velocity $v(t)$ (Ref. 2). It was established that for $j=0$ the electrical response decreases monotonically after a steady-state temperature has been established and reaches a certain background level after 1.5–2 h. This is at variance with the data given by Kalitenko *et al.*[3] who first observed an acoustic response under thermal perturbation. Our results show that these studies[3] were carried out under nonsteady-state temperature conditions.

Passing a direct current through the wafer radically changes the acoustic response pattern. The spectra obtained under the influence of current show a clearly defined maximum at $f\approx0.25$ Hz. The signal amplitude remains constant even after thermostatic control for 36 h. Thus, most of the investigations were carried out after holding for 2 h at constant temperature.

Typical results plotted in Fig. 1 clearly demonstrate the acoustic emission response of the semiconductor containing dislocations. For instance, when a current $j=2.8\times10^5$ A/m$^2$ is passed through the samples under steady-state temperature conditions, the acoustic emission signal from the samples containing dislocations (curve *1* in Fig. 1) is appreciably higher than the acoustic response of the dislocation-free wafers (curve *3* in Fig. 1). Such striking differences can only be caused by unpinning and migration of anchored dislocations in the static electric field, which agrees with the observations made by Kalitenko *et al.*[3] (thermoelastic stresses may also
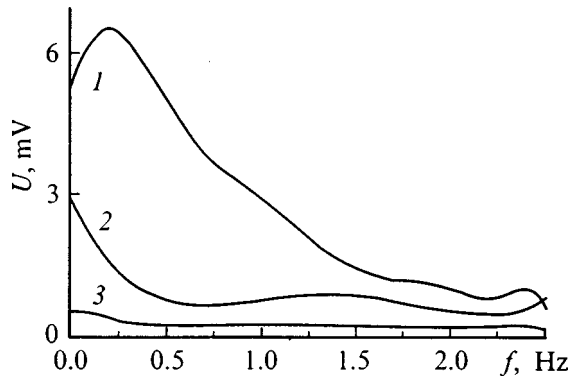
FIG. 1. Spectral power density of acoustic emission signal during passage of a current $j = 2.8 \times 10^5$ A/m² and external heating to 380 K for samples with (*1*) and without (*3*) dislocations; under external heating to 380 K without current (*2*).



FIG. 2. Temperature dependence of the acoustic vibration energy of a silicon wafer with dislocations during passage of a direct current of density $j = 2.8 \times 10^5$ A/m².

have some influence but further studies are needed to estimate their contribution and this is outside the scope of the present paper). A dislocation, having charge and effective mass, should respond to the action of an electric field (entrainment by the field and electron or hole wind) creating a mechanical stress greater than the Peierls stress $\sigma_p$ (Ref. 6). In this case, the dislocation overcomes the potential barrier in the crystal and is shifted from the equilibrium position. At nonzero temperature the potential relief becomes blurred as a result of incoherent thermal motion of the atoms, which reduces $\sigma_p$. The rate of transfer $v$ from one state to another[4,5] may be estimated as

$$v = (1-f)v_1 \exp\left(-\frac{E_d}{kT}\right), \tag{1}$$

where $f$ is the fraction of dislocations which have become unpinned with the activation energy $E_d$, and $v_1$ is the effective transition frequency which determines the maximum in the spectrum of the acoustic emission signals (0.25 Hz) obtained for samples containing dislocations. It follows from Eq. (1) that the temperature has a decisive influence on $v$. This was confirmed by our investigations, which revealed an increase in the amplitude of the recorded signal by a factor of 1.5 when the wafer temperature increased from 380 to 450 K. In order to obtain a more accurate estimate of the temperature changes of the acoustic emission signals, we calculated their energy $W$ and the results are plotted in Fig. 2. The value obtained $E_d = 0.53 \pm 0.05$ eV is typical of the displacement of dislocations in elementary semiconductors. For instance, independent investigations for germanium yielded $E_d \approx 0.55$ eV (Ref. 6).
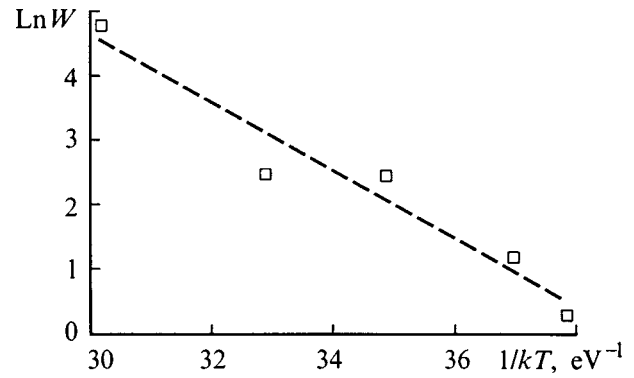
Note also that in the absence of a static electric field the acoustic emission response of the samples with dislocations (curve *2* in Fig. 1) is always higher than that of the dislocation-free wafers (curve *3* in Fig. 1). This result seems unexpected if we bear in mind that the thermal energy $E_{kT} = 0.025 – 0.037$ eV is clearly inadequate for a dislocation to overcome the potential barrier $E_d = 0.53$ eV. We suppose that this apparent contradiction can only be explained by introducing a Boltzmann energy distribution.

To conclude, the acoustic emission observed in silicon wafers containing dislocations is caused by the unpinning and migration of dislocations under the action of steady-state thermal ($T \approx 400$ K) and electric fields ($j = 2.8 \times 10^5$ A/m²). Any temperature deviations from the steady-state value are accompanied by an additional acoustic response, which distorts the true pattern of acoustic emission. The perturbing influence of this factor increases abruptly as the system departs from the equilibrium state.

[1] V. A. Greshnikov and Yu. B. Drobot, *Acoustic Emission* [in Russian], Moscow (1976), 272 pp.
[2] V. I. Domarskas and R.-I. Yu. Kazhis, *Piezoelectric Transducers for Control Measurements* [in Russian], Mintis, Vilnius (1975), 255 pp.
[3] V. A. Kalitenko, I. Ya. Kucherov, and V. M. Perga, Fiz. Tekh. Poluprovodn. **22**, 578 (1988) [Sov. Phys. Semicond. **22**, 361 (1988)].
[4] R. Truell, C. Elbaum, and B. B. Chick, *Ultrasonic Methods in Solid State Physics* (Academic Press, New York, 1969; Mir, Moscow, 1972).
[5] R. M. Peleshchak and B. A. Lukiyanets, Pis'ma Zh. Tekh. Fiz. **24**(2), 37 (1998) [Tech. Phys. Lett. **24**, 57 (1998)].
[6] J. Friedel, *Dislocations* (Pergamon Press, Oxford, 1964; Mir, Moscow, 1967, 643 pp.)

Translated by R. M. Durham

# Modeling of the spectral, power–current, and threshold characteristics of an injection laser

M. G. Noppe

*Novosibirsk State Technical University*
(Submitted September 17, 1997; resubmitted April 13, 1998)
Pis'ma Zh. Tekh. Fiz. **25**, 33–37 (February 12, 1999)

A description is given of a method of modeling the spectral, power–current, and threshold characteristics of an injection laser based on the dependence of the gain on the energy density. The results of the modeling can be used to describe various experimental observations. © *1999 American Institute of Physics.* [S1063-7850(99)00602-3]

1. The dependence of the gain on the energy density[1] $g(P_E)$ has been used to develop a method of calculating the spectral, power–current, and threshold characteristics of a semiconductor injection laser[2,3] which can be used to model various experimental observations. Here we describe the basic features of the method and report some results of the computer modeling of various experiments.

2. The dependence of the gain $g(P_E)$ on the energy density[1] holds when the saturation effect is unimportant. This dependence of $g(P_E)$ makes the equations for the energy density nonlinear. These equations yield[3] the phase condition and the steady-state lasing condition for the nonlinear laser model in the following form:

$$\int_{\sqrt{R_1(\omega_m)}}^{1/\sqrt{R_2(\omega_m)}} \frac{dx}{[g(P_{0m}(x+1/x))-\alpha]x} = L_Z, \tag{1}$$

where $R_1(\omega_m)$ and $R_2(\omega_m)$ are the left-hand and right-hand reflection coefficients, $g[P_{0m}(x+1/x)]$ is the gain at the frequency $\omega_m$ calculated using formula (4) from Ref. 2, $g$ depends on the distribution functions calculated as in Ref. 3 assuming electrical neutrality, and on the densities of states
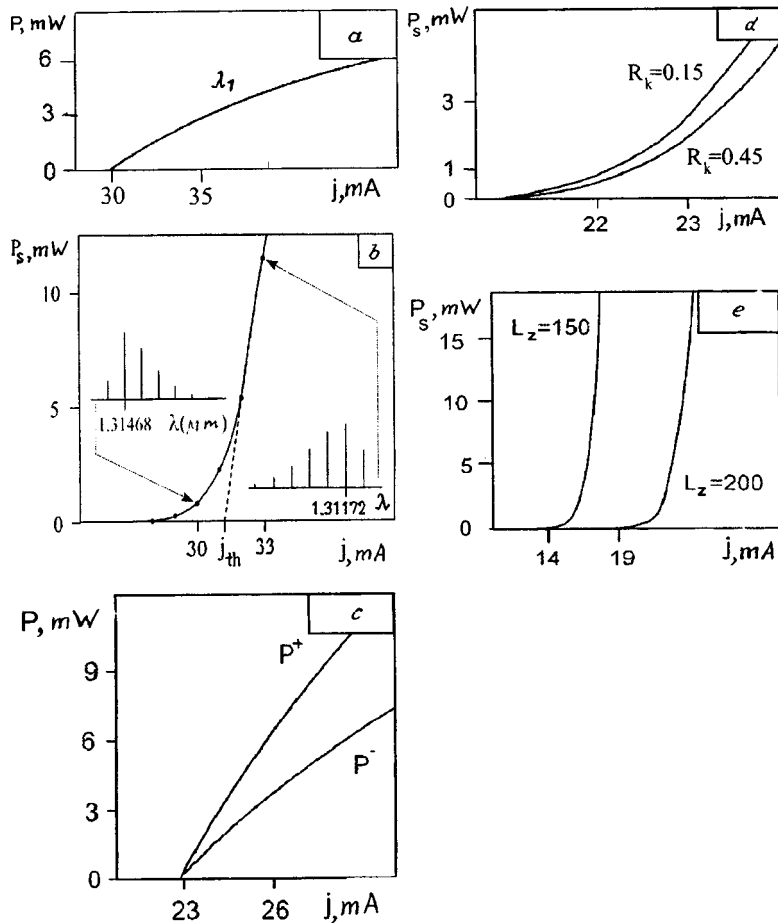


FIG. 1. power–current characteristics, spectra, and mode powers as a function of current.

in the bands,[3] $\alpha$ is the loss factor calculated using formulas (3.8.25) and (3.8.24) from Ref. 4, and $L_z$ is the laser length. The coefficient for the stimulated transition is calculated using a formula obtained from the density matrix equations for a two-level model with relaxation:

$$(H_{21}/\hbar)^2 T_2/2, \qquad (2)$$

where $T_2$ is estimated using the formula $T_2 = 1.27 \times 10^{-11}$ cK/T derived by Alferov *et al.*[5] and the matrix element of the Hamiltonian $H_{21}$ is calculated using formulas (3.6.10), (3.6.13), and (3.6.19) from Ref. 14. Having determined $P_{0m}$ from Eq. (1), we find the coherent radiation power on the right at frequency $\omega_m$ using the formula from Ref. 3:

$$P^+(\omega_m, j) = c P_{0m}(1 - R_2(\omega_m)) L_x L_y / \sqrt{R_2(\omega_m)}. \qquad (3)$$

The right-hand power–current characteristic is given by:

$$P_s^+(j) = \sum_M P^+(\omega_M, j). \qquad (4)$$

3. The experimental studies cited below do not give all the data required for the calculations. Thus, we used a single laser model, i.e., a $p$-$In_{0.71}Ga_{0.29}As_{0.61}P_{0.39}$/InP laser with the parameters and pump formula from Ref. 8. The temperature dependence of the spectral line width (see the experimental data plotted in Figs. 2.11 and 2.12 in Ref. 12 for different types of lasers) was taken into account using an approximation with a correction factor whose accurate value must be determined for each specific laser, since the line width may vary by two orders of magnitude.[12] The aim of the modeling was to compare the behavior of the calculated curves as a function of various parameters with the results of experiments using different types of lasers. a) Figure 1a gives the power calculated using formula (3) for two modes with $\lambda_1 = 1.31369 \mu m$ and $\lambda_2 = 1.31666 \mu m$ at $T = 293$ K plotted as a function of current. Note that the rate of increase in the mode power decreases with increasing current, which agrees with the experiments.[6] Thus, the result of the calculations based on this physical model can explain the behavior of the curves obtained in Ref. 6. b) Figure 1b gives the power–current characteristic plotted using formula (4) and two spectra for currents $j_1 = 30$ mA and $j_2 = 33$ mA at $T = 293$ K, which agrees with the experiments (see Fig. 6 in Ref. 7). c) Having calculated the power–current characteristics at $T = 273$ K and $T = 293$ K we find the threshold current $j_{th}$ for these characteristics using a linear approximation. Describing the temperature dependence of the threshold current using the function $j(T) = j_0 \exp(T/T_0)$, we find the characteristic parameter $T_0$: $T_0 = 69$ which agrees with the observed value $T_0 = 60$ from Ref. 8. d) Figure 1c gives the radiation power for the same frequency across the left and right faces of the laser for $R_1 = 0.3005$ and $R_2 = 0.1505$, which agrees
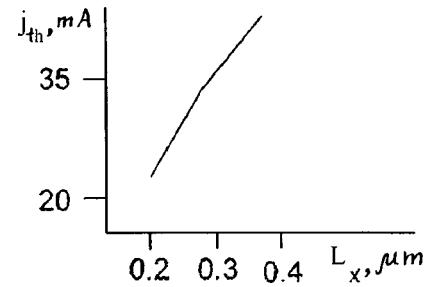


FIG. 2. Threshold current as a function of active zone thickness.

with the experiments reported by Bouadma *et al.*[9] e) Figure 1d gives the power–current characteristics for two lasers: I — for $R_\varkappa = 0.45 (\varkappa = 1.2)$ and II — for $R_k = 0.15$ ($k = 1.2$). These characteristics agree with those obtained experimentally.[10] Figure 1e gives the power–current characteristics for $L_z = 200 \mu m$ and $L_z = 150 \mu m$, which agrees with the experiments described by Levine *et al.*[11] f) The threshold current is plotted as a function of the thickness of the active zone $j_{th}(L_x)$ in Fig. 2 and agrees with the experimental dependence (see Fig. 64 in Ref. 7).

4. Thus, a comparison of the functional behavior of the calculated curves as a function of various parameters with experimental results obtained for different types of lasers has revealed good qualitative agreement, which indicates that the proposed method may be highly relevant.

[1] M. G. Noppe, in *Proceedings of the 11th International Vavilov Conference on Nonlinear Optics*, Novosibirsk, 1997 [in Russian].
[2] M. G. Noppe, in *Proceedings of the 11th International Scientific-Technical Conference APÉP-96*, Novosibirsk, 1996 Vol. 3 [in Russian], pp 91–92.
[3] M. G. Noppe, *Physical Principles of the Nonlinear Theory of Semiconductor Injection Lasers* [in Russian], Novosibirsk (1995), 113 pp.
[4] N. C. Gasey, Jr and M. B. Panise, *Heterostructure Lasers*, Part A (Academic Press, New York, 1978; Vol. 1, Mir, Moscow, 1981, 299 pp.).
[5] Zh. I. Alferov, A. T. Gorelenok, V. V. Mamutin, *et al.*, Fiz. Tekh. Poluprovodn. **18**, 1999 (1984) [Sov. Phys. Semicond. **18**, 1247 (1984)].
[6] N. V. Zotova, S. A. Karandashev, B. A. Matveev, M. A. Remennyĭ, N. M. Stus', and G. N. Talalakin, Pis'ma Zh. Tekh. Fiz. **23**(1), 72 (1997) [Tech. Phys. Lett. **23**, 41 (1997)].
[7] P. G. Eliseev, *Introduction to the Physics of Injection Lasers* [in Russian], Nauka, Moscow (1983), 294 pp.
[8] C. B. Su, R. Olshansky, J. Manning, and W. Powazinik, Appl. Phys. Lett. **44**, 1030 (1984).
[9] N. Bouadma, J. Riou, and A. Kampfer, Electron. Lett. **231**, 566 (1985).
[10] N. K. Dutta and P. P. Deimel, IEEE J. Quantum Electron. **QE-19**, 496 (1983).
[11] B. F. Levine, J. P. Van Der Ziel, and C. G. Bethea, Electron. Lett. **18**, 690 (1982).
[12] *Physics of Semiconductor Lasers*, edited by Kh. Takuma [Russ. transl.], Mir, Moscow (1989), 310 pp.

Translated by R. M. Durham

# Influence of a thin conducting transverse layer on the properties of quasitransverse shear waves and Lamb waves in gallium arsenide plates

I. E. Kuznetsova, B. D. Zaĭtsev, I. A. Borodina, and V. V. Popov

*Saratov Branch of the Institute of Radio Engineering and Electronics, Russian Academy of Sciences*
(Submitted July 6, 1998)
Pis'ma Zh. Tekh. Fiz. **25**, 38–43 (February 12, 1999)

An investigation was made of the influence of a thin conducting surface layer on the damping and velocity of acoustic waves in gallium arsenide plates. It was observed that the square of the coefficient of electromechanical coupling for specific directions of propagation of Lamb waves and quasitransverse shear waves is an order of magnitude higher than that for surface acoustic waves. Thus, the conductivities of the substrate and the surface layer have a stronger influence on the damping of waves in the plates than in the case of surface acoustic waves. © *1999 American Institute of Physics.* [S1063-7850(99)00702-8]

As is well known,[1] two types of elastic waves, Lamb waves and transverse waves, can propagate in an unbounded plate with free surfaces. Pure transverse waves only exist in isotropic materials or in crystals possessing specific crystalline symmetry. Recently published studies[2,3] have shown that so-called quasitransverse shear (QSH) waves can exist in plates. One of the main characteristics of these waves is that there is almost no dispersion or any component of the particle mechanical displacement normal to the surface for $h/\lambda < 1$, where $h$ is the plate thickness and $\lambda$ is the acoustic wavelength. Unlike pure transverse waves, QSH waves can propagate in crystals of any symmetry. Theoretical and experimental studies have shown that the coefficient of electromechanical coupling for QSH and Lamb waves in piezoelectric plates depends strongly on the plate thickness and may be an order of magnitude higher than the similar parameter for surface acoustic waves.[4,5]

Zaĭtsev *et al.*[6] and Chaplik[7] showed that thin conducting surface layers influence the velocity and damping of surface acoustic waves propagating in noncentrosymmetric piezosemiconducting crystals. This effect is caused by acoustoelectric interaction between conduction electrons and the electric field accompanying the acoustic wave. Moreover, the amplitude of the induced oscillations of the carrier concentration depends on the electromechanical coupling coefficient. In this context, it is interesting to study the influence of thin conducting surface layers on Lamb and QSH waves in piezosemiconducting plates.

The influence of the bulk conductivity and the electron drift velocity on the velocity and damping of normal waves and Lamb waves has been studied theoretically and experimentally[8–10] for cadmium sulfide. One of the most widely used materials nowadays is gallium arsenide. However, the influence of surface and bulk electrons on the characteristics of Lamb and QSH waves in GaAs plates has not yet been studied.

This problem was solved using standard equations of motion for an elastic medium, the Poisson equation, the equation of continuity, and rate equations for the mechanical stress, electric induction, and conduction current with allowance for the piezoelectric effect and carrier diffusion in the plate.[6] The boundary conditions were zero mechanical stresses and normal component of the conduction current and continuity of the potential at the boundaries of the plate. The influence of the thin conducting layer was taken into account by a jump in the normal component of the electric induction caused by the surface charge.[11]

We calculated the coefficients of electromechanical coupling of the symmetric ($S_0$) and antisymmetric ($A_0$) Lamb and QSH waves for different directions of propagation in the most commonly used crystallographic planes of gallium arsenide (001), (110), (111), and (112).

It was observed that the maximum coefficient of electromechanical coupling $K$ of the plate waves was almost an order of magnitude higher than the same parameter for the surface acoustic waves. For example, for the most piezoactive [110] direction in the (001) plane for surface acoustic waves we have $K = 0.04\%$, whereas for $S_0$ and QSH waves in the (110) plane there are directions where this value is 0.2% and 0.3%, respectively for $h/\lambda = 0.1$, and for the $A_0$ wave in the (001) plane and the [110] direction this coefficient is $K = 0.13\%$ for $h/\lambda = 0.4$ (Fig. 1a). The coefficient $K$ is higher for the plate waves because the ratio of the electric field energy outside the crystal to that inside the crystal is substantially greater for a plate than for a semiinfinite medium. Thus, the metallization of the plate will have a greater influence on the velocity of the plate waves compared with surface acoustic waves.

Figure 1b gives the power damping of 100 MHz waves in the plate as a function of the bulk conductivity for different types of waves. These results show qualitative agreement with known experimental data for CdS.[9,10]

Figures 2a–2c give the damping of Lamb and QSH waves as a function of the conductivity of a thin layer on the surface of the plate for various values of the bulk conductivity. As in the case of surface acoustic waves,[6] an absorption peak is observed for $\sigma_s = 10^{-7}$ S, perhaps because for low $\sigma_s$
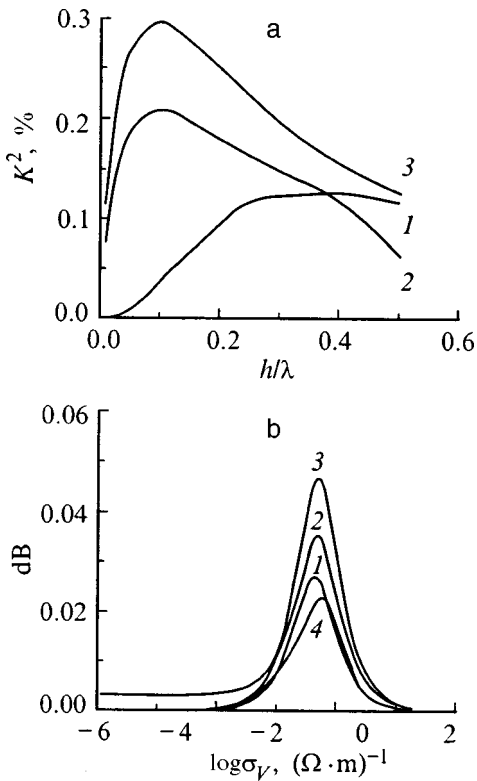
FIG. 1. a — Coefficient of electromechanical coupling $K$ versus relative plate thickness, b — wave damping in plate versus bulk conductivity $\sigma_v$ : *1* — $A_0$ wave in (001) plane in [110] direction ($h/\lambda = 0.4$); *2* — $S_0$ wave in (110) plane at an angle of 40° to the [001] direction ($h/\lambda = 0.1$); *3* — QSH wave propagating in (110) plane in the [001] direction ($h/\lambda = 0.1$); *4* — surface acoustic wave propagating in the (001) plane in the [110] direction.
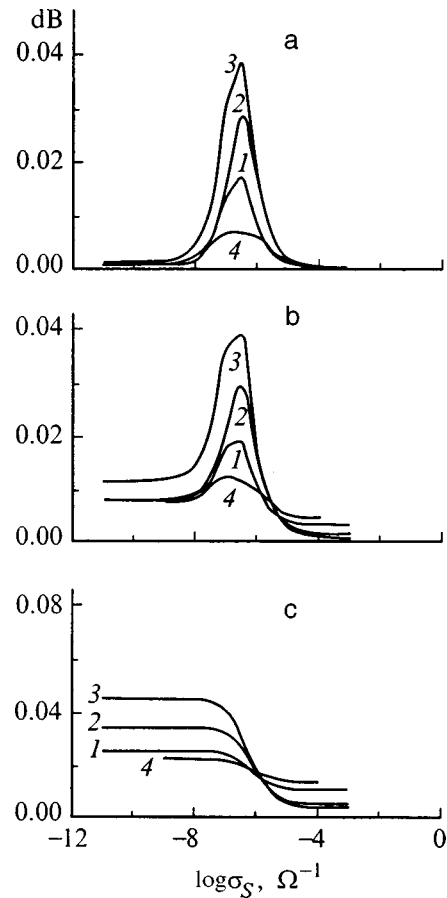


FIG. 2. Wave damping in plate as a function of the surface conductivity ($\sigma_s$): a — $\sigma_v = 0.001$; b — $\sigma_v = 0.01$; c — $\sigma_v = 0.1$. *1* — $A_0$ wave in (001) plane in [110] direction ($h/\lambda = 0.4$); *2* — $S_0$ wave in (110) plane at an angle of 40° to [001] direction ($h/\lambda = 0.1$); *3* — QSH wave propagating in the (110) plane in the [001] direction ($h/\lambda = 0.1$); *4* — surface acoustic wave propagating in the (001) plane in the [110] direction.

the layer has no influence on the acoustic wave and introduces no damping, whereas for large $\sigma_s$ the layer becomes an ideal conductor. It can be seen from Fig. 2 that as the bulk conductivity increases, the curves become straighter and for $\sigma_v > 0.1$ the influence of the surface conductivity can be neglected.

These graphs indicate that the bulk and surface conductivity have a greater influence on the characteristics of QSH and Lamb waves than on those of surface acoustic waves.

Calculations were also made of the relative change in the phase velocity of a wave in the plate as a function of the surface conductivity for different types of waves and the bulk conductivity. It was observed that as the surface conductivity increases, the velocity of the acoustic waves in the plate decreases and the maximum change in velocity, which is equal to the electromechanical coupling coefficient, depends on the plate thickness.

These results indicate that the parameters of electroacoustic signal processing devices based on GaAs can be improved substantially by using waves in the plates instead of surface acoustic waves.

[1] *Physical Acoustics: Principles and Methods*, edited by W. P. Mason (Academic Press, Orlando, 1964; Mir, Moscow, 1966), Vol. 1, Part A.

[2] S. G. Joshi and Y. Jin, Ultrasonics **34**, 507 (1996).

[3] Y. Jin and S. G. Joshi, IEEE Trans. Ultrason. Ferroelectr. Freq. Control **43**, 491 (1996).

[4] B. D. Zaitsev, S. G. Joshi, and I. E. Kuznetsova, Smart Structures **6**, 739 (1997).

[5] S. G. Joshi and Y. Jin, J. Appl. Phys. **70**, 4113 (1991).

[6] B. D. Zaĭtsev, I. E. Kuznetsova, and I. S. Nefedov, Pis'ma Zh. Tekh. Fiz. **20**(4), 60 (1994) [Tech. Phys. Lett. **20**, 159 (1994)].

[7] A. V. Chaplik, Pis'ma Zh. Tekh. Fiz. **10**(11), 1385 (1984) [Sov. Tech. Phys. Lett. **10**, 584 (1984)].

[8] Do Khak Khyong, N. Ya. Kotsarenko, and A. M. Fedorchenko, Ukr. Fiz. Zh. **15**, 1878 (1970).

[9] I. Ya. Kucherov and I. V. Ostrovskiĭ, Ukr. Fiz. Zh. **16**, 209 (1971).

[10] P. V. Burliĭ, I. Ya. Kucherov, M. Yu. Omel'yanenko, and I. V. Ostrovskiĭ, Ukr. Fiz. Zh. **20**, 327 (1975).

[11] I. A. Viktorov, Dokl. Akad. Nauk SSSR **187**, 294 (1969) [Sov. Phys. Dokl. **14**, 660 (1969)].

Translated by R. M. Durham